

Journal of Combustion

Coal and Biomass Combustion

Lead Guest Editor: Hanhui Jin

Guest Editors: Kun Luo, Oliver T. Stein, Hiroaki Watanabe, and Xiaoke Ku





Coal and Biomass Combustion

Journal of Combustion

Coal and Biomass Combustion

Lead Guest Editor: Hanhui Jin

Guest Editors: Kun Luo, Oliver T. Stein, Hiroaki Watanabe,
and Xiaoke Ku



Copyright © 2018 Hindawi. All rights reserved.

This is a special issue published in “Journal of Combustion.” All articles are open access articles distributed under the Creative Commons Attribution License, which permits unrestricted use, distribution, and reproduction in any medium, provided the original work is properly cited.

Editorial Board



Kalyan Annamalai, USA
S. R. Chakravarthy, India
Bruce Chehroudi, USA
Michael A. Delichatsios, UK
Michael Fairweather, UK
Sergey M. Frolov, Russia

Peyman Givi, USA
Ashwani K. Gupta, USA
Kazunori Kuwana, Japan
Cheng-Xian Lin, USA
Thanos Megaritis, UK
Ishwar K. Puri, Canada




Li Qiao, USA
Constantine D. Rakopoulos, Greece
Dimitrios C. Rakopoulos, Greece
Richard Saurel, France
Benjamin Shaw, USA

Contents



Coal and Biomass Combustion

Hanhui Jin , Kun Luo, Oliver Stein, Hiroaki Watanabe , and Xiaoke Ku 
Editorial (2 pages), Article ID 9654923, Volume 2018 (2018)

A Large Eddy Simulation Study on the Effect of Devolatilization Modelling and Char Combustion Mode Modelling on the Structure of a Large-Scale, Biomass and Coal Co-Fired Flame

Miriam Rabaçal, Mário Costa , Michele Vascellari, Christian Hasse , Martin Rieth, and Andreas M. Kempf 
Research Article (15 pages), Article ID 7036425, Volume 2018 (2018)

3D Instantaneous Reconstruction of Turbulent Industrial Flames Using Computed Tomography of Chemiluminescence (CTC)

A. Unterberger , M. Röder, A. Giese, A. Al-Halbouni, A. Kempf , and K. Mohri
Research Article (6 pages), Article ID 5373829, Volume 2018 (2018)

Simulation of Coal and Biomass Cofiring with Different Particle Density and Diameter in Bubbling Fluidized Bed under O₂/CO₂ Atmospheres

Chao Chen , Xuan Wu, and Lingling Zhao 
Research Article (12 pages), Article ID 6931483, Volume 2018 (2018)


Experimental Investigation of Combustion Kinetics of Wood Powder and Pellet

Peng Haobin, Yuesheng Li, Yunquan Li , Fangyang Yuan, and Guohua Chen 
Research Article (7 pages), Article ID 5981598, Volume 2018 (2018)

Thermodynamic Analysis of Supercritical CO₂ Power Cycle with Fluidized Bed Coal Combustion

Chenchen Geng, Yingjuan Shao , Wenqi Zhong, and Xuejiao Liu
Research Article (9 pages), Article ID 6963292, Volume 2018 (2018)

Investigation of the Thermal Improvement and the Kinetic Analysis of the Enriched Coal

Selma Duzyol  and Cem Sensogut
Research Article (10 pages), Article ID 1761023, Volume 2018 (2018)

Editorial

Coal and Biomass Combustion

Hanhui Jin ¹, **Kun Luo**,² **Oliver Stein**,³ **Hiroaki Watanabe** ⁴, and **Xiaoke Ku** ¹

¹*School of Aeronautics and Astronautics, Zhejiang University, Hangzhou 310027, China*

²*State Key Laboratory of Clean Energy Utilization, Zhejiang University, Hangzhou 310027, China*

³*Institut für Technische Verbrennung, Universität Stuttgart, Herdweg 51, 70174 Stuttgart, Germany*

⁴*Department of Mechanical Engineering, Kyushu University, Fukuoka, Fukuoka 8190395, Japan*

Correspondence should be addressed to Hanhui Jin; enejhh@zju.edu.cn

Received 8 October 2018; Accepted 8 October 2018; Published 29 November 2018

Copyright © 2018 Hanhui Jin et al. This is an open access article distributed under the Creative Commons Attribution License, which permits unrestricted use, distribution, and reproduction in any medium, provided the original work is properly cited.

Coal combustion is the largest source of global energy consumption and electricity generation worldwide now and will remain so in the foreseeable future, although coal is also one of the major sources of air pollution. Increasing the efficiency of coal-fired power plants across the world will greatly reduce air pollution and extend the lifetime of our coal resources. The combustion of solid biomass fuels as a renewable energy source has grown significantly in the last decade, principally because it can be used to replace fossil fuels (coal, oil, and natural gas).

For this special issue of the Journal of Combustion, we have invited researchers to focus on the combustion of solid fuels and their related processes in power generation. The submitted papers cover a diversity of aspects reflecting the latest progress in the field. These include integrating the supercritical CO₂ Brayton cycle with the coal-fired circulating fluidized-bed boiler, coal and biomass cofiring systems, combustion kinetics of biomass materials, thermal improvement and combustion kinetics of enriched coal, and Computed Tomography of Chemiluminescence (CTC) for turbulent industrial flame reconstruction.

Biomass appears to be a promising source of power generation and about half of the papers focus on the biomass related fields, including the combustion kinetic characteristics of wood powder and pellets, as well as the combustion process. Although some methods to utilize pure biomass have been developed (e.g., pyrolysis, gasification, and combustion), the coal and biomass cofiring system is still the most important technology for biomass energy conversion. In this special

issue, both of the final published papers on biomass utilization pay attention to the coal and biomass cofiring process, implying that coal combustion is still difficult to be entirely replaced in energy generation.

Regarding the methods used in the published research, both experimental and numerical methods show their advantages in different fields. In this special issue, the combustion kinetics of different materials were studied experimentally and numerical research was carried out to study the combustion processes. Computed Tomography of Chemiluminescence (CTC) for turbulent industrial flame reconstruction was also included in the current issue, which may become a useful tool for researchers and scientists for studying flame structure and evolution.

Conflicts of Interest

The members of the guest editorial team do not have any possible conflicts of interest or private agreements with companies, including the following. (1) Any of us will refuse to handle the manuscript, if he has recently coauthored with the author of the manuscript, which could be perceived to be influenced by the relationship or recently shared an affiliation or employment history with the author. (2) We will identify any undeclared conflicts that an author might have according to our knowledge of the discipline, when making a recommendation on the manuscript. (3) We will consider potential conflicts when assigning the manuscript to reviewers according to our knowledge. We will not select a referee who (i) works or has recently worked at the same institution

as the author or authors, (ii) has recently coauthored a paper with the author or authors, or (iii) has a recent or current collaboration with the author. (4) If we have concerns about a potential reviewer, we will consider appointing someone else. If we believe a reviewer's recommendation on a manuscript was made to further their own interests, we may tell the authors they do not need to address that point.

Hanhui Jin
Kun Luo
Oliver Stein
Hiroaki Watanabe
Xiaoke Ku

Research Article

A Large Eddy Simulation Study on the Effect of Devolatilization Modelling and Char Combustion Mode Modelling on the Structure of a Large-Scale, Biomass and Coal Co-Fired Flame

Miriam Rabaçal,¹ Mário Costa ,¹ Michele Vascellari,² Christian Hasse ,³ Martin Rieth,⁴ and Andreas M. Kempf ⁴

¹IDMEC, Mechanical Engineering Department, Instituto Superior Técnico, Universidade de Lisboa, Av. Rovisco Pais, Lisboa, Portugal

²Technische Universität Bergakademie Freiberg, Freiberg, Germany

³Technische Universität Darmstadt, Darmstadt, Germany

⁴Institute for Combustion and Gasdynamics (IVG), Chair of Fluid Dynamics, University of Duisburg-Essen, Duisburg, Germany

Correspondence should be addressed to Andreas M. Kempf; andreas.kempf@uni-due.de

Received 5 July 2018; Revised 4 September 2018; Accepted 17 September 2018; Published 1 November 2018

Guest Editor: Kun Luo

Copyright © 2018 Miriam Rabaçal et al. This is an open access article distributed under the Creative Commons Attribution License, which permits unrestricted use, distribution, and reproduction in any medium, provided the original work is properly cited.

This work focuses on the impact of the devolatilization and char combustion mode modelling on the structure of a large-scale, biomass and coal co-fired flame using large eddy simulations. The coal modelling framework previously developed for the simulation of combustion in large-scale facilities is extended for biomass capabilities. An iterative procedure is used to obtain devolatilization kinetics of coal and biomass for the test-case specific fuels and heating conditions. This is achieved by calibrating the model constants of two empirical models: the single first-order model and the distributed activation energy model. The reference data for calibration are devolatilization yields obtained with predictive coal and biomass multistep kinetic mechanisms. The variation of both particle density and diameter during char combustion is governed by the conversion mode, which is modelled using two approaches: the power law using a constant parameter that assumes a constant mode during char combustion and a constant-free model that considers a variable mode during combustion. Three numerical cases are considered: single first-order reaction with constant char combustion mode, distributed activation energy with constant char combustion mode, and single first-order reaction with variable char combustion mode. The numerical predictions from the large eddy simulations are compared with experimental results of a high co-firing rate large-scale laboratory flame of coal and biomass. Furthermore, results from single particle conversion under idealised conditions, isolating the effects of turbulence, are presented to assist the interpretation of the predictions obtained with large eddy simulations. The effects of the devolatilization and conversion mode modelling on the flame lift-off, flame length, and spatial distribution and radial profiles of O_2 and CO_2 are presented and discussed. Both the devolatilization and conversion mode modelling have a significant effect on the conversion of particles under idealised conditions. The large eddy simulations results show that the devolatilization model has a strong impact on the flame structure, but not on the flame lift-off. On the other hand, for the tested numerical conditions, the char combustion mode model has a marginal impact on the predicted results.

1. Introduction

Co-firing biomass with coal can have a major role in accomplishing the European Union's renewable targets for power production while contributing to energy security and grid stability [1]. Although biomass co-firing has been successfully demonstrated in over 150 installations worldwide, there are still many open questions concerning flame

stability, combustion efficiency, and pollutant emissions [2].

There are only a few examples in the literature of detailed experimental studies of large-scale laboratory co-firing under operating conditions that are relevant for power production. Relevant studies include those of Annamalai and coworkers. [3, 4], Damstedt et al. [5, 6], Lu et. al [7], and Casaca and Costa [8]. These studies have shown the positive impact of adding

biomass on pollutant emissions, particularly the emissions of NO_x . Among these, the work reported by Damstedt and coworkers [5, 6] provides the most complete set of in-flame experimental data for comparison with numerical predictions at a high co-firing ratio ($\approx 50\%$). Numerical studies of pulverised biomass combustion or co-firing of coal and biomass under realistic conditions are scarce, which is not surprising given the shortage in detailed experimental measurements. Yin et al. [9] compared RANS predictions with the experimental data [5, 6] and obtained a reasonable agreement. They found that modelling intraparticle temperature gradients in large biomass particles had little influence on the predictions. Furthermore, a four-step gas reaction mechanism, combined with eddy dissipation rate, outperformed a two-step mechanism, combined with eddy break-up. Other numerical studies are those of Ghenai and Janajreh [10], Ma et al. [11], Black et al. [12], and Blackreedy et al. [13], focused on purely numerical results of RANS simulations of industrial scale biomass combustion and co-firing biomass with coal. The work of Blackreedy et al. [13] focuses on how the devolatilization and the char combustion rate affect the particle burnout; however no comparisons with experimental data are provided. The authors emphasise the importance of the uncertainties in the absolute values of devolatilisation model constants under the heating conditions of the study, given that, for biomass combustion, devolatilisation is the process responsible for the major release of mass to gas phase. Note that the low co-firing ratio in this study is 3%, so that the characteristics of the flame were essentially the same as those of a base coal flame.

The process of devolatilization has a significant impact on flame stabilisation and on flame length and consequently on particle burnout and combustion efficiency. A number of advanced coal and biomass conversion models have emerged in the past decade, such as the Chemical Percolation Devolatilization (CPD) model [14] and Bio-PoliMi [15]. The CPD model includes network modelling, coal structure characterization, depolymerization reactions, cross-linking reactions, and noncondensable gas, tar, and char formation. The Bio-PoliMi model has a “mechanist” approach based on conventional multistep devolatilization models of the three reference components of biomass (cellulose, lignin, and hemicellulose) and predicts the yields and lumped composition of the devolatilization products. The complexity of these models makes their use prohibitive in LES; therefore strategies are needed to bridge the advanced conversion models and the cost-effective empirical models that are suitable for CFD codes. Hashimoto et al. [16] used a tabulation strategy based on the particle temperature history to store the results of the devolatilization models for retrieval during the simulation. Vascellari et al. [17] used a number of heating rates from the CFD simulation to calibrate a simple kinetic expression for the volatile yield for later direct use. The latter method has been successfully used in the past for LES of large-scale of coal combustion [18] and Rieth et al. [19] showed that it yields similar averaged predictions as those obtained when directly coupling the CPD model to LES of a small-scale coal flame. The calibration methods have been applied to a single first-order devolatilization model

(SFOR) but other empirical models are also good candidates, such as the distributed activation energy model (DAEM) that assumes multiple decomposition steps at a reduced computational cost [20, 21].

In contrast to biomass char combustion, coal char combustion has been a subject of research for many years. Still, it can be assumed that the mechanisms of char combustion for coal are also applicable for chars originating from lignocellulosic fuels [22]. Heterogeneous char conversion depends on the char surface area, the surface accessibility, the carbon active sites and catalytic active sites created by indigenous or added inorganic matter, the particle temperature, and the local gaseous reactant concentration. These parameters influence the char combustion mode that in large-scale facilities typically is controlled by both kinetics and diffusion (regime II) or only by diffusion (regime III), depending on the operating conditions. Mitchell et al. [23] showed that the power law mode, based on a tunable model constant, is prone to failure in predicting the variations in size and apparent densities of char particles undergoing oxidation in a moderate zone II burning regime. More recently, Haugen and Mitchel [24] showed that the particle radius decreases with the ratio of the time derivative and the spatial derivative of the particle density at the surface of the particle. A model was proposed that can be used to describe the mode of conversion of reactive porous particles in a range of different applications such as entrained flow gasifiers, pulverized coal burners, and circulating fluidized bed combustors, without any tunable parameters.

The main objective of this work is to evaluate the impact of the devolatilization model and the char combustion mode model on the structure of a large-scale, biomass and coal co-fired flame. The devolatilization calibration procedure applied previously to PCC [18, 25] is extended to biomass, using SFOR and DAEM to model devolatilization, and the char combustion mode is modelled using two different approaches to describe the variation of density and diameter of the char particle. First, single particle conversion is analysed in order to assess the impact of the tested models on devolatilization and char combustion under idealised conditions and in the absence of turbulence. Subsequently, three LES test cases were simulated in order to assess the effect of devolatilization and conversion mode modelling on the particle conversion in the furnace, the flame structure, and the gas phase major species radial profile. The numerical predictions are compared to the experimental measurements of major gas species of the high co-firing ratio study performed by Damstedt et al. [5, 6] and the effects of the conversion models on the flame structure are discussed.

2. Experimental Conditions

Damstedt and coauthors measured the distribution of several gaseous species mole fractions for a set of coal and biomass flames [5, 6]. In this study, the *co-firing 1.0* case is targeted. Figure 1 shows the burner and quartz geometry of the Brigham Young University (BYU) furnace and Table 1 lists the operating conditions. Table 2 lists the coal (high volatile bituminous Blind Canyon) and biomass (straw) properties, while Figure 2

TABLE 1: Operating conditions of the targeted test case [5].

Mass flow rate	kg/h
Center fuel - straw	15.1
Annular fuel - coal	7.5
Central air	9.0
Annular air	12.0
Secondary air	160.0
Swirl Number [-]	1.0

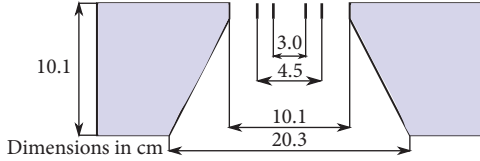


FIGURE 1: Burner and quarl geometry of the BYU furnace. Coal is fed through the central inlet, biomass through the annular middle inlet, and secondary swirled air through the outer annular inlet. [5].

shows the particle size distribution. Note that the particle size distribution of biomass is much wider than that of coal.

Water-cooled probes were used to sample combustion products along the radius on several axial locations along the furnace. The gas samples were fed to an online Horiba gas analyser to measure major species mole fractions. The measurements of CO_2 showed exceptional repeatability of 4.6%, whereas O_2 showed a lower repeatability of 20.3%. The uncertainties of the experimental studies, concerning boundary conditions, measurement repeatability, and the experimental flame asymmetry, do not allow for an extensive validation. In this work, the global features of the experimentally studied flame provide valuable comparison data to access the effect of conversion models on the flame shape, namely, flame lift-off, flame break, and flame length.

3. Coal and Biomass Combustion Modelling

This work presents an extension of the modelling framework as used in the previous work of Rabaçal et al. [18], where an LES of large-scale laboratory coal flame was presented, by adding the DAEM devolatilization model and the Haugen and Mitchel [24] char conversion mode model. For brevity, the modelling details concerning particle motion, particle heat balance, volatile combustion, and gas-phase radiation are summarised here, whereas the DAEM and the Haugen and Mitchel [24] models are described in more detail.

3.1. Particle Motion. The particles' trajectory is described in a Lagrangian framework. The particles are point sources assumed to be nondeformable and, given that the disperse phase is assumed to be dilute, particle-to-particle interactions are neglected. The only considered forces acting on the particle's acceleration \mathbf{u}_p are drag \mathbf{F}_D and gravity \mathbf{F}_G given by $d\mathbf{u}_p/dt = \mathbf{F}_D + \mathbf{F}_G$. The gravity force is calculated as $\mathbf{F}_G = m_p(1 - \rho_g/\rho_p)\mathbf{g}$, where m_p is the particle mass, ρ_p is the

particle density, ρ_g is the gas density, and \mathbf{g} is the gravitational acceleration. The drag force is calculated as

$$\mathbf{F}_D = \frac{3}{4} \frac{\rho_g m_p}{\rho_p d_p} C_D (\mathbf{u}_g - \mathbf{u}_p) |\mathbf{u}_g - \mathbf{u}_p| \quad (1)$$

where d_p is the particle diameter, \mathbf{u}_g is the velocity of the gas, and \mathbf{u}_p is the velocity of the particle. The drag coefficient C_D has been shown empirically to correlate with the particle Reynolds number $Re_p = \rho_g |\mathbf{u}_g - \mathbf{u}_p| d_p / \mu$, where μ is the viscosity of the gas. Given that the particle shape was not reported quantitatively in the experimental study, both coal and biomass particles are assumed spherical. For a spherical particle the correlation is defined by the drag correlation of Yuen and Chen [26]:

$$C_D = \begin{cases} \frac{24}{Re_p} \left(1 + \frac{Re_p^{2/3}}{6} \right) & Re_p < 1000 \\ 0.424 & Re_p > 1000 \end{cases} \quad (2)$$

The particle size is smaller than the largest unresolved scales, which means that the effect of the unresolved scales on the particle trajectory has to be considered. This is done by an additional term added to the particles' velocity equation as

$$d\mathbf{u}_p = \mathbf{F}_D dt + \mathbf{F}_G dt + \sqrt{C_o \frac{k_{SGS}}{\tau_t}} d\mathbf{W} \quad (3)$$

The last term on the RHS of (3) represents the influence of the subgrid scales on the particle motion, where C_o is the dispersion constant and k_{SGS} is the unresolved kinetic energy of the gas phase, which can be obtained from the assumption of equilibrium of the subgrid scales by $k_{SGS} = 2\Delta C_s^{2/3} \tilde{S}_{ij} \tilde{S}_{ij}$. The turbulent particle relaxation time τ_t is written as

$$\tau_t = \tau_p \left(\frac{\tau_p k_{SGS}^{1/2}}{\Delta} \right)^{0.6} \quad (4)$$

where τ_p is the particle relaxation time, given by

$$\tau_p = \frac{4}{3} \frac{\rho_p}{\rho_g} \frac{1}{C_D |\mathbf{u}_g - \mathbf{u}_p|} \quad (5)$$

Finally, $d\mathbf{W}$ represents the incremental *Wiener* process, which is sampled from a normal distribution with zero mean and standard deviation of \sqrt{dt} [27]. The particle position \mathbf{x}_p evolves according to $d\mathbf{x}_p = \mathbf{u}_p dt$.

3.2. Particle Heat Balance. The timescale of heat conduction inside the particle is typically much higher than that of convection on the surface of the particle; therefore no internal temperature gradients are considered. In these conditions, the particle temperature can be obtained from the balance of heat transfer on the particle surface (convection and radiation) and internal consumption and generation of energy (drying and char combustion). The heat exchange between

TABLE 2: Properties of coal and straw [5].

Fuel properties	Coal	Straw
<i>Proximate Analysis (wt%)</i>		
Moisture (ar)	2.1	7.7
Volatiles (db)	40.6	79.5
Fixed carbon (db)	51.5	15.6
Ash (db)	7.89	4.91
<i>Ultimate Analysis (% wt, ar)</i>		
Carbon	74.8	47.3
Hydrogen	5.08	5.68
Oxygen	10.1	41.6
Nitrogen	1.53	0.54
Sulfur	0.58	<0.01
HHV (kJ/kg, db)	29810	17750

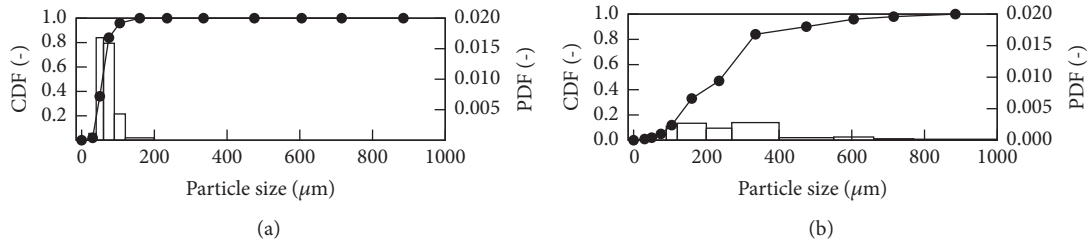


FIGURE 2: Particle size distribution represented by cumulative distribution function (CDF) and probability density function (PDF): (a) coal; (b) biomass.

the particle and the surrounding gas due to convection through the surface of the particle is given by

$$\dot{Q}_{conv} = \theta \frac{Nu}{Pr} \frac{c_{p,g}}{c_{p,p}} \frac{1}{\tau_m} (T_g - T_p) \quad (6)$$

where $c_{p,g}$ and $c_{p,p}$ are the specific heat of the gas and the particle, respectively, T_g and T_p are the temperature of the gas and the particle, respectively, and $\tau_m = \rho_p d_p^2 / 18\mu$ is the diffusion relaxation time. The Nusselt number is calculated using the Ranz-Marshall correlation, which for spheres is given as

$$Nu = 2 + 0.552 Re_p^{1/2} Pr^{1/3} \quad (7)$$

In addition, a blowing factor θ is included to account for the reduced heat transfer due to mass transfer between the particle and the gas phase [28]. During the drying phase, the particle will lose heat proportionally to the mass of evaporated water \dot{m}_{p,H_2O} and the latent heat of evaporation L_{evap} , calculated from the Watson relation, given by $\dot{Q}_{dry} = -\dot{m}_{p,H_2O} L_{evap}$. During the char combustion phase, heat is generated that contributes to particle heating as $\dot{Q}_{char} = \dot{m}_{p,char} LHV_{char}$. Assuming that the char is pure carbon, the heating value takes the value 32.76 MJ/kg. The radiative heat exchange between the particle and its surroundings is given by

$$\dot{Q}_{rad} = A_p \epsilon_p (4\pi I_{b,p} - G) \quad (8)$$

where the particle emissivity is denoted by ϵ_p , the particle black body intensity is denoted by $I_{b,p}$, and the total incident radiation is denoted by G .

3.3. Devolatilization. The direct coupling of detailed multistep devolatilization models to LES results in significant costs when simulating large-scale facilities. Empirical models offer cost effectiveness but require model constants which are specific to both the fuel and the heating conditions. In this work, the model constants of empirical models were calibrated to the specific fuel and heating conditions using predictions of detailed multistep devolatilization models for coal and biomass as reference data, following the same method proposed by Vascellari et al. [17], and applied for a large-scale coal flame by Rabaçal et al. [18].

The phenomenological network model CPD developed by Grant et al. [14], for coal, and the mechanistic model Bio-PoliMi developed by Ranzi and coworkers [15], for biomass, were used to obtain the reference devolatilization rates and yields. Specific composition parameters are required as an input for both models that can be calculated from the proximate and the ultimate analysis of the fuels. In the case of CPD, the correlation developed by Genetti et al. [29], based on a database of 30 coals, is used to obtain the average coal chemical structural properties: the average molecular weight per side chain, the average molecular weight per aromatic cluster, the ratio of bridges to total attachments, and the total attachments per cluster. In the case of Bio-PoliMi, the triangulation method proposed by Cuoci et al. [30] is used to

obtain the composition of the biomass in terms of its main components: cellulose, hemicellulose, and lignin.

Two empirical formulations have been considered to describe devolatilization in LES. The well established and cost-effective SFOR is used as a reference, where only one global decomposition reaction is considered and it is expressed as

$$\frac{dV}{dt} = k(V^* - V), \quad \text{with } k = A_0 \exp\left(-\frac{E_a}{RT_p}\right) \quad (9)$$

where V is the mass fraction of volatiles released up to time t and V^* is the total volatile content. The reaction constant k is given by the Arrhenius expression, where A_0 is the preexponential factor, E_a is the apparent activation energy, R is the ideal gas constant, and T_p is the particle temperature.

In the DAEM formulation, a large number of independent parallel reactions is considered. The contribution of the i^{th} reaction is described by a first-order reaction:

$$\frac{dV_i}{dt} = k_i(V_i^* - V_i), \quad \text{with } k_i = A_0 \exp\left(-\frac{E_{a,i}}{RT_p}\right) \quad (10)$$

The amount of volatiles released in each reaction is obtained by integration of (10). Assuming that the preexponential factor remains constant and that the number of reactions is large enough to allow the distribution of energy to be expressed as Gaussian distribution with a mean activation energy E_0 and a standard deviation σ , the total amount of volatiles released up to a certain time t can be described as

$$V^* - V = \frac{V^*}{\sigma(2\pi)^{1/2}} \int_0^\infty \exp\left[-A_0 \int_0^t \exp\left(-\frac{E}{RT}\right) dt - \frac{(E - E_{mean})^2}{2\sigma^2}\right] dE \quad (11)$$

Equation (11) is discretised using the Modified Gauss-Hermite Quadrature method [20] using four quadrature nodes.

Figure 3 illustrates the calibration process. In the first LES run, SFOR is used considering an initial guess is considered for the model constants. In this work, the preexponential factors and activation energies used by Yin et al. [9] for coal and biomass were used as the initial guess. From the first LES, several particle heating rates from coal and biomass are extracted in order to obtain three representative heating profiles. In the next iteration, the devolatilization rates and yields are calculated with the predictive CPD and PoliMi models by imposing the heating profiles extracted from the previous iteration. The resulting devolatilization yields $Y_{i,j}^{pred}$, obtained for $i = 1, N_i$ heating profiles and $j = 1, N_j(i)$ time steps, are the reference data for the current iteration to calibrate the model constants of SFOR and DAEM. The devolatilization yields $Y_{i,j}^{emp}$ are calculated with the empirical models considering a set of model parameters x_k (A_0 and E_a for SFOR, A_0 , E_{mean} , and σ for DAEM). The calibration of the

model parameters is achieved by minimising the following objective function OF with a genetic algorithm:

$$\text{OF}(x_k) = \frac{1}{N_i} \sum_{i=1}^{N_i} \left(\frac{\sum_{j=1}^{N_j(i)} [Y_{i,j}^{pred} - Y_{i,j}^{emp}(x_k)]^2}{N_j(i) [\max_j(Y_{i,j}^{pred}) - \max_j(Y_{i,j}^{emp})]} \right) \quad (12)$$

More details on the calibration method can be found in the work of Vascellari et al. [17]. An LES is subsequently performed using the calibrated model constants obtained in the current iteration and new particle heating rates for the next iteration are obtained. In this study, only 2 iterations steps were required to achieve convergence of the particle heating profile, as in previous studies [17, 18].

3.4. Char Combustion. The instantaneous burning rate of an individual particle due to char combustion is modelled based on the assumption of a reacting particle surrounded by a chemically frozen boundary layer, the single film assumption. For the present test case, where 80% of the coal particles are under 130 μm in diameter, this assumption is adequate. Biomass particles are larger, but given their significantly lower fixed carbon content, the impact of biomass char combustion on the gas phase is much less pronounced than that of coal. The combustion of lignocellulosic chars has been shown to be analogous to coal char combustion [22] and therefore both coal and biomass chars are assumed to be pure carbon. The effects of ashes (catalytic and thermal) are neglected in this work. For both coal and biomass, CO is assumed as the only product of char combustion and the char consumption rate was modelled using the Smith model [31] where both kinetic and diffusion rate limitations are considered:

$$\dot{m}_{char} = \pi d_p^2 p \tilde{X}_{O_2} \frac{R_{diff} R_{kin}}{R_{diff} + R_{kin}} \quad (13)$$

where the product $p \tilde{X}_{O_2}$ is the partial pressure of oxygen in the gas surrounding the particle. The bulk molecular mass diffusion rate is given:

$$R_{diff} = \frac{C_{diff} T_m^{0.75}}{d_p} \quad (14)$$

where T_m is the average temperature between the particle and the surrounding gas. The chemical rate depends on both the intrinsic chemical rate and pore diffusion as

$$R_{kin} = \eta \left(\frac{d_p}{6} \right) \rho_p A_s k_i \quad (15)$$

where η is the ratio of the real combustion rate to the rate achievable if no pore diffusion resistance existed, A_s is the specific internal surface area, and k_i is the intrinsic reactivity rate constant. The latter is calculated as $k_i = A_i \exp(-E_i/RT_p)$, with the values of the intrinsic preexponential factor A_i and intrinsic activation energy E_i based on a line of best fit of several chars standardised at an oxygen

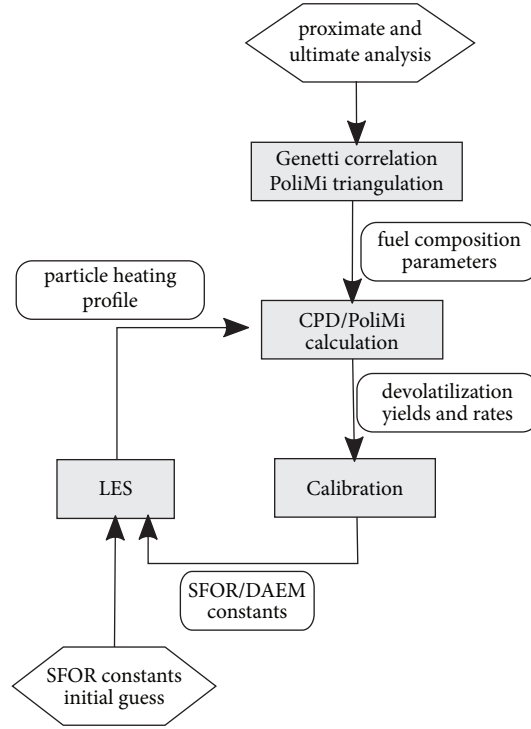


FIGURE 3: Flowchart of the calibration process. Adapted from [17].

partial pressure of 1 atm [31], specifically $305 \text{ g/cm}^2\text{s(atm)}^1$ and 42.8 Kcal/mol , respectively. The effectiveness factor can be related to the Thiele modulus η for a first-order irreversible reaction in a spherical porous particle:

$$\eta = \frac{3}{\phi} \left(\frac{1}{\tanh \phi} - \frac{1}{\phi} \right) \quad (16)$$

The Thiele modulus is defined as

$$\phi = \frac{d_p}{2} \sqrt{\frac{s_{char} \rho_p A_s p \bar{X}_{O_2} k_i}{D_{eff} p \bar{X}_{O_2}}} \quad (17)$$

where $s_{char} = 1.33$ is the stoichiometric coefficient assuming that CO is the only product of char combustion. Mitchell et al. [23] have shown that the relation $\eta - \phi$ described by (16) can accurately describe the effect of pore diffusion resistance under zone I, moderate zone II, and intense zone II oxidising conditions. Additionally, D_{eff} is the effective overall oxygen pore diffusion coefficient evaluated with the combined effects of bulk and Knudsen diffusion of oxygen through pores as described by the Bosanquet relation:

$$D_{eff} = \left(\frac{1}{D_{O_2}} + \frac{1}{D_{Kn}} \right)^{-1} \quad (18)$$

Following previous work [32], a tree pore model that describes the evolution of the specific area of the char with

increasing char conversion is used, which is based on the fractional conversion of carbonaceous material x_c :

$$\frac{A_s}{A_{s,0}} = (1 - x_c) \sqrt{\frac{x_c}{\theta_c} + (1 - x_c)} \quad (19)$$

During char combustion in large-scale applications, char combustion typically proceeds between burning zones II and II. In this work, two different approaches were used to describe density and diameter variation with particle conversion. In the first approach, the classical power law mode is used:

$$\frac{\rho_p}{\rho_{p,0}} = \left(\frac{m_C}{m_{C,0}} \right)^\alpha \quad (20)$$

$$\frac{d_p}{d_{p,char}} = \left(\frac{m_C}{m_{C,0}} \right)^\beta \quad (21)$$

The parameters in (20) and (21) are related by the expression $\alpha + 3\beta = 1$ for spherical particles. For char burning under zone II, α takes the constant value of $1/3$. Mitchell et al. [23] showed that the power law mode is prone to failure in predicting the variations in size and apparent densities of char particles undergoing oxidation in a moderate zone II burning regime. The second approach used in this work has been introduced very recently by Haugen and Mitchel [24], who derived a parameter-free model. In this model, a characteristic time τ is defined as the time taken for the mass in this outermost shell of the particle to be completely consumed (initial stages of char combustion). Based on the assumption that the

reactivity at the outer shell of the particle and the effectiveness factor η are independent, the characteristic time corresponds to the one when conversion equals the effectiveness factor. When the characteristic time has passed, the assumption of a large Thiele modulus ($\phi > 4$) allows the derivation of the relationship $\alpha = \eta$. Finally, the radius and density variation are given by

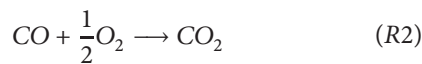
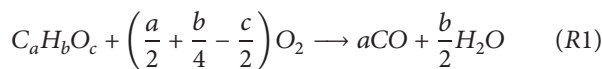
$$\frac{dr_p}{dt} = \begin{cases} 0 & \text{if } t < \tau, \\ \frac{dm_C}{dt} \frac{1-\eta}{4\pi r_p^2 \rho_p} & \text{if } t \geq \tau. \end{cases} \quad (22)$$

$$\frac{d\rho_C}{dt} = \begin{cases} \frac{dm_C}{dt} \frac{1}{V_p} & \text{if } t < \tau, \\ \frac{dm_C}{dt} \frac{\eta}{V_p} & \text{if } t \geq \tau. \end{cases} \quad (23)$$

In this work, the first approach using the power law and a constant α is named a constant conversion mode model, while the second approach is called a variable conversion mode model. In order to isolate the effects of the conversion mode and exclude any other source of variability in the char combustion rate, the char characteristics (porosity, tortuosity, and initial specific surface area) are kept the same for both fuels based on typical high-volatile bituminous coal values used in the previous study [18].

3.5. Gas Phase Combustion. The volatiles from each fuel are represented by a postulate substance $C_aH_bO_c$, which respects the proximate and ultimate analysis in a dry ash free (daf) and sulphur and nitrogen free (snf) basis, respectively, and assuming that the fixed carbon consists of pure carbon, as described by Hashimoto et al. [16]. The molecular weight of the coal volatiles is assumed as 50 kg/kmol [17], whereas for the case of biomass it is assumed as 20 kg/kmol. The low heating value of the volatile matter is obtained from $LHV_{vol} = (LHV_{fuel} - Y_{FC,daf} LHV_{FC}) / Y_{VM,daf}$, with $LHV_{FC} = 32.76$ MJ/kg. Considering the global combustion reaction of the postulate volatiles with air, and assigning the low heating value of the fuel as the heat of reaction, the standard enthalpy of formation of the postulate volatiles can be calculated based on the enthalpy balance of the global combustion reaction.

The homogeneous combustion is reduced to a two-step mechanism for both fuels. The reactions (R1) and (R2) describe the oxidation of volatiles and carbon monoxide, respectively.



The turbulence-chemistry interaction on the subgrid level is described using the Eddy Break Up model [33]. The reaction rate is dependent on the inverse mixing time, which is calculated from the resolved strain rate tensor using $1/\tau = |\tilde{S}| = \sqrt{2\tilde{S}_{ij}\tilde{S}_{ij}}$, as proposed by Hu et al. [34].

3.6. Radiation. The general radiative transfer equation is solved using the discrete ordinates method [35–37], being discretized and solved for 24 directions using the S_4 approximation. The participating medium's spectral properties are modelled using a weighted-sum-of-gray-gases model [38]. The particle's absorption coefficients κ_p and scattering coefficient σ_p in a given computational cell are defined according to Chui et al. [37]:

$$\kappa_p = \epsilon_p \sum_{i=1}^N \frac{\pi d_{p,i}^2}{4} \quad (24)$$

$$\sigma_p = (1 - \epsilon_p) \sum_{i=1}^N \frac{\pi d_{p,i}^2}{4} \quad (25)$$

where ϵ_p depends on the char-burnout and the proportions of volatile content and ash found in the particle [37]. Equations (24) and (25) are valid for large, grey, and diffuse particles. Only particle scattering is considered as this is largely dominant over gas, soot, and fly-ash scattering. Furthermore, throughout this work only isotropic scattering is considered. For the experimental test cases used in this work, considering the measured and predicted temperatures and the smallest particle diameter (15 μm), it can be estimated that only negligible amounts of emitted radiative energy are on the wavelengths where the large particle assumption fails.

4. Numerical Setup

The in-house code PsiPhi [18, 25, 39–43] was used to solve the implicitly filtered, low-Mach number Navier Stokes equations for a variable density flow. PsiPhi ensures continuity by a pressure-correction scheme using a projection method. A Cartesian, equidistant grid is used, providing good numerical accuracy, isotropic filtering, high parallel efficiency, and good vectorisation through avoiding slow, nonsequential memory access. The configuration allows decomposing the domain into blocks for maximum efficiency during MPI communication between CPUs.

The convective fluxes are approximated with a 2nd-order central differencing scheme for momentum and a total variation diminishing scheme for scalars. A low storage, explicit Runge Kutta scheme is used for time-integration with a CFL number of 0.3 to ensure accuracy and stability. The particle motion is embedded into the Runge-Kutta procedure of the LES code and the coupling between particle and LES fields is done by trilinear interpolation schemes.

In this work, a particle parceling strategy was applied to achieve a compromise between accuracy and computational cost. Given the biomass mass flow input and the biomass particle size distribution (c.f. Figure 2), approximately ten particles are injected per time step. As for coal particles, approximately 200 particles are injected per time step. While the order of magnitude of the number of physical biomass particles injected per time step is affordable, in the case of physical coal particles that number is too large. Therefore ten physical coal particles are parcelled into one numerical particle. The particles were injected in the domain using a

TABLE 3: Numerical test case setup list.

Test case	Devolatilization	Conversion mode
SC	SFOR	Constant
DC	DAEM	Constant
SV	SFOR	Variable

TABLE 4: Optimised model constants of the empirical devolatilization models.

	Coal	Biomass		Coal	Biomass
<i>SFOR</i>			<i>DAEM</i>		
A_0	1.95×10^5	1.19×10^8	A_0	12.29	8.73
E	7.775×10^3	13.418×10^3	E_{mean}	192.47	125.09
Q	0.5558	0.8475	σ	26.75	4.73
			Q	0.5598	0.8476

random distribution fitted to the particle size distribution and randomly positioned within the injection plane.

The closure of the subgrid stress tensor is ensured through the eddy viscosity approach, where the turbulent viscosity is modelled using the Smagorinsky-Lilly model [44]. The model constant takes the value 0.173. Pseudo-turbulent inflow conditions were generated using an efficient implementation of Klein's turbulence generator [45], for a turbulence level of 10% for the fluctuation magnitude. Inlets mean velocities were assigned using a 7th-power law profile matching the mass flow of each stream.

Immersed boundaries describe the furnace walls and no additional wall modelling was attempted as the flame burns away from the walls and as the wall roughness is hardly known. A wall temperature profile was imposed to the immersed boundaries (D. Tree, personal communication). The furnace geometry was described by an equidistant Cartesian mesh with 2250x750x750 mm in size using a cell size of $\Delta = 3.0$ mm. This resolution has been shown to provide reasonable predictions of a coal flame in a furnace and burner of similar dimensions, operating under similar conditions [18]. The grid has a total of 40 million cells and 1024 cores were used in SuperMUC (LRZ, Munich, Germany). Statistics were collected after 5 seconds of initialisation over a period of 1 second. The numerical cost of each run was 100 thousand CPUh and 3 runs were necessary for the iterative optimisation process, corresponding to a total of 0.5 million CPUh. Three numerical setups were simulated, listed in Table 3, varying the devolatilization model and the char combustion mode model.

5. Results

5.1. Single Particle Conversion under Idealised Conditions. Figures 4 and 5 show the total yield and rate curves of devolatilization for coal and biomass, respectively. The optimised constants are given in Table 4, where the Q factor refers to the ratio between the total volatile yield predicted by CPD and PoliMi under the heating conditions retrieved from the LES and the total volatile yield reported by the proximate analysis. Note that the latter is obtained following measuring standards where the heating rates and maximum

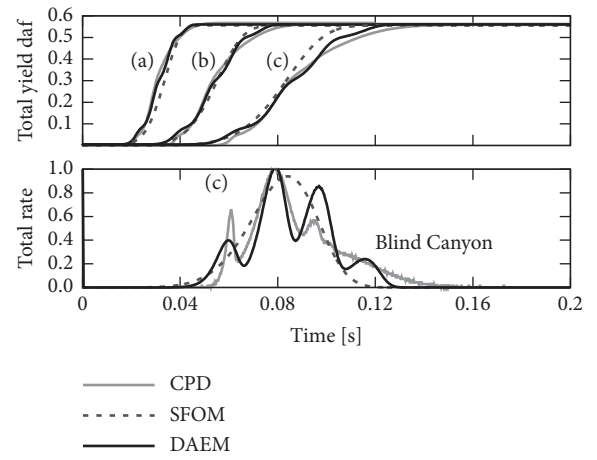


FIGURE 4: Coal devolatilization. Top: total yield (daf); down: total rate (daf) normalised by the maximum value of the CPD rate. (a) From 300 to 1700 K in 0.06 s, (b) from 300 to 1600 K in 0.1 s, and (c) from 300 to 1500 K in 0.15 s.

temperatures are far from those in typical large-scale combustion (e.g., ASTM D3172 and ASTM E872). Note that coal and particles are exposed to different heating rates due to the different particle size distributions (see Figure 2). Both coal and biomass particles of similar size are subjected to heating rates in the order of 1×10^4 K/s, whereas larger biomass particles are additionally subjected to heating rates in the order of 1×10^3 K/s given their broader size distribution. Coal devolatilization presents several rate peaks whereas biomass presents one single peak at such high heating rates. In the case of coal, the DAEM curve presents better agreement with the CPD curve than that of SFOR. In the case of biomass, both calibrated curves present a good agreement with the PoliMi curve.

Figure 6 shows the effect of the conversion mode modelling approach on the char conversion, normalised density, and normalised diameter variation during char conversion of a single particle. A char particle with 100 μm in diameter was immersed in an atmosphere with 6% O_2 and at two temperatures, 1200 K and 1500K, corresponding

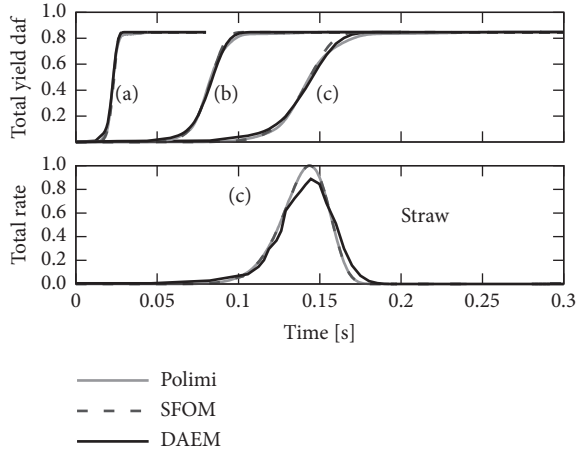


FIGURE 5: Biomass devolatilization. Top: total yield (daf); down: total rate (daf) normalised by the maximum value of the CPD rate. (a) From 300 to 1600 K in 0.04 s, (b) from 300 to 1500 K in 0.15 s, and (c) from 300 to 1400 K in 0.25 s.

to a moderate and an intensive zone II burning mode, respectively.

The conversion mode model affects the char diameter and density but has little influence on the burnout time. The trends obtained with the variable conversion mode are in good agreement with the ones obtained by Haugen and Mitchell [24] for similar conditions. At the lower temperature of 1200 K, both models predict a similar variation of the diameter, although a small deviation can be observed in the latter stages of conversion. The density variation curves present a more pronounced deviation throughout conversion. At the higher temperature of 1500 K, the diameter and density variation show clear deviations between conversion models. Under an intensive zone II burning mode (1500 K), where it is expected that the density variation is close to that of a shrinking core mode, the variable conversion mode yields reasonable results.

5.2. Particle Conversion in the Furnace Simulations. Figure 7 shows the LES instantaneous devolatilization rate over time of a particle ensemble collected at 6 seconds of physical run time for the cases SC and DC, cf. Table 3. When SFOM is used for calibration (Figures 7(a) and 7(c)), corresponding to case SC, the devolatilization of each fuel type occurs mainly within a narrow location. When DAEM is used for calibration (Figures 7(b) and 7(d)), corresponding to case DC, devolatilization of both fuels spans through a longer axial distance and maximum rates decrease slightly. Since the local distribution of volatiles in the furnace affects the local gas phase mixture composition, these results provide a first indicator of the effect of the devolatilization model on the gaseous flame length, for the studied conditions.

Figure 8 shows the LES instantaneous normalised particle diameter, density, temperature, and velocity magnitude during char conversion of a particle ensemble collected at 6 seconds of physical run time for the cases SC and SV (cf. Table 3). Particle temperature is normalised using

the maximum temperature obtained in case SC and the analogous normalisation is applied to the velocity magnitude. Figures 8(c) and 8(d) show that the conversion mode model has an influence on the particles aerodynamic properties, as typified by the particle velocity variation during conversion. As a consequence, local char burning conditions will vary yielding the differences observed in the particle temperature during char combustion, as seen in Figures 8(a) and 8(b).

5.3. Effects of the Particle Conversion Model on the Flame Structure. Figure 9 shows the instantaneous radial mid-plane gas phase temperature distribution corresponding to 2.5 seconds of physical runtime, sufficient for the establishment of the gaseous flame. The temperature is used as an indicator of regions where intense heat release occurs and hence where combustion reactions are taking place. Figures 9(a) and 9(c) show that when using SFOR the reactions occur in a well defined envelope enclosing the internal recirculation zone and further downstream pockets of cold unreacted gas. On the other hand, Figure 9(b) shows that when using DAEM the high temperature regions are broader and spacial gradients are less intense downstream of the internal recirculation zone. Finally, Figure 9 shows that the flame lift-off height is marginally affected by the devolatilization model in the studied conditions, as typified by the early onset of reactions within the quarl.

Figures 10 and 11 show experimental and numerical maps of CO_2 and O_2 mean concentration, respectively. The experimental maps show that the flame has a large volume, extending axially beyond 125 cm, and expanding outward radially for 15–20 cm. This large flame volume can be explained by several factors, namely, [5]: (1) given the low energy density in mass base of biomass, considerable mass flows of transport air need to be used to supply the furnace with a certain thermal input; therefore particles will be fed with a high momentum that allows the particles to penetrate through the internal recirculation zone; (2) large biomass particles, as compared to coal, typically show higher volatile yields and longer devolatilization times, spreading the reaction of the biomass particles over a larger volume; (3) the high volatile yields of biomass create local fuel-rich volumes in a section of the furnace where mixing is more limited due to the low gas velocities, which limits the homogenous gas-phase reactions. Another interesting aspect of the structure of flame is the “break” occurring between 20 and 35 cm. Damsteadt [5] attributes the occurrence of the “break” to the characteristics of the biomass used in the study. Straw contains two main structures: stalks and knees. The knees are much harder and less porous than the stalks. Upon grinding, the shape of the knees is near spherical, while the stalks are either flake-like or cylindrical. The knees proceed mostly unreacted through the internal recirculation zone into the lower regions of the reactor, where sufficient time in the hot reactor environment has elapsed to begin the combustion process. When comparing the different devolatilization models, specifically the cases SC and DC, it is possible to see that the flame break is only captured when DAEM is used. Furthermore, it is possible to observe in both figures the effect of large biomass particles that

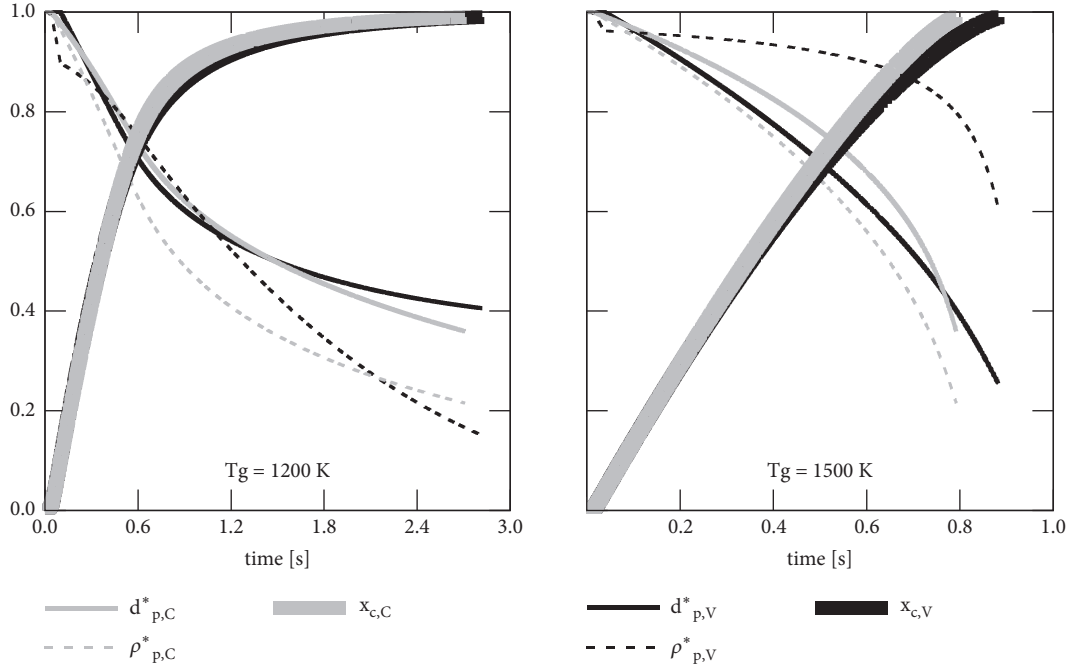


FIGURE 6: Time evolution of char conversion (x_c), normalised diameter ($d_p^* = d_p/d_{p,0}$), and normalised density ($\rho_p^* = \rho_p/\rho_{p,0}$) of a single particle char immersed in an atmosphere with 6% O_2 at 1200 K. The subscripts C and V denote constant conversion mode and variable conversion mode, respectively.

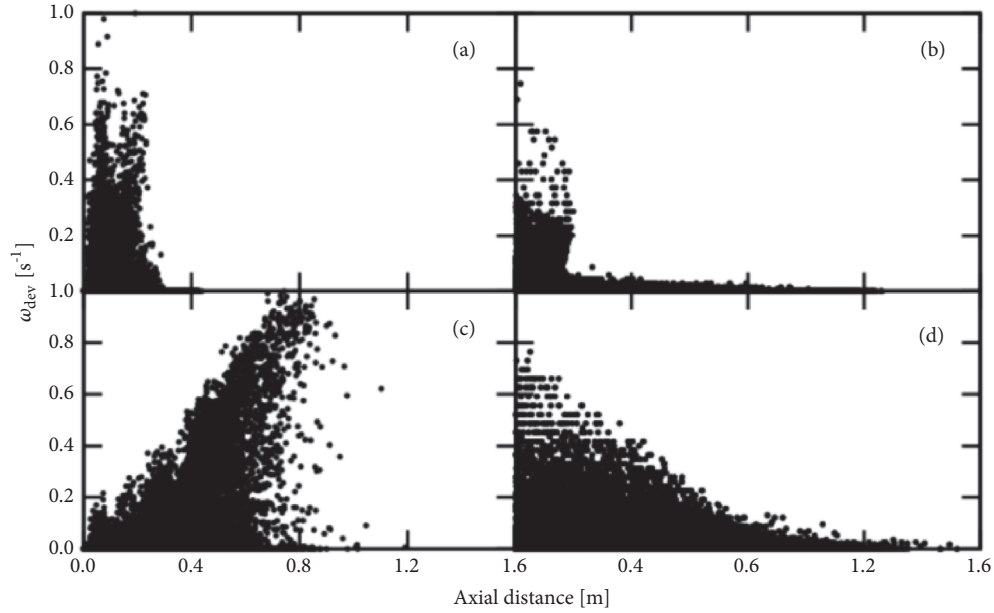


FIGURE 7: Devolatilization rate along the axial direction of the furnace: (a) SC coal, (b) DC coal, (c) SC biomass, and (d) DC biomass. Rates normalised by maximum rate obtained with SFOM of corresponding fuel. Particle ensemble collected after 6 seconds of physical runtime.

are marginally affected by the internal recirculation zone, penetrating through it and travelling downwards. The results indicate that SFOR overpredicts the devolatilization rates close to the burner yielding a faster burnout of coal and biomass particles. In parallel, gas-phase reactions are also more intense resulting in a larger radial expansion of the internal recirculation zone. In contrast, the case DC shows

a radially compact internal recirculation zone where smaller particles are entrained and burn, and a radially compact secondary reaction zone after the flame break, owing to a more distributed volatile release as shown in Figure 7. Note that Figure 7 shows that the location in the furnace where the maximum devolatilization rate occurs varies depending on the choice of the devolatilization model. Essentially, it shows

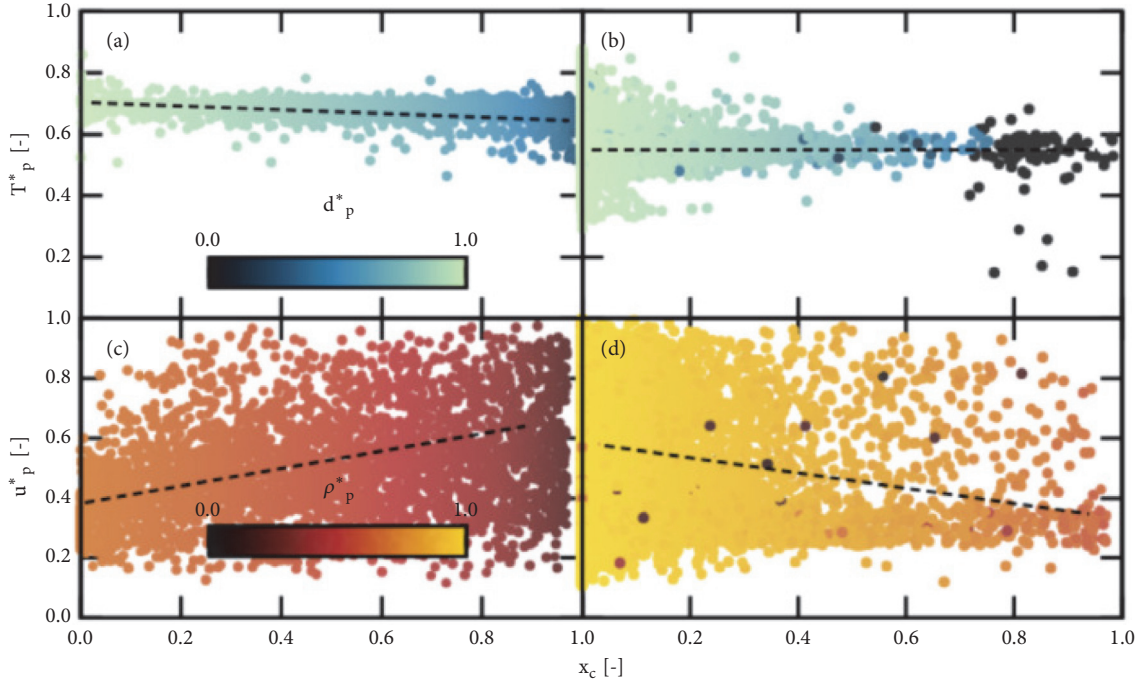


FIGURE 8: Normalised diameter, density, velocity magnitude ($u_p^* = u_p/u_{p,max}$), and particle temperature ($T_p^* = T_p/T_{p,max}$) variation during char conversion as a function of particle temperature: (a) and (c) SC, (b) and (d) SV. Particle ensemble collected after 6 seconds of physical runtime.

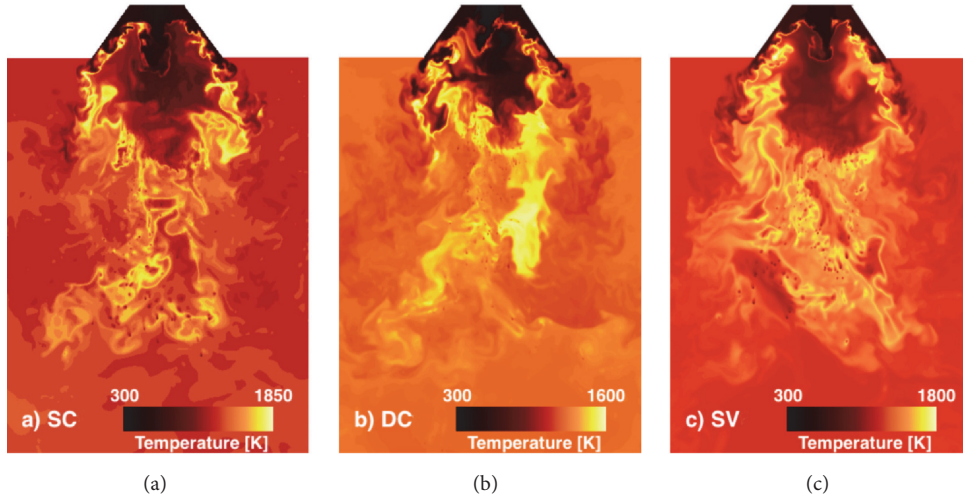


FIGURE 9: Instantaneous radial mid-plane gas phase temperature distribution corresponding to 2.5 seconds of physical runtime, sufficient for the establishment of the gaseous flame. Note that only the region of interest is shown, corresponding to a third of the diameter and half of the length. From left to right: SC, DC, and SV.

that with SFOR the predicted devolatilization rates occur very close to the burner exit and the devolatilization process is over at 400 mm. Experimentally, the flame break is observed at approximately 250 mm, downstream of which large particles go through devolatilization creating the second flame. This is captured by the DAEM in both Figure 7 and Figures 10 and 11. The O_2 and CO_2 maps obtained with the cases SC and SV show that under these conditions the average spatial distribution of the major species is not affected by the choice of the char combustion mode model, which is a result of high

intensity reaction zone in the upper region of the furnace leading to early burnout under high temperatures.

Figure 12 shows a comparison between the experimental measurements and the numerical predictions of O_2 and CO_2 . The flame showed considerable asymmetry; therefore absolute comparisons between measurements and predictions should be regarded as qualitative. In order to minimise the asymmetry, points and corresponding error bars show the mean and standard deviation of measurements performed at opposing, radially symmetric locations. The predictions

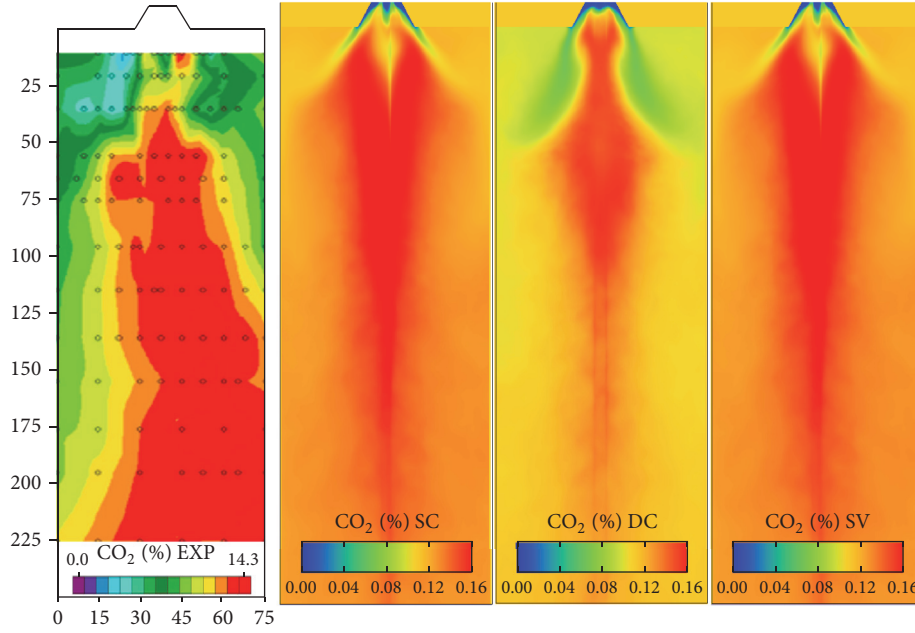


FIGURE 10: Experimental (adapted from [5]) and numerical maps of CO_2 concentration. Dimensions on the the left are given in centimetres.

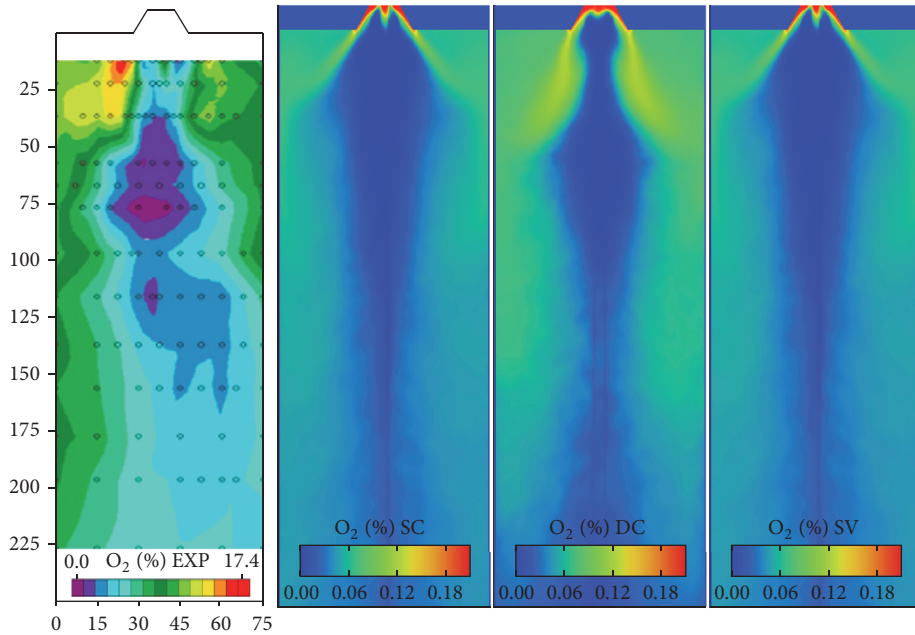


FIGURE 11: Experimental (adapted from [5]) and numerical maps of O_2 concentration. Dimensions on the the left are given in centimetres.

from the cases SC and DC show that the devolatilization model has a pronounced effect in the flame structure, whereas the char conversion mode model does not show significant differences. When SFOR is used, cases SC and SV, it is clear that the overall particle heating and reaction rates are overpredicted, given the underprediction of O_2 and the overprediction of CO_2 . Furthermore, the particle burnout at the exit of the domain in those cases was close to 100%, but qualitative analysis of the experimentally collected char at the exit of the furnace showed that biomass, particularly the

knees, showed limited burnout levels. When using DAEM, the predictions are closer to the experimental results and burnout levels at the exit of the computational domain are in the order of 60%.

6. Conclusions

A study on the effect of the devolatilization model and char combustion mode model on the structure of a large-scale laboratory coal and biomass flame is presented. Two

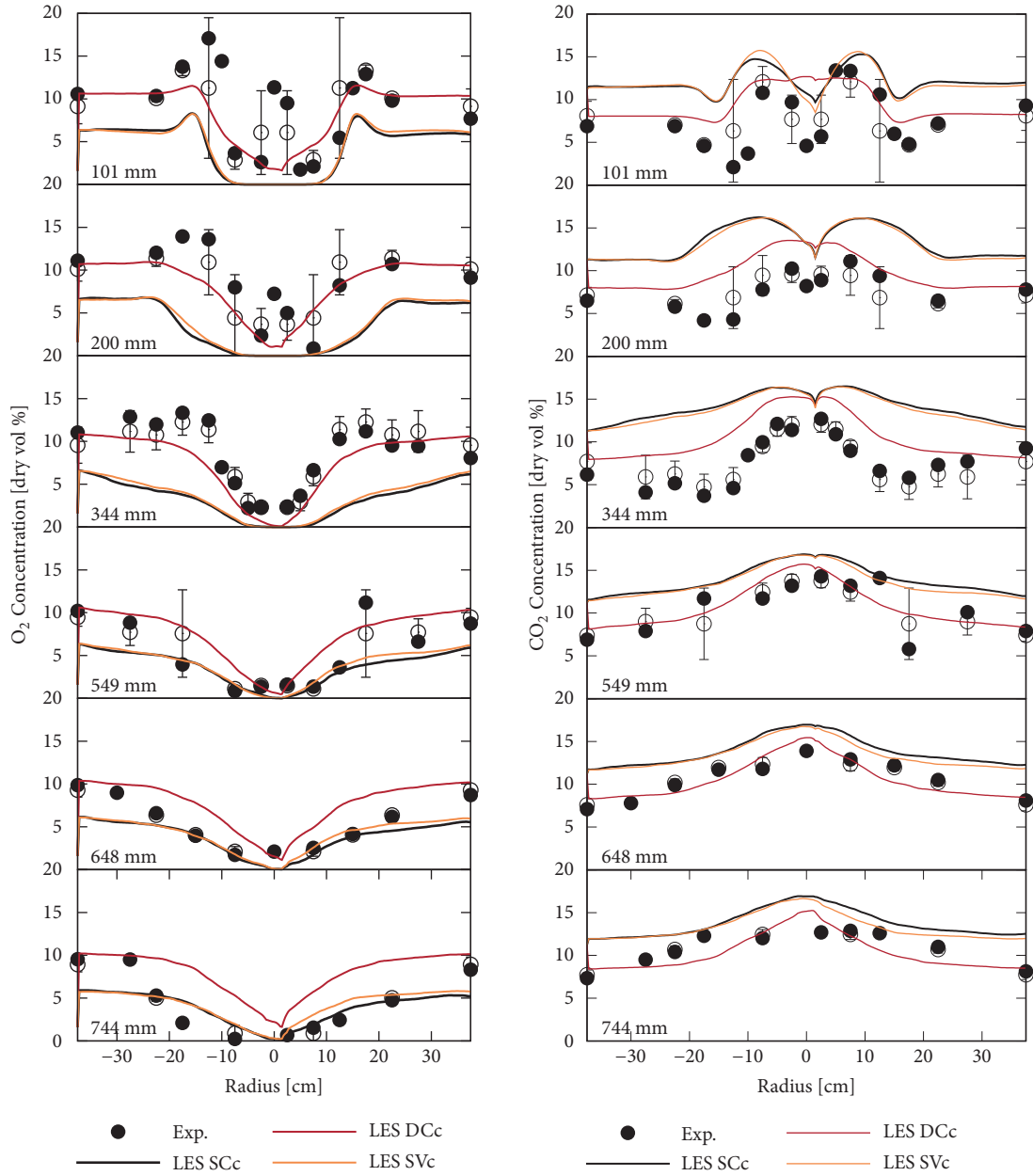


FIGURE 12: Comparison between measurements and predictions of O_2 (left) and CO_2 (right) for the modelling cases SCc, DCc, and SVc. Empty points and corresponding error bars show the mean and standard deviation of measurements performed at opposing, radially symmetric locations.

devolatilization models were tested, single first-order reaction and distributed activation energy, and two char conversion modes were tested: power law mode with a model constants and a constant-free model. Single particle simulations under idealised conditions were performed to evaluate the impact of the different models in the absence of turbulence. Subsequently, large eddy simulations were performed and the results were compared with experimental results. Three numerical cases were considered: single first-order reaction with constant char combustion mode, distributed activation energy with constant char combustion mode, and single first-order reaction with variable char combustion mode.

Simulations of single particle conversion under idealised conditions showed that both the devolatilization model and the char conversion mode model had a pronounced effect in the conversion of the particle when using typical furnace conditions, namely, heating rates, temperature, and oxygen concentration. Particle scatter data obtained from the large eddy simulations show that devolatilization tends to occur in a narrow region close to the burner region when using the single first-order reaction devolatilization model, while with the distributed activation energy devolatilization model devolatilization is retarded and occurs along the furnace axial distance. This effect has a profound effect on the

spatial distribution of O_2 and CO_2 , since a more intense and localised devolatilization stage leads to a more intense gas-phase combustion region, resulting in early burnout, strong radial expansion, and shorter flame when using the single first-order reaction devolatilization model. On the other hand, the distributed activation energy devolatilization model was capable of predicting the flame break observed experimentally, resulting in a more radially compact and longer flame. The authors of the experimental work attribute the flame break to particle dynamics, particularly different trajectories followed by the different particle categories; hence the results of this work motivate further investigations on the impact of the devolatilization model on particle dynamics. In what concerns the flame lift-off, in both cases the flame stabilises close to the burner within the quarl area. Finally, owing to the intense reaction zone close to the burner region, the different models used for the char combustion mode had a marginal impact on the spatial distribution of O_2 and CO_2 .

Data Availability

Data presented in the paper is available from the authors on request.

Disclosure

The present address of Miriam Rabaçal is Aerothermochemistry and Combustion Systems Laboratory, ETH Zurich, Switzerland.

Conflicts of Interest

The authors declare that there are no conflicts of interest regarding the publication of this paper.

Acknowledgments

This work was partially supported by Fundação para a Ciência e Tecnologia (FCT), through IDMEC, under LAETA, project UID/EMS/50022/2013 and project PTDC/EMS-ENE/5710/2014. M. Rabaçal acknowledges FCT for the provision of Scholarship SFRH/BD/72583/2010. The authors acknowledge PRACE and the Gauss Centre for Supercomputing for awarding access to SuperMUC based at the Leibniz-Rechenzentrum, Munich, Germany (projects 2013081677 and HLRB pr84mu, respectively). The authors would like to thank Professor Dale Tree from Brigham Young University for the many helpful discussions.

References

- [1] European Climate Foundation, *An Assessment of Advanced Biofuels from Wastes & Residues*, 2010.
- [2] F. Al-Mansour and J. Zuwala, "An evaluation of biomass co-firing in Europe," *Biomass & Bioenergy*, vol. 34, no. 5, pp. 620–629, 2010.
- [3] K. Annamalai, B. Thien, and J. Sweeten, "Co-firing of coal and cattle feedlot biomass (FB) fuels. Part II. Performance results from 30 kWt (100,000) BTU/h laboratory scale boiler burner," *Fuel*, vol. 82, no. 10, pp. 1183–1193, 2003.
- [4] B. Lawrence, K. Annamalai, J. M. Sweeten, and K. Heflin, "Cofiring coal and dairy biomass in a 29 kWt furnace," *Applied Energy*, vol. 86, no. 11, pp. 2359–2372, 2009.
- [5] B. D. Damstedt, *Structure and nitrogen chemistry in coal, biomass, and co-firing low-NOx flames [Ph.D. thesis]*, Brigham Young University, 2007.
- [6] B. Damstedt, J. M. Pederson, D. Hansen et al., "Biomass cofiring impacts on flame structure and emissions," *Proceedings of the Combustion Institute*, vol. 31, pp. 2813–2820, 2007.
- [7] G. Lu, Y. Yan, S. Cornwell, M. Whitehouse, and G. Riley, "Impact of co-firing coal and biomass on flame characteristics and stability," *Fuel*, vol. 87, no. 7, pp. 1133–1140, 2008.
- [8] C. Casaca and M. Costa, "Co-combustion of biomass in a natural gas-fired furnace," *Combustion Science and Technology*, vol. 175, no. 11, pp. 1953–1977, 2003.
- [9] C. Yin, S. K. Kær, L. Rosendahl, and S. L. Hvid, "Co-firing straw with coal in a swirl-stabilized dual-feed burner: Modelling and experimental validation," *Bioresource Technology*, vol. 101, no. 11, pp. 4169–4178, 2010.
- [10] C. Ghenai and I. Janajreh, "CFD analysis of the effects of co-firing biomass with coal," *Energy Conversion and Management*, vol. 51, no. 8, pp. 1694–1701, 2010.
- [11] L. Ma, J. M. Jones, M. Pourkashanian, and A. Williams, "Modelling the combustion of pulverized biomass in an industrial combustion test furnace," *Fuel*, vol. 86, no. 12–13, pp. 1959–1965, 2007.
- [12] S. Black, J. Szuhánszki, A. Pranzitelli et al., "Effects of firing coal and biomass under oxy-fuel conditions in a power plant boiler using CFD modelling," *Fuel*, vol. 113, pp. 780–786, 2013.
- [13] R. I. Backreedy, L. M. Fletcher, J. M. Jones, L. Ma, M. Pourkashanian, and A. Williams, "Co-firing pulverised coal and biomass: A modeling approach," *Proceedings of the Combustion Institute*, vol. 30, no. 2, pp. 2955–2964, 2005.
- [14] D. M. Grant, R. J. Pugmire, T. H. Fletcher, and A. R. Kerstein, "Chemical model of coal devolatilization using percolation lattice statistics," *Energy & Fuels*, vol. 3, no. 2, pp. 175–186, 1989.
- [15] E. Ranzi, A. Cuoci, T. Faravelli et al., "Chemical kinetics of biomass pyrolysis," *Energy & Fuels*, vol. 22, no. 6, pp. 4292–4300, 2008.
- [16] N. Hashimoto, R. Kurose, S.-M. Hwang, H. Tsuji, and H. Shirai, "A numerical simulation of pulverized coal combustion employing a tabulated-devolatilization-process model (TDP model)," *Combustion and Flame*, vol. 159, no. 1, pp. 353–366, 2012.
- [17] M. Vascellari, R. Arora, M. Pollack, and C. Hasse, "Simulation of entrained flow gasification with advanced coal conversion submodels. Part 1: Pyrolysis," *Fuel*, vol. 113, pp. 654–669, 2013.
- [18] M. Rabaçal, B. M. Franchetti, F. C. Marincola et al., "Large Eddy Simulation of coal combustion in a large-scale laboratory furnace," *Proceedings of the Combustion Institute*, vol. 35, no. 3, pp. 3609–3617, 2015.
- [19] M. Rieth, A. G. Clements, M. Rabaçal, F. Proch, O. T. Stein, and A. M. Kempf, "Flamelet LES modeling of coal combustion with detailed devolatilization by directly coupled CPD," *Proceedings of the Combustion Institute*, vol. 36, no. 2, pp. 2181–2189, 2017.
- [20] E. Donskoi and D. L. S. McElwain, "Optimization of coal pyrolysis modeling," *Combustion and Flame*, vol. 122, no. 3, pp. 359–367, 2000.

- [21] J. Cai, W. Wu, and R. Liu, "An overview of distributed activation energy model and its application in the pyrolysis of lignocellulosic biomass," *Renewable & Sustainable Energy Reviews*, vol. 36, pp. 236–246, 2014.
- [22] C. di Blasi, "Combustion and gasification rates of lignocellulosic chars," *Progress in Energy and Combustion Science*, vol. 35, no. 2, pp. 121–140, 2009.
- [23] R. E. Mitchell, L. Ma, and B. Kim, "On the burning behavior of pulverized coal chars," *Combustion and Flame*, vol. 151, no. 3, pp. 426–436, 2007.
- [24] N. E. L. Haugen, M. B. Tilghman, and R. E. Mitchell, "The conversion mode of a porous carbon particle during oxidation and gasification," *Combustion and Flame*, vol. 161, no. 2, pp. 612–619, 2014.
- [25] B. M. Franchetti, F. Cavallo Marincola, S. Navarro-Martinez, and A. M. Kempf, "Large Eddy simulation of a pulverised coal jet flame," *Proceedings of the Combustion Institute*, vol. 34, no. 2, pp. 2419–2426, 2013.
- [26] M. C. Yuen and L. W. Chen, "On Drag of Evaporating Liquid Droplets," *Combustion Science and Technology*, vol. 14, no. 4–6, pp. 147–154, 1976.
- [27] S. B. Pope, "PDF methods for turbulent reactive flows," *Progress in Energy and Combustion Science*, vol. 11, no. 2, pp. 119–192, 1985.
- [28] M. Stöllinger, B. Naud, D. Roekaerts, N. Beishuizen, and S. Heinz, "PDF modeling and simulations of pulverized coal combustion - Part I: Theory and modeling," *Combustion and Flame*, vol. 160, no. 2, pp. 384–395, 2013.
- [29] D. Genetti, T. H. Fletcher, and R. J. Pugmire, "Development and application of a correlation of ¹³CNMR chemical structural analyses of coal based on elemental composition and volatile matter content," *Energy Fuels*, vol. 13, pp. 60–68, 1999.
- [30] A. Cuoci, T. Faravelli, A. Frassoldati et al., "A general mathematical model of biomass devolatilization Note 1. Lumped kinetic models of cellulose, hemicellulose and lignin," in *Proceedings of the 30th Meeting of the Italian section of the Combustion Institute*, 2007.
- [31] I. W. Smith, "The combustion rates of coal chars: A review," *Symposium (International) on Combustion*, vol. 19, no. 1, pp. 1045–1065, 1982.
- [32] A. Williams, R. Backreedy, R. Habib, J. M. Jones, and M. Pourkashanian, "Modelling coal combustion: The current position," *Fuel*, vol. 81, no. 5, pp. 605–618, 2002.
- [33] B. F. Magnussen and B. H. Hjertager, "On mathematical modeling of turbulent combustion with special emphasis on soot formation and combustion," *Symposium (International) on Combustion*, vol. 16, no. 1, pp. 719–729, 1977.
- [34] L. Y. Hu, L. X. Zhou, and J. Zhang, "Large-eddy simulation of a swirling diffusion flame using a SOM SGS combustion model," *Numerical Heat Transfer, Part B: Fundamentals*, vol. 50, no. 1, pp. 41–58, 2006.
- [35] J. S. Truelove, "Discrete-ordinate solutions of the radiation transport equation," *Journal of Heat Transfer*, vol. 109, no. 4, pp. 1048–1051, 1987.
- [36] W. A. Fiveland, "Three-dimensional radiative heat-transfer solutions by the discrete-ordinates method," *Journal of Thermophysics and Heat Transfer*, vol. 2, no. 4, pp. 309–316, 1988.
- [37] E. H. Chui and G. D. Raithby, "Computation of radiant heat transfer on a nonorthogonal mesh using the finite-volume method," *Numerical Heat Transfer, Part B: Fundamentals*, vol. 23, no. 3, pp. 269–288, 1993.
- [38] T. Kangwanpongpan, R. C. da Silva, and H. J. Krautz, "Prediction of oxy-coal combustion through an optimized weighted sum of gray gases model," *Energy*, vol. 41, no. 1, pp. 244–251, 2012, In Proceedings of the 23rd International Conference on Efficiency, Cost, Optimization, Simulation and Environmental Impact of Energy Systems, ECOS 2010.
- [39] O. Stein and A. Kempf, "LES of the Sydney swirl flame series: A study of vortex breakdown in isothermal and reacting flows," *Proceedings of the Combustion Institute*, vol. 31, no. 2, pp. 1755–1763, 2007.
- [40] O. T. Stein, G. Olenik, A. Kronenburg et al., "Towards comprehensive coal combustion modelling for les," *Flow, Turbulence and Combustion*, vol. 90, no. 4, pp. 859–884, 2013.
- [41] F. Proch and A. M. Kempf, "Numerical analysis of the Cambridge stratified flame series using artificial thickened flame LES with tabulated premixed flame chemistry," *Combustion and Flame*, vol. 161, no. 10, pp. 2627–2646, 2014.
- [42] A. Rittler, F. Proch, and A. M. Kempf, "LES of the Sydney piloted spray flame series with the PFGM/ATF approach and different sub-filter models," *Combustion and Flame*, vol. 162, no. 4, pp. 1575–1598, 2015.
- [43] M. Rieth, F. Proch, M. Rabaçal, B. M. Franchetti, F. Cavallo Marincola, and A. M. Kempf, "Flamelet LES of a semi-industrial pulverized coal furnace," *Combustion and Flame*, vol. 173, pp. 39–56, 2016.
- [44] K. Lilly, "On the application of the eddy viscosity concept in the inertial sub-range of turbulence," 1966.
- [45] A. M. Kempf, S. Wysocki, and M. Pettit, "An efficient, parallel low-storage implementation of Klein's turbulence generator for LES and DNS," *Computers & Fluids*, vol. 60, pp. 58–60, 2012.

Research Article

3D Instantaneous Reconstruction of Turbulent Industrial Flames Using Computed Tomography of Chemiluminescence (CTC)

A. Unterberger¹ ,¹ M. Röder,² A. Giese,² A. Al-Halbouni,² A. Kempf¹ ,¹ and K. Mohri¹

¹*Institute for Combustion and Gas Dynamics (IVG) - Chair of Fluid Dynamics, University of Duisburg-Essen, Germany*

²*Gas- und Wärme-Institut Essen e. V. (GWI), Essen, Germany*

Correspondence should be addressed to A. Unterberger; andreas.unterberger@uni-due.de

Received 6 July 2018; Accepted 16 September 2018; Published 29 October 2018

Guest Editor: Xiaoke Ku

Copyright © 2018 A. Unterberger et al. This is an open access article distributed under the Creative Commons Attribution License, which permits unrestricted use, distribution, and reproduction in any medium, provided the original work is properly cited.

Computed Tomography of Chemiluminescence (CTC) was used to reconstruct the instantaneous three-dimensional (3D) chemiluminescence field of a high-power industrial flame, which was made optically accessible, for the first time. The reconstruction used 24 projections that were measured simultaneously, in one plane and equiangularly spaced within a total fan angle of 172.5°. The 3D results were examined by plotting both vertical and horizontal slices, revealing highly wrinkled structures with good clarity. The results presented are one of a series of experimental demonstrations of CTC applications to turbulent gaseous flames. The work reveals the potential to use any kind of luminescence measurement, such as emission from heated particles in coal-fired flames, for analysis of the flame shape directly in 3D.

1. Introduction

The use of fossil fuels such as coal remains to be the main source in today's power generation and likely to continue being so for the coming decades. However, conventional coal combustion is accompanied with harmful pollutants that disturb our environment and contribute to global warming. Hence, much scientific effort and investment is being increasingly dedicated to the development of cleaner and more efficient coal-burning technologies. In this context, there is a need for advanced monitoring techniques for the relevant flames, which are typically turbulent and inherently unsteady and three-dimensional (3D). Therefore, instantaneous volumetric data is key to obtaining in-depth knowledge of such flames to facilitate optimising coal combustion efficiency with respect to energy and pollutant production. The flame shape and expansion as well as temporal fluctuations, e.g., combustion instabilities, are examples of important information that will aid in the development and optimisation of the thermal processes involved.

Several non-intrusive flame diagnostic techniques such as laser-based ones currently exist, which were originally developed to deliver planar information. In principle, it is possible to use complex experiments constituting high-speed cameras, lasers, and rotating mirrors, to obtain time-resolved 3D information about species and temperature from multiple quasi-instantaneous light-sheet measurements [1, 2]. Nonetheless, this approach is very expensive and challenging. On the other hand, the CTC technique [3, 4] can calculate at least the instantaneous spatially and temporally resolved flame shape information directly in 3D, using comparatively simpler and less costly arrangements. The CTC utilises flame chemiluminescence measurements, and hence there is no need for an external source of illumination. Since chemiluminescence occurs in a region close to the reaction zone, the reconstructed 3D chemiluminescence field can reveal important geometrical features such as flame propagation and wrinkling, flame orientation, vortex shedding and breakdown, jet precession and recirculation and local quenching. In principle, any kind of emission measurement,

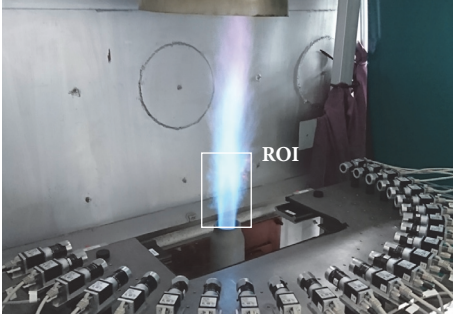


FIGURE 1: The setup used for the CTC, constituting 24 cameras with filters (Schott BG40), arranged equiangularly within a 172.5° region, around the burner operated with natural gas, at the GWI (the white box shows the imaging region of interest ROI).

such as emissions from heated soot particles in the flame, as demonstrated by Hossain et al. [5] can be used with the CTC. Our focus on gaseous flames so far demonstrates the capability of CTC and prepares the technique for application to coal-fired combustion where emissions from heated coal particles will be used for volumetric flame reconstructions [6]. The CTC was first developed to reconstruct the instantaneous chemiluminescence field of gaseous flames by Floyd [7], and was proven to work using commodity cameras. It was initially tested using several phantoms (exactly known fields which are compared to their reconstruction for quantified analysis of the reconstruction quality). Some flame experiments, where either one camera was rotated around a steady flame [8] or mirrors captured 10 flame chemiluminescence images for the reconstructions [3], were also demonstrated.

We have built a new setup that constitutes 24 low-cost (< €600) and light-weight (< 90 g) monochrome CCD cameras, for the application of CTC to a series of different flames. It was first applied to quasi-steady [9] and unsteady Bunsen flames [10], and a turbulent swirl flame [4] within our institute. To demonstrate the versatility of the technique at its current stage, we took the setup to the Gas- und Wärme-Institute (GWI) in Essen to reconstruct the chemiluminescence field of flames from a high-power industrial burner that was made optically accessible. Within three days, the setup was completed around the burner and flame reconstructions were achieved, revealing information about the flame shape, which are presented in this paper, for the first time.

2. The CTC Technique

The CTC directly calculates the instantaneous 3D chemiluminescence field using multiple measurements (in the form of camera images) that are obtained from different angles θ around the object, as depicted in Figure 1. The total number of pixels (or projections) N_{pix} in one camera image which is obtained at the same angle θ , forms a view q , with a total number of N_{cams} views. The spectral density detected on the camera pixel corresponds to the sum (line-of-sight projection) of the light emitted along the light ray path

TABLE 1: The burner flow conditions: ϕ is the equivalence ratio, \dot{V}_{CH_4} and \dot{V}_{air} are the methane and air volume flow rates of the combustion gases, respectively, Re is the cold flow Reynolds number based on D , t_{exp} is the camera exposure time and P is the flame thermal power.

ϕ	\dot{V}_{CH_4} (m ³ /h)	\dot{V}_{air} (m ³ /h)	Re	t_{exp} (ms)	P (kW)
0.79	8	100	~ 40000	0.1	83
0.79	10	127	~ 50000	0.1	105

through the probe volume. This is based on the fundamental radiative transfer equation (RTE), which relates the change in radiation intensity along a ray path to local absorption and volume emission [11, 12]. In the CTC, the RTE is simplified by neglecting scattering and re-absorption. The projection measurement I_{qp} is approximated as a finite sum going through the 3D field, that is, discretised into a total number of N_{vox} voxels, via (1). In (1) $w_{qp\nu}$ represents the contribution of each voxel ν to the line of sight projection p of view q and $Q_\nu(x, y, z)$ is the scalar field to be reconstructed.

$$I_{qp} = \sum_{\nu=1}^{N_{vox}} w_{qp\nu} Q_\nu \quad (1)$$

The CTC algorithm that uses the projection measurements is based on the iterative Algebraic Reconstruction Technique (ART) [13]. The camera optics are modelled via simple ray-tracing representation, and non-parallel rays were implemented to account for perspective effects. This means that the rays fan out as a function of focal length and cover a large volume focused in the focal plane as a function of focal depth, thus requiring a direct reconstruction in 3D, as opposed to stacked reconstructions in 2D. The projection rays also consider the blur-effect, to account for limited depth of field. For the reconstruction process, the measured projections I_{qp} are compared to equivalent projections that are taken through the current iteration's estimate of the field Q_ν^h , where h denotes the current iteration step. The reconstruction is assumed to be converged once the absolute difference of the sum of the field vector, from one iteration to the next, is below the threshold $\Delta_c \times Q_\nu^h$. The value of Δ_c is chosen by the user and is typically in the range of 10^{-3} and 10^{-6} . In-depth detail on the algorithm and initial extensive parametric phantom studies can be found in [3, 7, 8].

3. The Experimental Setup

A standard industrial burner was used, which is commonly utilised for heating purposes in thermal processes. The burner is modular and can be equipped with different nozzle configurations. The ceramic nozzle head used here had an exit diameter of $D = 65$ mm and length $L = 300$ mm. The burner was not encased and the premixed combustion gases constituted natural gas (90 mol% methane) and air at atmospheric conditions. Premixing was achieved inside the ceramic nozzle. The chemiluminescence images were obtained for the flame operating with a thermal power of 83 kW and 105 kW. The complete test conditions are given in Table 1.

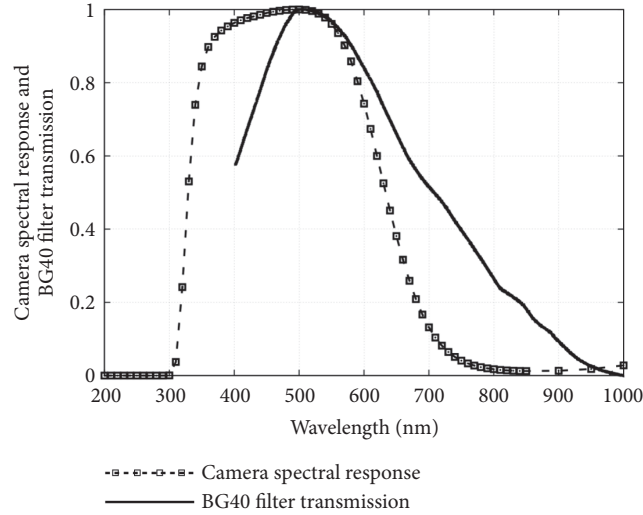


FIGURE 2: Spectral response of the cameras and the transmission curve of the Schott BG40 filter used for water emission suppression.

As shown in Figure 1, a total of $N_{cams} = 24$ CCD cameras (Basler acA645-100gm containing a 0.5" Sony ICX414 monochrome sensor, 659 by 494 pixels of size $9.9 \times 9.9 \mu\text{m}$) were mounted on one plate, with a constant angular separation of $\theta = 7.5^\circ$ in one plane within a total fan angle of 172.5° around the burner. Preset holes at a fixed distance from the burner and the aforementioned angular separation were used for the camera mounts. A back-illuminated pinhole, which was mounted on a rotation stage that measures the angle to within $\pm 0.5^\circ$ accuracy, was placed at the burner location. Camera alignment was achieved by first lining the point light onto camera 1 and consecutively rotating it by 7.5° to point to the rest of the cameras. Each time the relevant camera was adjusted to ensure that the image of the light point falls on the centre pixel of the camera image. The adequacy of this camera alignment method was checked in our previous work [4].

The spectral response of the cameras, at $> 60\%$, is between about 400 nm and 680 nm. Kowa C-mount lenses (focal length 12 mm) were used. Each camera was fitted with an optical filter (Schott BG40) to eliminate the detection of thermally heated water which emits lights in the near infra-red and infra-red range. The images were taken by capturing all other emitted signals from the excited species, the prominent ones being CH^* (around 430 nm) and C_2^* (around 515 nm) and broadband CO_2^* . Figure 2 illustrates the spectral response of the cameras and the transmission curve of the filters used. One trigger signal was sent to all cameras and the image readout was done simultaneously through two Ethernet switches (Gigabit smart TL-SG2424P) that were connected to the control and evaluation computer. The tomography setup used here was the same as the one used recently to reconstruct a turbulent swirl flame [4].

The interest was in lowering the camera exposure time t_{exp} as much as possible to minimise motion blur, so that finer flame structures could be resolved. The aperture opening was set to its largest opening size, $f/1.4$, and an exposure time

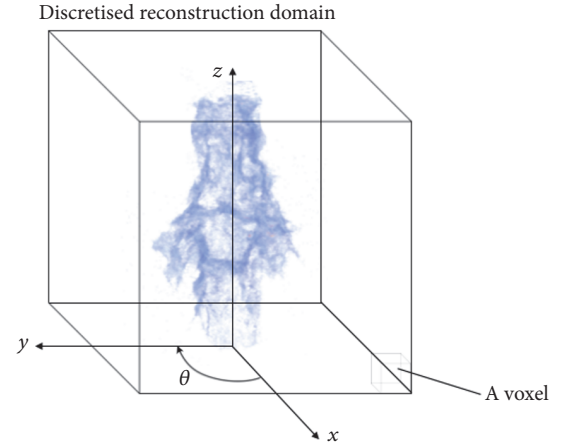


FIGURE 3: Reconstruction domain around the flame, discretized into voxels.

of $t_{exp} = 0.1$ ms was used. Images of the background signal (the scene without the flame) were obtained by each camera directly after the flame tests. Background correction was applied by subtracting the pixel intensities of the background images from the flame images.

4. 3D Instantaneous Reconstructions of the Flame

All 24 views of the flame were used for the reconstructions. The flame images had a pixel resolution of 0.8 mm and contained 164 by 168 pixels in the horizontal and vertical directions respectively (providing a total of 27,552 projection measurements per view). The 3D reconstruction domain constituted 164 by 164 by 168 voxels in the xyz directions, the coordinates are illustrated in Figure 3. Examples of the flame images obtained at different angles for one instantaneous time are shown in Figure 4.

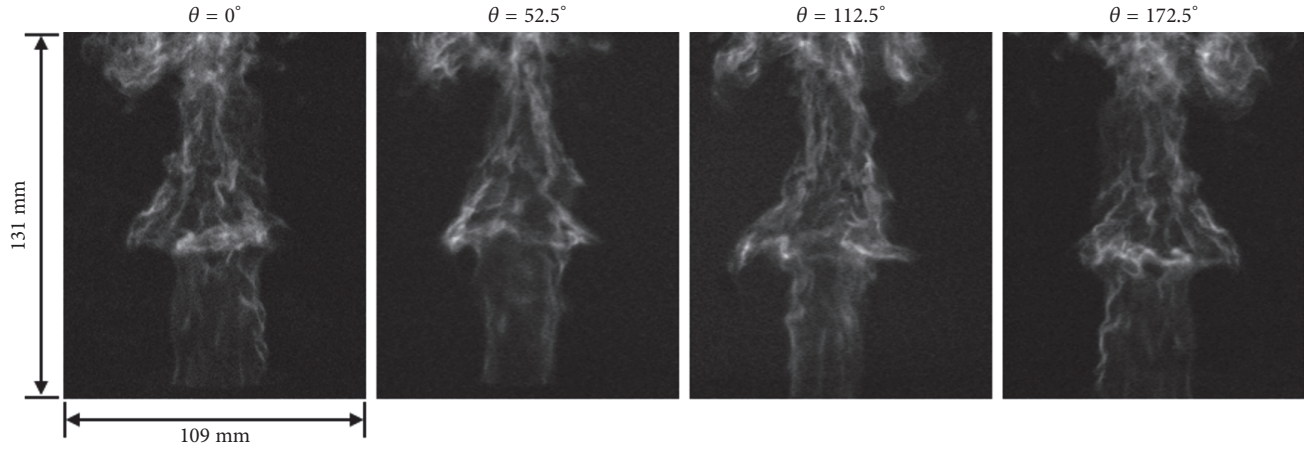


FIGURE 4: Examples of the flame projections from different angles, for the 83 kW flame.

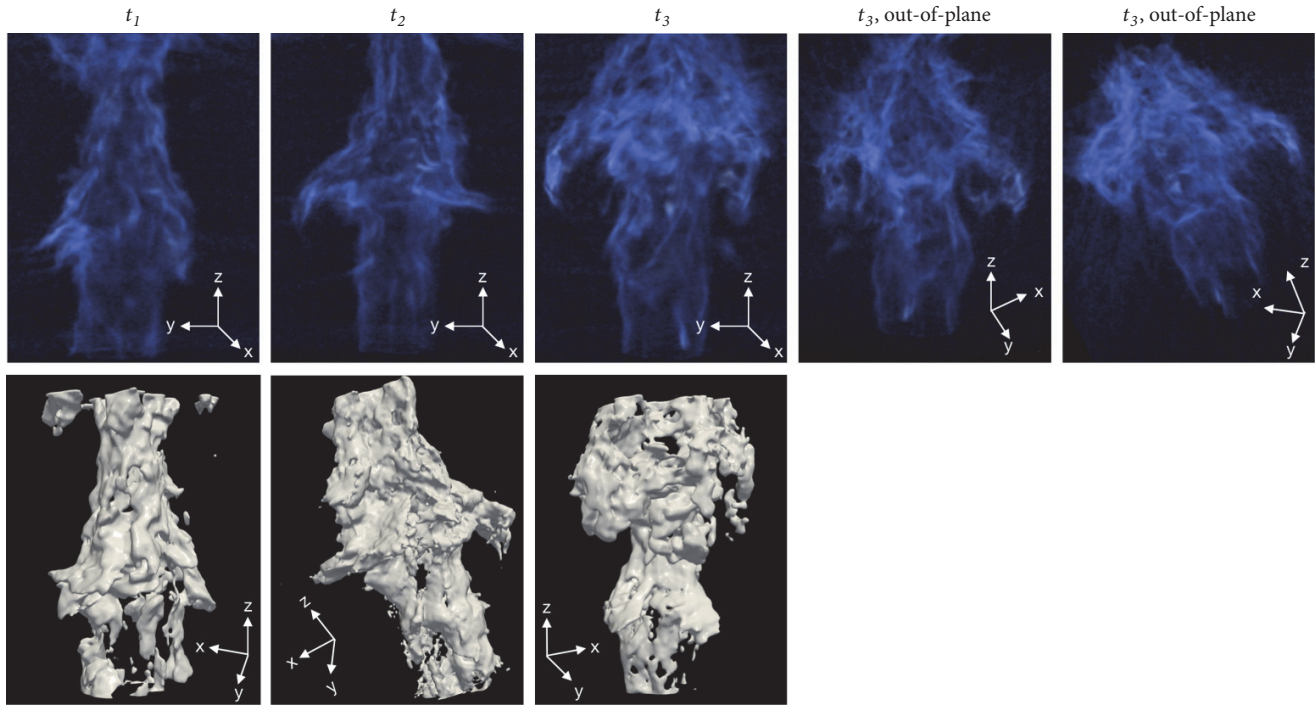


FIGURE 5: Volume-rendered views (top) and iso-surfaces (bottom) of the reconstructed 83 kW flame at different randomly chosen instances in time, shown from random angles that do not correspond to any view angle.

Volume-rendered views and iso-surfaces of the reconstructed 83 kW flame, for different instances in time, particularly chosen to reveal the shedding of large-scale structures in the downstream direction, are shown in Figure 5. For one case, t_3 , two further inclined views at two further random angles are illustrated. It is important to observe the field from angles that do not coincide with any of the original view angles, since these angles will have a bias towards better reconstruction quality.

Examples of the horizontal slices at different heights above the burner z , and vertical slices from the reconstructed fields are shown in Figures 6 and 7, respectively. Data is presented for both instantaneous and time-averaged flames

(averages are calculated from 100 instantaneous snapshots). It is a particularly stringent test to check the horizontal slices from the reconstructed field since information was only provided to the algorithm from the vertical directions. The slices in Figure 6 demonstrate a good reconstruction quality that does not exhibit the artefacts which are typically seen in low-quality CTC results, such as parallel lines that cut through the domain. The instantaneous slices show that from very close to the burner exit the flame is highly wrinkled. The averaged flame reconstructions show the expected smooth shape but since the flames were very unsteady (as observed during the experiments), more than 100 instantaneous snapshots are presumably needed to produce a fully symmetric field. There

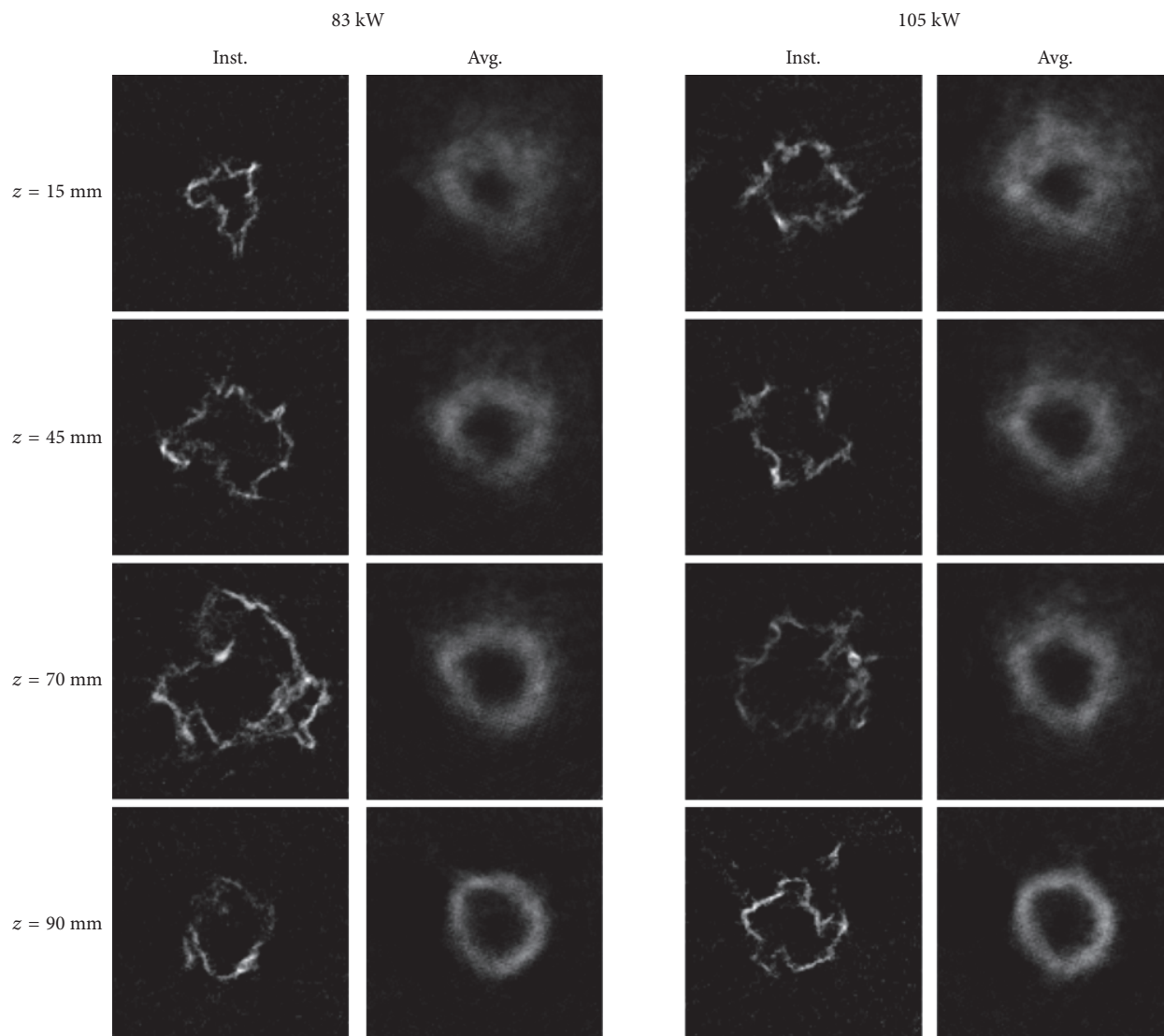


FIGURE 6: Horizontal slices from the reconstructed instantaneous and time-averaged (from 100 snapshots) flame images, at different heights above the burner z .

does not appear to be a striking difference between the two different powered flames.

5. Conclusions

The chemiluminescence field of highly turbulent and unsteady industrial burner flames at the GWI were reconstructed for the first time using the full CTC technique that comprises an experimental setup with 24 low-cost CCD cameras (for capturing the flame chemiluminescence), and a tomographic algorithm that includes non-parallel perspective-corrected projections. The wrinkled flame shape in the instantaneous reconstructions and the smooth field in the time-averaged cases were revealed by looking at the volume-rendered views and different horizontal and vertical slices from the reconstructed fields. All the results showed a good reconstruction quality that can be achieved from

the low-cost and versatile CTC technique, proving it to be a practical flame imaging method. Reconstructions from different instances in time showed that the flames shed large-scale structures in the downstream direction.

Data Availability

All the data, including raw flame images and reconstructed fields, that were used for the production of the manuscript is available within specially allocated hard drives in our department and can be accessed without restriction.

Disclosure

This work was presented at the 3rd General Meeting and Workshop on SECs in Industry COST Action 1404 of the

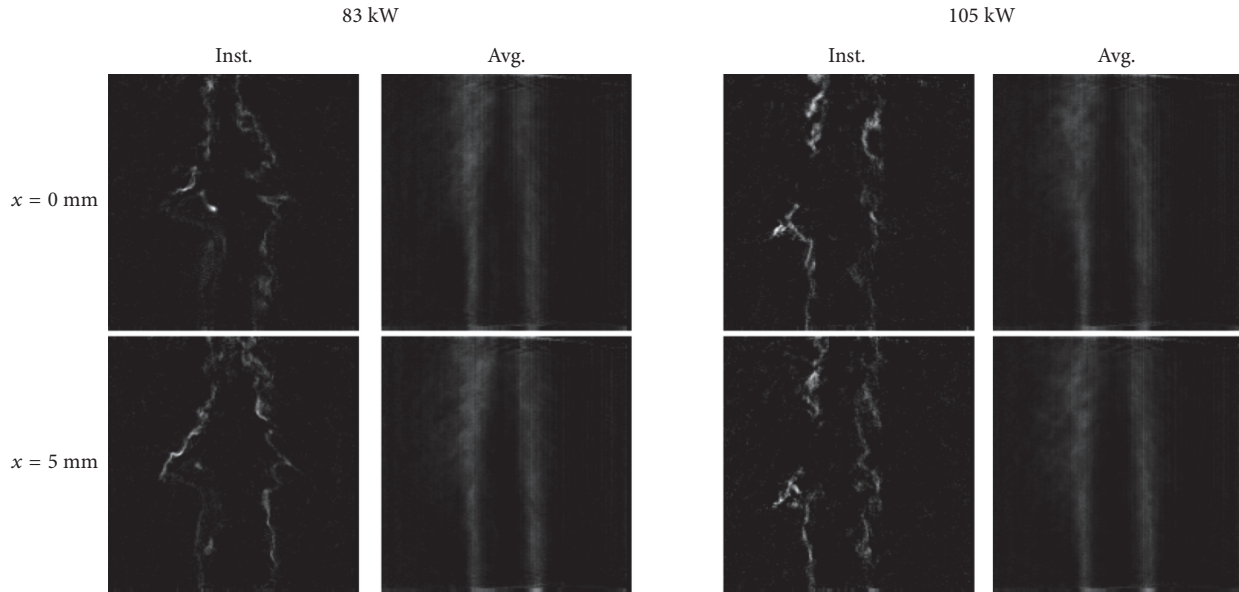


FIGURE 7: Vertical slices from the reconstructed instantaneous and time-averaged (from 100 snapshots) flame images, at the burner centreline and one neighbouring plane.

European Cooperation in Science and Technology, Prague (Oct. 2017).

Conflicts of Interest

The authors declare that they have no conflicts of interest.

Acknowledgments

The authors are grateful for the funding from the Ministerium für Innovation, Wissenschaft und Forschung des Landes Nordrhein-Westfalen, and the support by the Open Access Publication Fund of the University of Duisburg-Essen.

References

- [1] B. Peterson, E. Baum, B. Böhm, V. Sick, and A. Dreizler, "High-speed PIV and LIF imaging of temperature stratification in an internal combustion engine," *Proceedings of the Combustion Institute*, vol. 34, no. 2, pp. 3653–3660, 2013.
- [2] K. Y. Cho, A. Satija, T. L. Pourpoint, S. F. Son, and R. P. Lucht, "High-repetition-rate three-dimensional OH imaging using scanned planar laser-induced fluorescence system for multiphase combustion," *Applied Optics*, vol. 53, no. 3, p. 316, 2014.
- [3] J. Floyd, P. Geipel, and A. M. Kempf, "Computed Tomography of Chemiluminescence (CTC): instantaneous 3D measurements and Phantom studies of a turbulent opposed jet flame," *Combustion and Flame*, vol. 158, no. 2, pp. 376–391, 2011.
- [4] K. Mohri, S. Göers, J. Schöler et al., "Instantaneous 3D imaging of highly turbulent flames using computed tomography of chemiluminescence," *Applied Optics*, vol. 56, no. 26, pp. 7385–7395, 2017.
- [5] M. M. Hossain, G. Lu, D. Sun, and Y. Yan, "Three-dimensional reconstruction of flame temperature and emissivity distribution using optical tomographic and two-colour pyrometric techniques," *Measurement Science and Technology*, vol. 24, no. 7, Article ID 074010, 2013.
- [6] Y. Yan, T. Qiu, G. Lu, M. M. Hossain, G. Gilibert, and S. Liu, "Recent advances in flame tomography," *Chinese Journal of Chemical Engineering*, vol. 20, no. 2, pp. 389–399, 2012.
- [7] Floyd, J., *Computed tomography of chemiluminescence: a 3D time resolved sensor for turbulent combustion*. 2009, Imperial College London.
- [8] J. Floyd and A. M. Kempf, "Computed Tomography of Chemiluminescence (CTC): high resolution and instantaneous 3-D measurements of a matrix burner," *Proceedings of the Combustion Institute*, vol. 33, no. 1, pp. 751–758, 2011.
- [9] K. Mohri and A. Kempf, "Computed tomography of chemiluminescence for 3D reconstructions of quasi-steady premixed flames," in *in Combustion Institute (British section) meeting, talk and poster*, London, Imperial College, 2014.
- [10] K. Mohri and A. Kempf, "Computed tomography of chemiluminescence in asymmetric unsteady premixed flames," in *27th Deutscher Flammentag*, VDI-Berichte Nr. 2267, Clausthal-Zellerfeld, 2015.
- [11] J. R. Howell, R. Siegel, and M. P. Mengüç, *Thermal radiation heat transfer*, CRC Press, Taylor & Francis Group, Boca Raton, Florida, USA, 5 edition, 2010.
- [12] K. J. Daun, S. J. Grauer, and P. J. Hadwin, "Chemical species tomography of turbulent flows: Discrete ill-posed and rank deficient problems and the use of prior information," *Journal of Quantitative Spectroscopy & Radiative Transfer*, vol. 172, pp. 58–74, 2016.
- [13] R. Gordon, "A tutorial on art (algebraic reconstruction techniques)," *IEEE Transactions on Nuclear Science*, vol. 21, no. 3, pp. 78–93, 1974.

Research Article

Simulation of Coal and Biomass Cofiring with Different Particle Density and Diameter in Bubbling Fluidized Bed under O_2/CO_2 Atmospheres

Chao Chen ¹, Xuan Wu,¹ and Lingling Zhao ^{1,2}

¹School of Energy & Environment, Southeast University, Nanjing, Jiangsu 210096, China

²Key Laboratory of Energy Thermal Conversion and Control of Ministry of Education, Nanjing, Jiangsu 210096, China

Correspondence should be addressed to Lingling Zhao; zhao_lingling@seu.edu.cn

Received 3 May 2018; Revised 26 July 2018; Accepted 18 August 2018; Published 12 September 2018

Academic Editor: Hiroaki Watanabe

Copyright © 2018 Chao Chen et al. This is an open access article distributed under the Creative Commons Attribution License, which permits unrestricted use, distribution, and reproduction in any medium, provided the original work is properly cited.

A 2D dynamic model for a bubbling fluidized bed (BFB) combustor has been developed for simulating the coal and biomass cofiring process under 21% O_2 /79% CO_2 atmosphere in a 6 kWth bubbling fluidized bed, coupled with the Euler-Euler two-phase flow model. The kinetic theory of binary granular mixtures is employed for the solid phase in order to map the effect of particle size and density. The distribution of temperature, volume fraction, velocity, gas species concentration, and reaction rates are studied with numerical calculations. The simulated temperature distribution along the height of the combustor and outlet gas concentrations show good agreement with experimental data, validating the accuracy and reliability of the developed cofiring simulation model. As indicated in the results, there are two high temperature zones in the combustor, which separately exist at the fuel inlet and dilute phase. The reaction rates are related to the species concentration and temperature. The higher concentration and temperature lead to the larger reaction rates. It can be seen that all of the homogeneous reaction rates are larger at the fuel inlet region because of rich O_2 and volatiles. High mass fraction of volatile gas is found at the fuel inlet, and the main reburning gas at the dilute phase is CH_4 . The mass fraction distribution of CO is related to the volume fraction of fuel which is due to the fact that the source of CO is not only from the devolatilization but also from the gasification. On the basis of this theoretical study, a better understanding of flow and combustion characteristics in biomass and coal cofiring under oxy-fuel atmospheres could be achieved.

1. Introduction

Biomass is a carbon-neutral fuel with a large reserve available, producing no net CO_2 emissions in its life cycle, and can reduce net CO_2 emissions effectively in coal-based power plants [1]. Biomass cofiring with coal provides an alternative way to utilize biomass fuel effectively due to its many advantages such as low risk, good emission properties, and better fuel economy [2, 3]. Fluidized bed (FB) combustion technology is suitable for biomass and coal cocombustion due to its high combustion efficiency for various types of fuel and better emission characteristics [4–6]. What is more, in comparison with pulverized-fuel (PF) boilers, fluidized bed combustors could be designed with a relatively small investment for conversion from coal combustion to biomass and coal cofiring.

Oxy-fuel combustion technology is a type of carbon-capture technology first proposed by Abraham et al. in 1982 [7]. Several experimental investigations demonstrated the potential and economic value of its application in fluidized bed combustors [8–10]. In recent years, researchers have paid more attention to biomass and coal cofiring in oxy-fuel fluidized bed combustors [11]. Tan et al. [12] conducted a series of tests on combustion and emission characteristics of wood cofiring with coal in a pilot-scale oxy-fuel circulating fluidized bed (CFB) combustor and concluded that it is feasible for achieving negative emissions of CO_2 . Duan et al. [13] studied NO emission from biomass and coal cofiring in a 10 kWth CFB under oxy-fuel conditions. It was found that the emission of NO in an O_2/CO_2 atmosphere is lower than that in an air atmosphere. Experiments were carried out by Kumar and Singh [14, 15] to investigate the temperature profile,

gas emission, particle size distribution, and combustion efficiency of four kinds of biomass cofiring with coal under an oxy-fuel atmosphere in a 20 kWth CFB.

Computational fluid dynamics (CFD) has been widely used to study the combustion and flow characteristics of biomass cofiring with coal [16–21]. Gungor [22] simulated the biomass and coal cofiring in CFB using a developed model which investigated the effect of biomass fraction on CO, NO_x, and SO₂ emissions. Zhang et al. [23] simulated the combustion of low density biomass (oat hulls) cofiring with coal in a fluidized bed combustor by using an Euler-Lagrange model and found that the mass fraction of biomass can affect the peak temperature of the furnace, while the adjustment of the secondary air can strongly affect the combustion of oat hulls. However, there have been only a few studies in which biomass cofiring in FB was simulated under an oxy-fuel atmosphere. Bhuiyan et al. [24, 25] simulated biomass cofiring in PF under an O₂/CO₂ atmosphere and studied the effects of oxygen concentration and biomass ratio on combustion characteristics.

There are two main approaches to describe the hydrodynamic behavior of particles in the fluidized bed: Lagrange (discrete element) and Eulerian (continuum). The Lagrange approach tracks every individual particle in the random flow field by solving its motion equation. The external force directly acting on each particle is taken into account. On the other hand, the Eulerian approach describes the carrier and the dispersed phase with a set of continuum equations representing conservation of mass, momentum, and energy of either phase within a fixed element volume. In the simulation of a dense fluidized bed, the discrete particles are approximated as continuous phase for describing the gas-particle and particle-particle interaction, which is based on the kinetic theory of granular flow (KTGF). The KTGF is developed from the kinetic theory of dense gases [26]. It is based on the Boltzmann equation, which represents the relative disordered motion of particles according to the collision and fraction through the granular temperature (θ). Goldschmidt et al. [27] demonstrated that simulations using KTGF agree well with the elastic particles model of a fluidized bed. Nevertheless, the original KTGF [28] cannot model a mixture with different size/density particles, due to the assumption that all particles have equal granular temperature [29, 30]. Hence, Lu et al. [30, 31] extended the KTGF model to a binary granular mixture with different granular temperatures by means of the Maxwell distribution. Wang et al. [32] simulated combustion and desulfurization processes in CFB with various particle size/density (coal/limestone) using the KTGF model with different granular temperatures. It is obvious that the flow and combustion characteristics of fuel are greatly affected by the particle size and density [33]. The assumption of average density and particle size limits the accuracy of simulations [21, 32]. Therefore, it is necessary to establish a model of coal and biomass cofiring in FB with different particle size and density.

In this study, the combustion and flow characteristics of biomass cofiring with coal in a 6 kWth oxy-fuel bubbling fluidized bed combustor have been investigated using CFD. The constitutive properties of the dispersed solid phases

are predicted with the kinetic theory of binary granular mixtures. The unsteady processes of gas-solid two-phase flow, heat, and mass transfer incorporating the devolatilization, heterogeneous, and homogeneous reactions are considered in this simulation.

2. Computational Modelling

Based on an Euler-Euler approach, a complicated model including gas-solid multiphase flow, interphase heat and mass transfer, devolatilization of coal and biomass, and homogeneous and heterogeneous reactions has been established. In order to ensure the good convergence and acceptable computational time, the established model was simplified; the main assumptions adopted in this study are listed as follows. (1) The mesh model is assumed as 2-dimensional with the furnace depth of 0.05 m. The widths of dilute and dense zones in the 2D case are determined based on the corresponding cross-section area in the 3D furnace. (2) The solid phase is composed of coal and biomass particles with different density and diameter. Both of them are assumed as inelastic spheres. (3) The gas is considered to be incompressible and ideal and there is no slippage near the wall. (4) The intensity of granular collision is independent with bed temperature. (5) The radiant heat transfer in the furnace is ignored, but the wall radiation is taken into account in the overall wall heat transfer coefficient. For good computational convergence, the heat transfer between coal and biomass particles is neglected. (6) Energy transfer induced by the effect of pressure, viscous dissipation, and compositional diffusion is ignored. (7) The reactions of denitration and desulfurization processes are neglected in the combustion submodel due to the less influence on temperature field.

2.1. Hydrodynamic Model

2.1.1. Gas Phase. The governing equations for gas phase are shown as (1)–(3), where the subscripts s and g represent solid phase and gas phase, respectively. α , ρ , \vec{u} , p , H , and T are the volume fraction, the density, the instantaneous velocity, the pressure, the enthalpy, and the temperature, respectively. S_g^m is the mass source term for gas phase contributed by chemical reactions. $\bar{\tau}$ is the stress-strain tensor. $\beta_{s,g}$ is the gas-solid drag coefficient which is defined as Gidaspow model [47]. $\vec{m}_{s,g}$ means the mass transfer from solid phase to gas phase. \vec{J}_e in (3) is the energy source term, including the heat generation per unit volume and the heat exchange caused by convection between gas and solid. λ is the coefficient of heat transfer between gas and solid calculated by Gunn's model [48]. The species conservation equation is expressed by (4), where subscript $i=1-8$ representing the 8 kinds of species (H₂O, H₂, CO, CO₂, CH₄, C₂H₆, tar, and O₂) in the gas phase. $Y_{g,i}$ is the mass fraction for gas i , \vec{J}_i is the diffusion flux caused by concentration gradient of species i , and R_i is the substance reaction rates during chemical reactions.

$$\frac{\partial}{\partial t} (\alpha_g \rho_g) + \nabla \cdot (\alpha_g \rho_g \vec{u}_g) = S_g^m \quad (1)$$

$$\begin{aligned} & \frac{\partial}{\partial t} (\alpha_g \rho_g \vec{u}_g) + \nabla \cdot (\alpha_g \rho_g \vec{u}_g \vec{u}_g) \\ &= -\alpha_g \nabla p + \alpha_g \nabla \cdot \vec{\tau}_g + \alpha_g \rho_g g + \sum_{i=1} \beta_{s_i g} (\vec{u}_{s_i} - \vec{u}_g) \quad (2) \\ &+ \sum_{i=1} \dot{m}_{s_i g} \vec{u}_{s_i} \end{aligned}$$

$$\frac{\partial}{\partial t} (\alpha_g \rho_g H_g) + \nabla \cdot (\alpha_g \rho_g \vec{u}_g H_g) = \nabla \cdot (\lambda_g \nabla T_g) + \vec{J}_e \quad (3)$$

$$\frac{\partial}{\partial t} (\rho \alpha_g Y_{g,i}) + \nabla \cdot (\rho \alpha_g \vec{u}_g Y_{g,i}) = -\nabla \cdot \vec{J}_i + R_i \quad (4)$$

2.1.2. Particle Phase. The continuity, momentum, and energy equations of solid phase are shown in (5)-(7). The same characters share the same definitions with the gas phase. $\beta_{s_{ij}}$ is the drag coefficient between different particle phases. Based on KTGF for binary granular mixture model, each particle phase has different size, density, and granular temperature. The kinetic energy equation for particle phases is shown in (8), where θ_i is the granular temperature for each particle phase. k_{θ_i} , γ_{θ_i} , and ϕ_{sg} are the diffusion coefficient for particle phase, the dissipation rate caused by particle inelastic collision, and kinetic energy exchange between gas and particles, respectively. The detailed derivation for KTGF of binary granular mixture model is given in [30, 32].

$$\frac{\partial}{\partial t} (\alpha_{s_i} \rho_{s_i}) + \nabla \cdot (\alpha_{s_i} \rho_{s_i} \vec{u}_{s_i}) = S_{s_i}^m \quad (5)$$

$$\begin{aligned} & \frac{\partial}{\partial t} (\alpha_{s_i} \rho_{s_i} \vec{u}_{s_i}) + \nabla \cdot (\alpha_{s_i} \rho_{s_i} \vec{u}_{s_i} \vec{u}_{s_i}) \\ &= -\alpha_{s_i} \nabla p + \alpha_{s_i} \nabla \cdot \vec{\tau}_{s_i} + \alpha_{s_i} \rho_{s_i} g - \beta_{s_i g} (\vec{u}_{s_i} - \vec{u}_g) \quad (6) \\ &+ \sum_{i=1, i \neq j} \beta_{s_{ij}} (\vec{u}_{s_i} - \vec{u}_{s_j}) - \sum_{i=1} \dot{m}_{s_i g} \vec{u}_{s_i} \end{aligned}$$

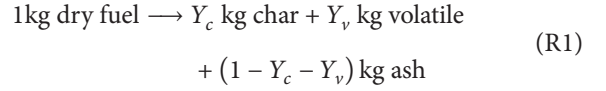
$$\frac{\partial}{\partial t} (\alpha_{s_i} \rho_{s_i} H_{s_i}) + \nabla \cdot (\alpha_{s_i} \rho_{s_i} \vec{u}_{s_i} H_{s_i}) = \nabla \cdot (\lambda_{s_i} \nabla T_{s_i}) + \vec{J}_e \quad (7)$$

$$\begin{aligned} & \frac{3}{2} \left[\frac{\partial}{\partial t} (\alpha_{s_i} \rho_{s_i} \theta_i) + \nabla \cdot (\alpha_{s_i} \rho_{s_i} \vec{u}_{s_i} \theta_i) \right] \\ &= \vec{\tau}_{s_i} : \nabla \vec{u}_i + \nabla \cdot (k_{\theta_i} \nabla \theta_i) - \gamma_{\theta_i} + \phi_{sg} \quad (8) \end{aligned}$$

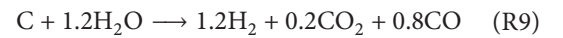
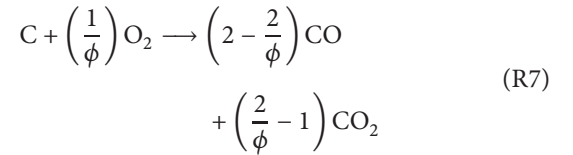
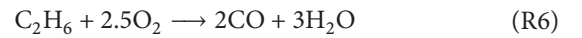
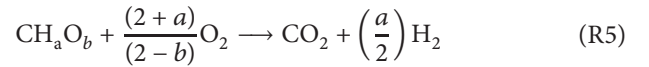
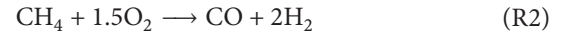
2.2. Chemical Reaction Model. The cofiring process of coal and biomass is defined as 3 parts: water evaporation and devolatilization, homogeneous reactions (volatile combustion), and heterogeneous reactions (char oxidation and gasification). All of the reaction rates are shown in Table 1.

2.2.1. Coal and Biomass Devolatilization Model. Five volatile products are considered during coal and biomass devolatilization: CH_4 , H_2 , CO , tar, and C_2H_6 [40, 49, 50]. The devolatilization of coal and biomass is expressed by reaction (R1). Y_c and Y_v are the mass fractions of char and volatile,

respectively. The amount of volatile products is calculated by the correlation used in [40, 51].



2.2.2. Homogeneous and Heterogeneous Reactions. Reactions (R2)-(R6) are the homogeneous reactions. The combustion rates of volatiles follow Arrhenius's law. The char oxidation and gasification reactions are shown in (R7)-(R9), where ϕ is mechanical factor determining the balance of CO and CO_2 production.



2.3. Numerical Method and Boundary Conditions. A 2D mesh was established to simulate the furnace of the bubbling fluidized bed which is shown in Figure 1. As shown in the figure, the fuel inlet, secondary air inlet, and the fuel gas outlet are at the heights of 0.18 m, 0.65 m, and 1.5 m, respectively. The grids at the fuel inlet and the secondary air inlet were refined. The total number of grids is 7751. Some main parameters used in the simulation are shown in Table 2. The selection of restitution coefficients is referred from [32, 52, 53]. The proximate analysis and ultimate analysis of coal and biomass (woodchips) are shown in Table 3.

Fluent software was used in this study, and unsteady equation was employed in the solution. Pressure-temperature coupling employed SIMPLE algorithm, and gradient interpolation employed Green-Gauss algorithm based on elementary volume. Velocity of the solid phase was assumed to be 0 at the initial time, and velocity of the gas phase was the same as the inlet velocity of primary air. Temperature in the furnace was uniform. Mirror coefficient of solid particle was considered to be 0.5 and thickness of the wall was 0.2 m. The chemical reaction rates coupled with the model were determined by user-defined functions. No slip boundary condition was applied for gas phase and Johnson-Jackson model [54] was adopted for particle phases at near wall region.

TABLE 1: Rates for the homogeneous and heterogeneous reactions.

	Reaction rate $r/\text{kmol.m}^{-3}\text{s}^{-1}$	Coal and biomass devolatilization	Reaction coefficient k_c
(R1)	$r_1 = \alpha_{s_i} k_1 C_{r_{nuc}}$ [34, 35]	$k_1 = \begin{cases} 4.136 \times 10^4 (\text{s}^{-1}) \exp(-0.73 \times 10^8/RT) & \text{coal} \\ 9.2 \times 10^8 (\text{s}^{-1}) \exp(-1.3576 \times 10^8/RT) & \text{biomass} \end{cases}$	
Homogeneous reactions			
(R2)	$r_2 = \alpha_g k_2 C_{O_2}^{0.8} C_{CH_4}^{0.7}$ [36]	$k_2 = 5.0122 \times 10^{11} (\text{m}^3 \text{kmol}^{-1} \text{s}^{-1}) \exp(-2.0085 \times 10^8/RT)$	
(R3)	$r_3 = \alpha_g k_3 C_{CO} C_{O_2}^{0.5} C_{H_2O}^{0.5}$ [37]	$k_3 = 1.3 \times 10^{11} (\text{m}^3 \text{kmol}^{-1} \text{s}^{-1}) \exp(-1.255 \times 10^8/RT)$	
(R4)	$r_4 = \alpha_g k_4 C_{O_2} C_{H_2}$ [38]	$k_4 = 1.0 \times 10^8 (\text{m}^3 \text{kmol}^{-1} \text{s}^{-1}) \exp(-0.083 \times 10^8/RT)$	
(R5)	$r_5 = \alpha_g k_5 C_{O_2} C_{tar}$ [39]	$k_5 = 3.8 \times 10^7 (\text{m}^3 \text{kmol}^{-1} \text{s}^{-1}) \exp(-0.555 \times 10^8/RT)$	
(R6)	$r_6 = \alpha_g k_6 C_{C_2H_6} C_{O_2}$ [40]	$k_6 = 1.068 \times 10^5 (\text{m}^3 \text{kmol}^{-1} \text{s}^{-1}) T^{0.5} \exp(-1.674 \times 10^8/RT)$	
Heterogeneous reactions			
(R7)	$r_7 = (6\alpha_{s_i} \rho_{s_i} Y_{char}/d_s \rho_c) \bullet k_c C_{O_2} k_7$ $k_c = (RT/w_c)/(1/k_d + 1/k_7)$ [40–42]	$k_7 = 8910 (\text{kgm}^3 \text{s}^{-1} \text{kPa}^{-1}) \exp(-1.4974 \times 10^8/RT)$, $k_d = \phi Sh D_g w_c / d_s RT_g$, $Sh = 2\varepsilon + 0.69(Re/\varepsilon)^{1/2} Sc^{1/3}$, $Re = ud \rho_g / \mu_g$ $Sc = \mu_g / \rho_g D_g$, $D_g = D_{g_0} \bullet (T/T_0)^{1.75} (p/p_0)$, $D_{g_0} = 3.13 \times 10^{-4} (\text{m}^2 \text{s}^{-1})$, $T_0 = 1500(\text{K})$, $p_0 = 101325(\text{Pa})$	
(R8)	$r_8 = k_8 C_{CO_2} / (1 + K_{k_{O_2}}^{k_{O_2}} C_{CO_2} + K_{k_{CO}}^{k_{CO}} C_{CO})$ [43–45]	$k_8 = 4.89 \times 10^{10} (\text{m}^3 \text{kmol}^{-1} \text{s}^{-1}) \exp(-2.68 \times 10^8/RT) (\rho_s Y_c / MW_s) (1 - X)$, $K_{k_{O_2}}^{k_{O_2}} = 66 (\text{m}^3 \text{kmol}^{-1})$, $X = 0.35$, $K_{k_{CO}}^{k_{CO}} = 1.20 \times 10^2 (\text{m}^3 \text{kmol}^{-1}) \exp(-2.55 \times 10^7/RT)$	
(R9)	$r_9 = k_9 C_{H_2O} / (1 + K_{k_{H_2O}}^{k_{H_2O}} C_{H_2O} + K_{k_{H_2}}^{k_{H_2}} C_{H_2} + K_{k_{CO}}^{k_{CO}} C_{CO})$ [43, 46]	$k_9 = 2.39 \times 10^5 (\text{m}^3 \text{kmol}^{-1} \text{s}^{-1}) \exp(-1.29 \times 10^8/RT) (\rho_s Y_c / MW_s) (1 - X)$, $K_{k_{H_2O}}^{k_{H_2O}} = 31.6 (\text{m}^3 \text{kmol}^{-1}) \exp(-3.01 \times 10^7/RT)$, $X = 0.5$, $K_{k_{H_2}}^{k_{H_2}} = 5.36 (\text{m}^3 \text{kmol}^{-1}) \exp(-5.98 \times 10^7/RT)$, $K_{k_{CO}}^{k_{CO}} = 8.25 \times 10^{-2} (\text{m}^3 \text{kmol}^{-1}) \exp(-9.61 \times 10^7/RT)$	

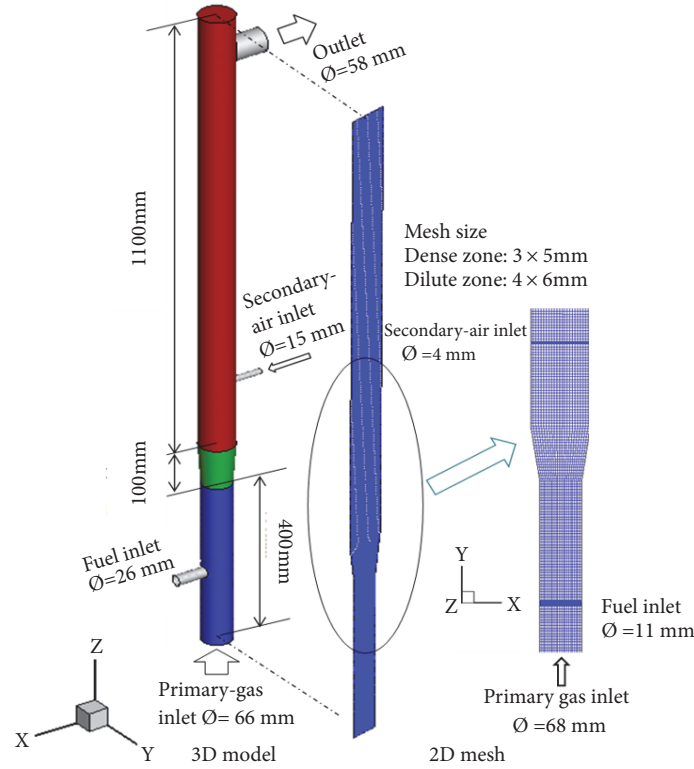


FIGURE 1: Schematics of the combustor and simulation grids.

TABLE 2: Parameters used in the simulation.

Parameters	value
Diameter of coal	0.7 mm
Diameter of biomass	0.9 mm
Density of coal	1280 kg/m ³
Density of biomass	600 kg/m ³
Density of ash	2200 kg/m ³
Fuel feed rate	0.87 kg/h
Restitution coefficient between different particles	0.95
Restitution coefficient between same particles	0.9
O ₂ /CO ₂ volume fraction	21%/79%
Excess O ₂ coefficient ^a	1.14
Primary air/ secondary air volume fraction	81%/19%
Gas phase inlet temperature	423 K
Fuel inlet temperature	300 K
Wall temperature	700 K
Velocity of primary air	0.512 m/s
Velocity of secondary air	2.04 m/s
Initial bed height	0.4 m
Initial bed temperature	1123 K

a: the oxygen/fuel ratio normalized by the actual stoichiometric oxygen/fuel ratio.

The simulation was conducted for 30 s with the time step being set as 1×10^{-4} s. For the first 0.1 s, gas-ash fluidization

TABLE 3: Fuel ultimate analysis and proximate analysis.

Fuel Name	Coal	Biomass
Ultimate analysis/wt. %		
C _{ad}	67.42	46.99
H _{ad}	4.14	5.75
O _{ad}	7.98	39.86
N _{ad}	1.04	0.39
S _{ad}	2.72	0.11
LHV MJ/kg	26.60	17.086
Proximate analysis/wt. %		
FC _{ad}	48.30	17.59
V _{ad}	35.00	75.51
A _{ad}	9.9	3.34
M _{ad}	6.8	3.36

was simulated at temperature of 1123 K without fuel feeding, and then coal and biomass were continuously fed into the furnace.

3. Results and Discussion

3.1. Validation. In order to get reliable statistics of combustion characteristics in the fluidized bed, the volume fractions of three gas species (CO₂, O₂, and H₂O) at gas outlet are monitored. The results are shown in Figure 2. It can be seen that the average volume fractions of CO₂ and H₂O at the

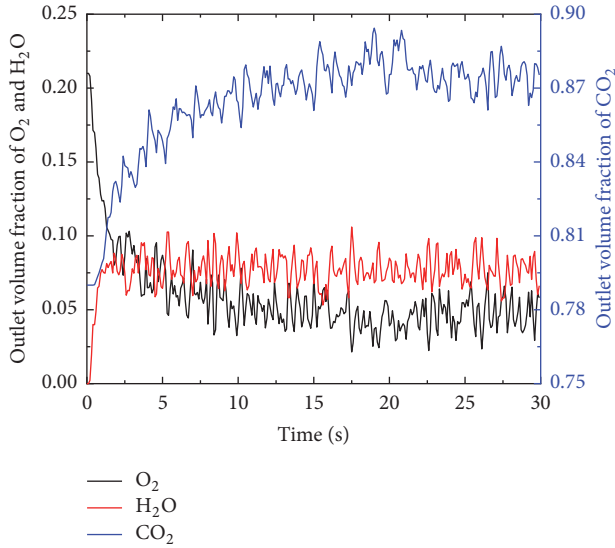


FIGURE 2: The gas (CO_2 , O_2 , and H_2O) volume fractions along with time at the outlet.

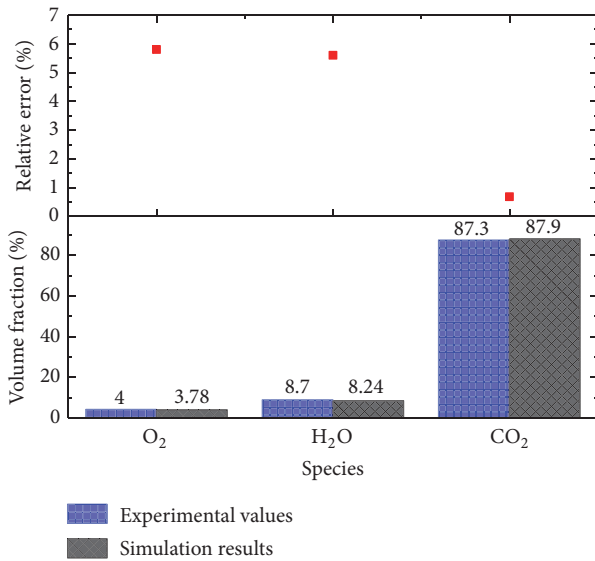


FIGURE 3: The experimental and simulation results of the outlet gas volume fractions.

outlet gradually increased from 79% to 86.42% and 0% to 9.36%, respectively, during the initial 10 s. At the same time, the volume fraction of O_2 decreased from 21% to 4.18%. However, the volume fractions for the CO_2 , O_2 and H_2O are relatively stable after 15 s of simulation, which fluctuate around 87.8%, 4.54%, and 7.55%. Therefore, the 20–30 s time-averaged calculation results are adopted to analyze the flow and combustion characteristics in this paper.

To demonstrate the accuracy of the simulation results, the experiment of 6 kWth bubbling fluidized bed under 21% O_2 /79% CO_2 atmosphere had been conducted at Southeast University, Nanjing, China [54]. Figure 3 shows the experimental and simulation values of CO_2 , O_2 , and H_2O volume fractions at the outlet. The relative errors of volume

fractions of O_2 , H_2O , and CO_2 are 5.8%, 5.6%, and 0.682%, respectively. The simulation values are in good agreement with the experimental results.

3.2. Flow Characteristic. Figure 4 shows the instantaneous volume fractions of coal and biomass under the conditions of primary air velocity, fuel feed rate, and biomass/coal mass ratio of 0.71 m/s, 0.87 kg/h, and 0.25, respectively. The volume fractions for coal and biomass phase are both 0.275 at the initial time. The coal and biomass entered the riser from the fuel inlet which is at the height of 0.18 m. It can be seen that the cluster of biomass and coal is formed at the fuel inlet (at 19.6 s) and falls down along the wall to the bottom of the riser and then rises up due to the primary air (from 19.8 s to 20.4 s). The formation of bubble can be observed while the primary air is rising. The bubbles grow, change the shapes, split, and combine along with the time building up. At last, the bubble breaks up above the secondary air inlet. The bubbling fluidization can be observed obviously in the figure of the instantaneous volume fraction distribution of coal and biomass.

The time and section-averaged volume fraction and pressure distribution along the axial height are shown in Figure 5. The volume fraction of coal is higher than that of biomass at the bottom of riser. The coal particles suffer greater gravity force due to the larger density, which lead to the more deposition of coal at the bottom of riser. However, the volume fraction of biomass is higher than biomass when the height is over 0.2 m. In comparison with Figure 4, it indicates that the biomass particles are more likely to rise up along with the primary air. The bed pressure distribution is also shown in Figure 5. The maximum of bed pressure is 2280 Pa. The bed pressure decreases along the axial height of the bed, which is maintained at -50 Pa when the height is higher than 0.8 m. The riser is divided into three zones which is dense zone (0–0.5 m), transition zone (0.5–0.8 m), and dilute zone (0.8–1.6 m), respectively.

Figure 6 shows the time-averaged axial velocity distribution of coal, biomass, and gas at heights of 0.05 m, 0.45 m, and 0.7 m. Combined with Figure 4, it can be seen that the velocity of gas phase is larger at the center due to the lower volume fraction of particles. The coal and biomass particles rise with the gas due to the effect of gas drag at the center. However, the volume fractions of coal and biomass are so high at the near wall region that the gas drag is not larger enough to carry the coal and biomass particles there. In that case, the velocities at the near wall region are negative which means the falling of particles. Comparing the velocities between the biomass and coal particles, the rise velocity of coal particles is lower than that of biomass particles. Consequently, the coal and biomass particles with low volume fraction flow up at the center and flow down with high volume fraction near the wall. In the rise reactor, the internal circulation of particle flow can be observed.

3.3. Temperature Profile. Figure 7 displays the section- and time-averaged simulation temperature during 20–30 s along the axial height of the riser and the experimental temperature values. The experimental values at 4 height points (0.16 m,

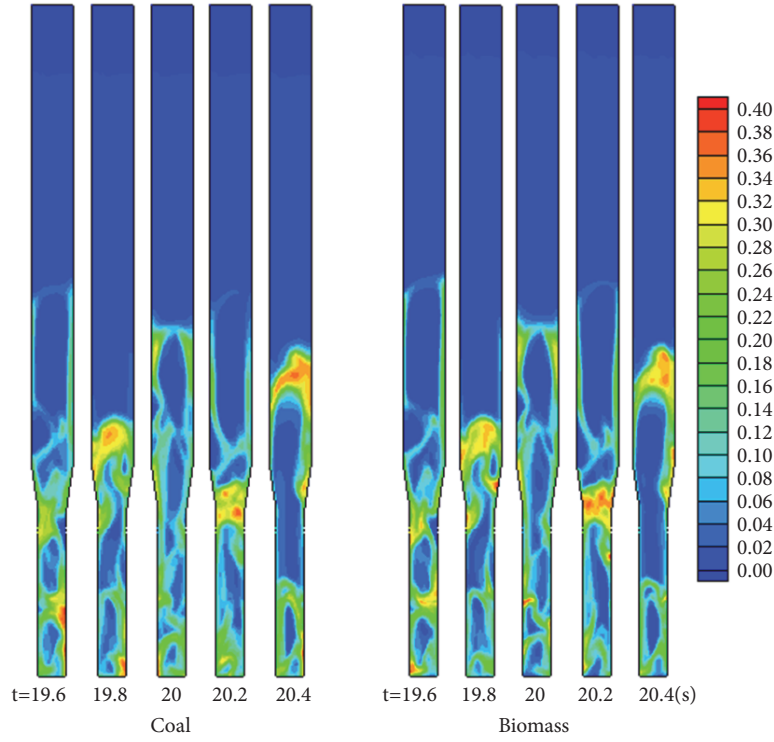


FIGURE 4: The instantaneous volume fraction of coal and biomass.

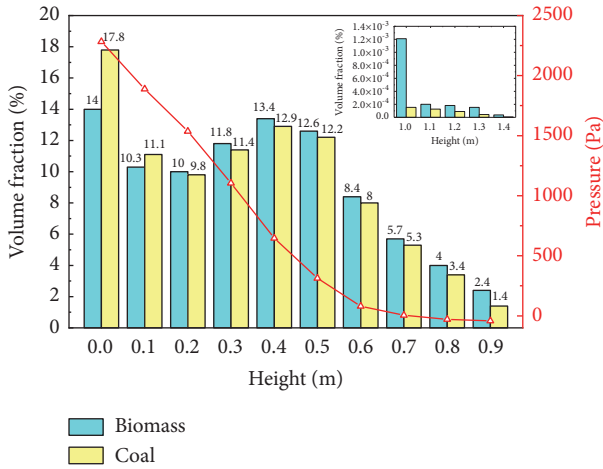


FIGURE 5: The time- and section-averaged volume fraction of coal and biomass along the height.

0.29 m, 0.8 m, and 1.2 m) are 1065 K, 1097 K, 1082 K, and 1033 K, respectively. The relative errors between the experimental value and the simulation temperature are separately 1.29%, 0.09%, 1.64%, and 3.82%. The larger relative error at 1.2 m may be due to the higher radial temperature gradient caused by the secondary air. Nevertheless, all of the temperature relative errors are less than 5%, which also indicated the accuracy of the established models in this work.

Figure 8 shows the instantaneous temperature distribution in the furnace. A high temperature region is observed

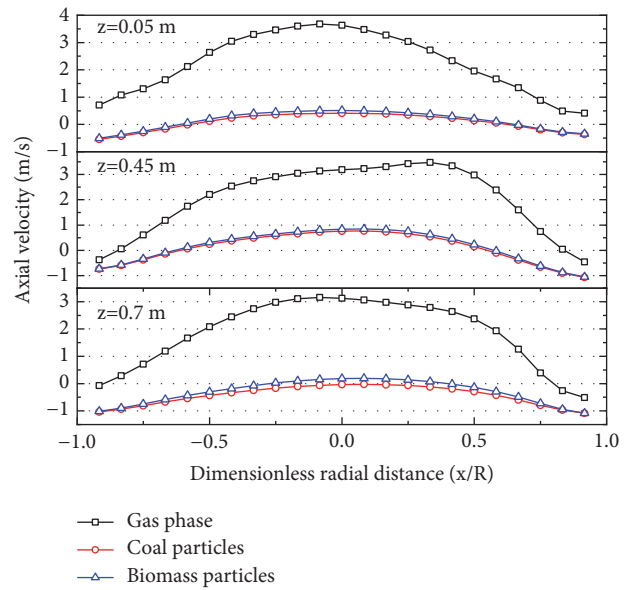


FIGURE 6: The axial velocity profile of coal, biomass, and gas phase (m/s).

above the fuel inlet (0.2~0.3 m) where temperature is about 1100~1200 K. This is due to the combustion of the volatiles which are released from the coal and biomass. In fact, combining with Figure 7, it can be seen that there is a low temperature region below the fuel inlet (0.16~0.18 m). The reason for this is that the heat is absorbed by the water evaporation and devolatilization of coal and biomass. The

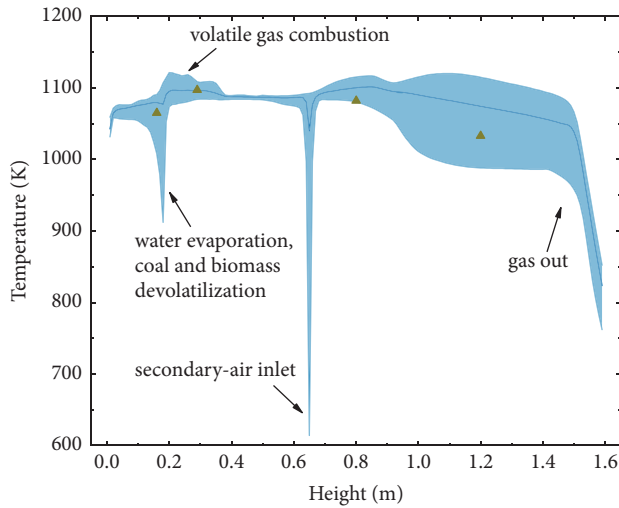


FIGURE 7: The curve: time- and section-averaged temperature of gas and the shadow region: time-averaged temperature range along the axial height.

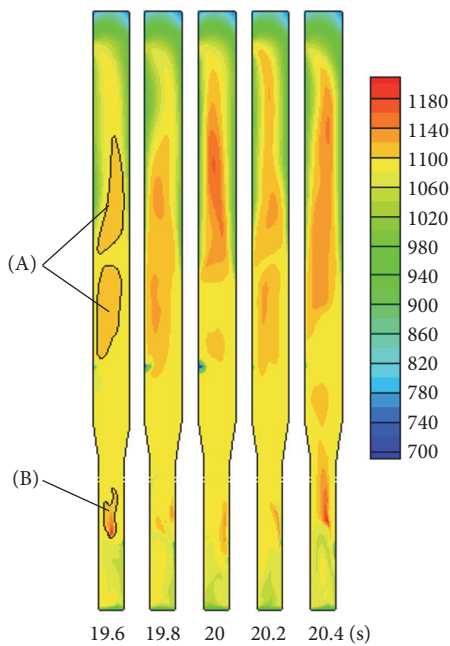


FIGURE 8: The contours of the instantaneous temperature distribution of gas during 19.5–20.5 s (K). Region (A): the high temperature region above the secondary air inlet due to the volatile reburning. Region (B): the high temperature region above the fuel inlet due to the volatile combustion.

average bed temperature at dense zone (0–0.5 m) is 1082 K. The temperature of transition zone (0.5–0.8 m) is uniform whose section-averaged temperature is about 1080 K. It is obvious that the temperature of gas increased again above the secondary air inlet. The cold secondary air (423 K) enters the riser which makes the volatiles reburn. Therefore, the temperature at the center is about 80 K higher than that near wall region.

3.4. Reaction Rates. Figure 9 displays the time-averaged devolatilization rates of biomass and coal. It can be seen that both coal and biomass release the volatile as soon as they enter the riser. The devolatilization rates of them are much higher than other heterogeneous reaction rates. The maximum values of coal and biomass are 0.00374 s^{-1} and 0.01495 s^{-1} . The devolatilization rate of coal is lower than that of biomass. Additionally, the mass fraction of coal is higher. In that case, the devolatilization process of coal lasts to the bottom of the riser, and the devolatilization process of biomass is nearly complete at the fuel inlet.

The homogeneous reaction rates (CH_4 , CO, tar, and H_2) are shown in Figure 10. The reaction rates are related to the species concentration and temperature. The higher concentration and temperature lead to the larger reaction rates. It can be seen that all of the homogeneous reaction rates are larger at the fuel inlet region because of rich O_2 and volatiles. In that case, most of the volatiles are consumed in the dense zone. The reaction rates decrease with the reduction of volatile and O_2 along the axial height. In fact, the H_2 reaction (R4) only occurs at the fuel inlet due to the higher reaction rate making H_2 being consumed completely in this region. However, the CH_4 and CO are not consumed completely in dense zone. The reburning of them occurs at the secondary air inlet due to the injection of O_2 . Consequently, the homogeneous reactions mainly occur in the dense zone.

3.5. Concentration of Gas Species. Figure 11 shows the contours of the instantaneous mass fractions of CH_4 , CO, and tar at around 20 s and the maximum values of them are 0.0418, 0.1785, and 0.1214, respectively. It can be found that the mass fractions of CH_4 and tar are high at the fuel inlet region because of the fuel devolatilization and the mass fraction of CO is high in the whole dense zone which may be due to the devolatilization and heterogeneous reactions process. Then, the mass fractions of them gradually drop with the height increase because of the homogeneous reactions. Actually, it is obvious that the CH_4 has not been completely consumed in the riser. In contrast, the tar has been completely consumed after the secondary air inlet. To combine with Figure 4, we can see that the mass fraction distribution of CO is related to the volume fraction of fuel which is due to the fact that the source of CO is not only from the devolatilization but also from the heterogeneous reactions.

Figure 12 displays the time- and section-averaged mass fraction distributions of H_2O , CO_2 , and O_2 along the axial height. As shown in Figure 12, we can see that the mass fraction of O_2 decreases rapidly from 16% to 3% in the dense zone (0–0.5 m) because of char and volatile combustion. The mass fraction of H_2O increases at the fuel inlet due to the chemical reaction and water evaporation. The mass fraction of CO_2 increases firstly at the bottom of riser because of the char combustion. The reduction of CO_2 at the fuel inlet is due to the heterogeneous reaction (R8) and the injection of primary air. Then, the volatile combustion leads to the rapid increase of CO_2 mass fraction. The mass fractions of CO_2 , H_2O , and O_2 are relatively uniform in the dilute zone.

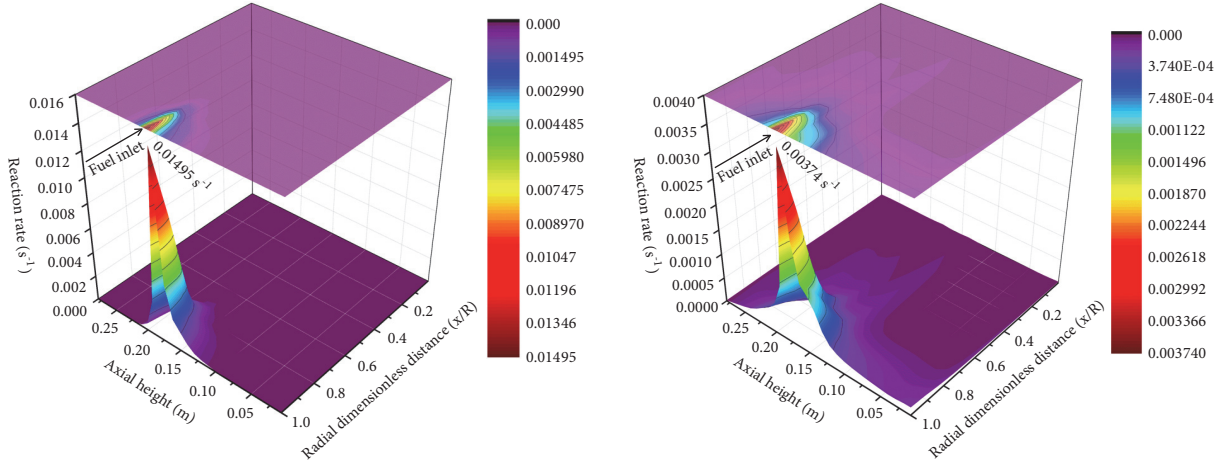


FIGURE 9: Coal (right) and biomass (left) devolatilization rates at fuel inlet region (s^{-1}).

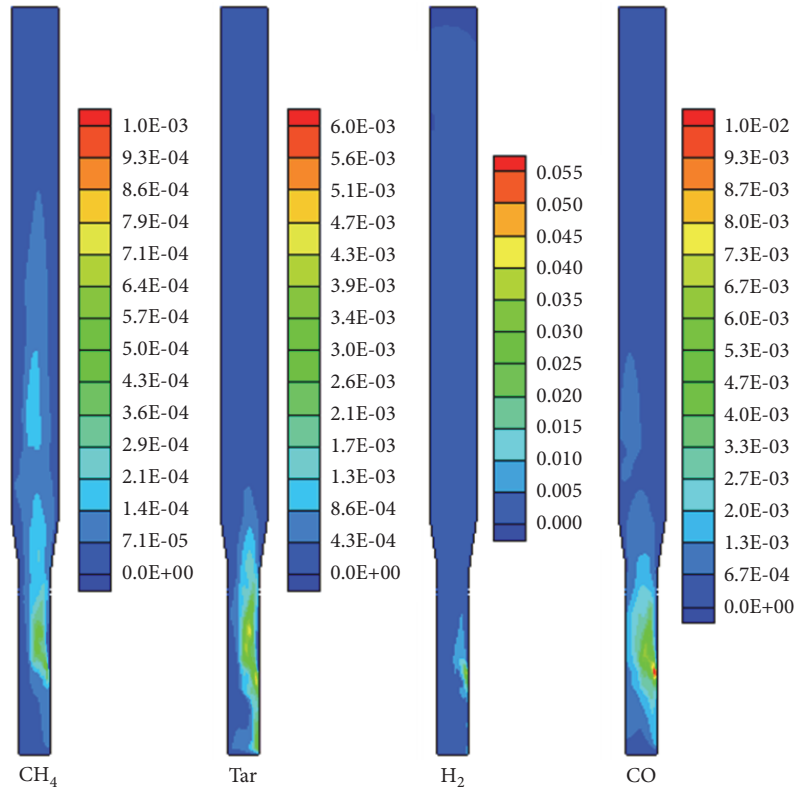


FIGURE 10: Time-averaged homogeneous reaction rates (CH_4 , CO , tar, and H_2) ($kmol/m^3 \cdot s$).

4. Conclusion

Based on an Euler-Euler approach, a complicated model including gas-solid multiphase flow, interphase heat and mass transfer, devolatilization of coal and biomass, and homogeneous and heterogeneous reactions has been established to investigate the combustion and flow characteristics of biomass cofiring with coal in a 6 kWth bubbling fluidized bed combustor under 21% O_2 /79% CO_2 atmosphere. The simulation values of CO_2 , O_2 , and H_2O volume fractions at the outlet and temperature distribution along the height of

the furnace were satisfactorily validated by the experimental data with no more than 6% relative errors. The results indicated the accuracy of the established models in this work.

The result shows that the bubbling fluidization can be observed obviously in the figure of the instantaneous volume fraction distribution of coal and biomass. During the simulation, two high temperature zones can be found in the riser reactor, which exist at the fuel inlet and dilute phase, respectively. One high temperature region is observed above the fuel inlet (0.18 m) where temperature is about 1100~1200 K. This is due to the combustion of the volatiles

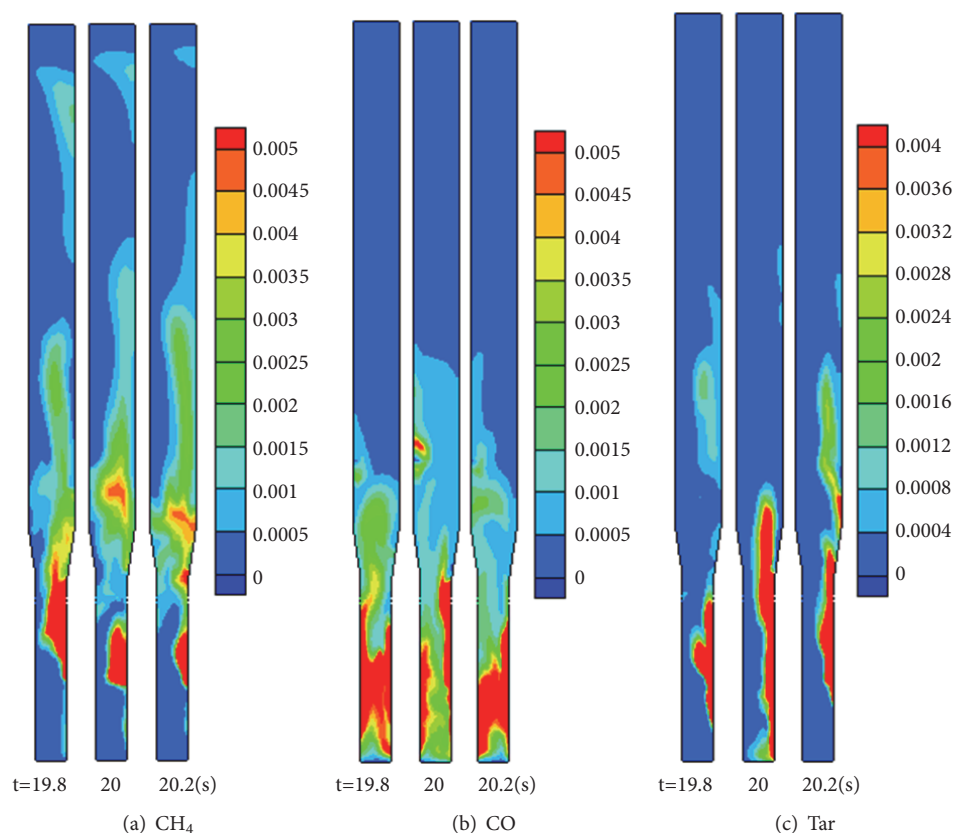


FIGURE 11: The contours of the instantaneous mass fractions of the main volatile species.

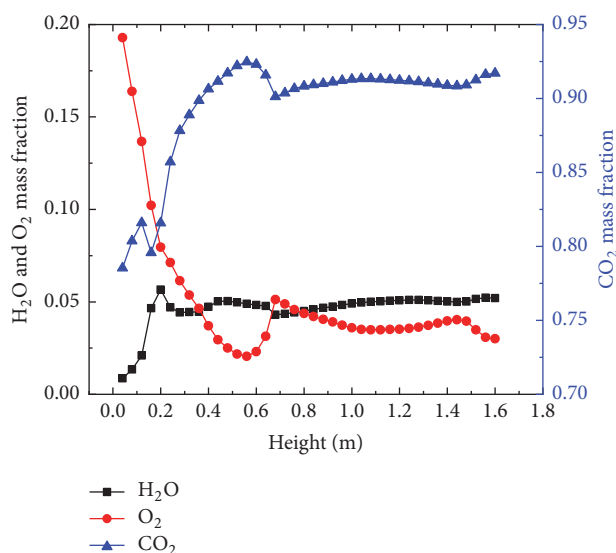


FIGURE 12: The time- and section-averaged mass fractions of H_2O , O_2 , and CO_2 along the height.

which are released from the coal and biomass. The other one is observed above the secondary air inlet (0.65 m). The cold secondary air (423 K) enters the riser which makes the volatiles reburn. Therefore, the temperature at the center is about 80 K higher than that near wall region. It also can be seen that both coal and biomass release the volatile as soon

as they enter the riser. The devolatilization rate of coal is lower than that of biomass. As the results indicated, all of the homogeneous reaction rates are larger at the fuel inlet region because of rich O_2 and volatiles and most of the volatiles are consumed in the dense zone. The reaction rates decrease with the reduction of volatile and O_2 along the axial height. High mass fraction of volatile gas (CH_4 , CO , etc.) is found at the fuel inlet, and the main reburning gas at the dilute phase is CH_4 . The mass fraction distribution of CO is related to the volume fraction of fuel which indicated that the source of CO is not only from the devolatilization but also from the heterogeneous reactions.

Actually, the detailed analysis and modelling of biomass cofiring under O_2/CO_2 atmosphere are extremely complex. On the basis of this theoretical study, a deeper insight of multiphase flow, heat and mass transfer, devolatilization, and homogeneous and heterogeneous reactions during coal and biomass cofiring under O_2/CO_2 atmosphere could be achieved. Certainly, the successful implementation of this technology still requires further study and full understanding of the characteristics of coal and biomass O_2/CO_2 cocombustion in the future.

Data Availability

The simulation and experimental data used to support the findings of this study are available from the corresponding author upon request.

Conflicts of Interest

The authors declare that there are no conflicts of interest regarding the publication of this paper.

Acknowledgments

The authors would like to acknowledge the National Natural Science Foundation of China (51376045) and Postgraduate Research & Practice Innovation Program of Jiangsu Province (KYCX18_0084) for financial support.

References

- [1] M. Parikka, "Global biomass fuel resources," *Biomass & Bioenergy*, vol. 27, no. 6, pp. 613–620, 2004.
- [2] K. R. G. Hein and J. M. Bemtgen, "EU clean coal technology - Co-combustion of coal and biomass," *Fuel Processing Technology*, vol. 54, no. 1-3, pp. 159–169, 1998.
- [3] M. Pronobis, "The influence of biomass co-combustion on boiler fouling and efficiency," *Fuel*, vol. 85, no. 4, pp. 474–480, 2006.
- [4] J. Dai, S. Sokhansanj, J. R. Grace, X. Bi, C. J. Lim, and S. Melin, "Overview and some issues related to co-firing biomass and coal," *The Canadian Journal of Chemical Engineering*, vol. 86, no. 3, pp. 367–386, 2008.
- [5] M. Akram, C. K. Tan, D. R. Garwood, M. Fisher, D. R. Gent, and W. G. Kaye, "Co-firing of pressed sugar beet pulp with coal in a laboratory-scale fluidised bed combustor," *Applied Energy*, vol. 139, pp. 1–8, 2015.
- [6] K. Veijonen, P. Vainikka, T. Järvinen, and E. Alakangas, "Biomass co-firing an efficient way to reduce greenhouse gas emissions," *VTT Processes*, March, p. A1, 2003.
- [7] B. M. Abraham, J. G. Asbury, E. P. Lynch, and A. P. S. Teotia, "Coal-oxygen process provides CO₂ for enhanced recovery," *Oil & Gas Journal*, 1982.
- [8] E. J. Anthony and H. Hack, "Oxy-fuel combustion on circulating fluidized bed (CFB)," *Oxy-Fuel Combustion for Power Generation and Carbon Dioxide (CO₂) Capture*, vol. 3, pp. 77–98, 2011.
- [9] C. S. Zhao, L. B. Duan, X. P. Chen, and C. Liang, *Latest Evolution of Oxy-Fuel Combustion Technology in Circulating Fluidized Bed*, Springer Berlin Heidelberg, 2009.
- [10] R. I. Singh and R. Kumar, "Current status and experimental investigation of oxy-fired fluidized bed," *Renewable & Sustainable Energy Reviews*, vol. 61, pp. 398–420, 2016.
- [11] S. C. Pickard, S. S. Daoood, M. Pourkashanian, and W. Nimmo, "Co-firing coal with biomass in oxygen- and carbon dioxide-enriched atmospheres for CCS applications," *Fuel*, vol. 137, pp. 185–192, 2014.
- [12] Y. Tan, L. Jia, and Y. Wu, "Some combustion characteristics of biomass and coal cofiring under oxy-fuel conditions in a pilot-scale circulating fluidized combustor," *ENERGY & FUELS*, vol. 27, no. 11, pp. 7000–7007, 2013.
- [13] L. Duan, Y. Duan, C. Zhao, and E. J. Anthony, "NO emission during co-firing coal and biomass in an oxy-fuel circulating fluidized bed combustor," *Fuel*, vol. 150, pp. 8–13, 2015.
- [14] R. Kumar and R. I. Singh, "Co-firing of coal with pine needles in a 20 kW oxy-fired bubbling fluidized bed," in *Experimental investigation*, Icaer, pp. 1–6, 2015.
- [15] R. Kumar and R. I. Singh, "An investigation in 20 kWth oxygen-enriched bubbling fluidized bed combustor using coal and biomass," *Fuel Processing Technology*, vol. 148, pp. 256–268, 2016.
- [16] A. A. Bhuiyan and J. Naser, "Numerical modeling of Biomass co-combustion with pulverized coal in a small scale furnace," in *Proceedings of the 6th BSME International Conference on Thermal Engineering, ICTE 2014*, pp. 504–511, Bangladesh, December 2014.
- [17] A. Stroh, F. Alobaid, J.-P. Busch, J. Ströhle, and B. Eppele, "3-D numerical simulation for co-firing of torrefied biomass in a pulverized-fired 1 MWth combustion chamber," *Energy*, vol. 85, pp. 105–116, 2015.
- [18] S. R. Gubba, D. B. Ingham, K. J. Larsen et al., "Numerical modelling of the co-firing of pulverised coal and straw in a 300 MWe tangentially fired boiler," *Fuel Processing Technology*, vol. 104, pp. 181–188, 2012.
- [19] C. Ghenai and I. Janajreh, "CFD analysis of the effects of co-firing biomass with coal," *Energy Conversion and Management*, vol. 51, no. 8, pp. 1694–1701, 2010.
- [20] J. Li, A. Brzdekiewicz, W. Yang, and W. Blasiak, "Co-firing based on biomass torrefaction in a pulverized coal boiler with aim of 100% fuel switching," *Applied Energy*, vol. 99, pp. 344–354, 2012.
- [21] F. Tabet and I. Gökalp, "Review on CFD based models for co-firing coal and biomass," *Renewable & Sustainable Energy Reviews*, vol. 51, pp. 1101–1114, 2015.
- [22] A. Gungor, "Simulation of co-firing coal and biomass in circulating fluidized beds," *Energy Conversion and Management*, vol. 65, pp. 574–579, 2013.
- [23] X. Zhang, M. Ghamari, and A. Ratner, "Numerical modeling of co-firing a light density biomass, oat (*Avena sativa*) hulls, and chunk coal in fluidized bed boiler," *Biomass & Bioenergy*, vol. 56, pp. 239–246, 2013.
- [24] A. A. Bhuiyan and J. Naser, "CFD modelling of co-firing of biomass with coal under oxy-fuel combustion in a large scale power plant," *Fuel*, vol. 159, pp. 150–168, 2015.
- [25] A. A. Bhuiyan and J. Naser, "Computational modelling of co-firing of biomass with coal under oxy-fuel condition in a small scale furnace," *Fuel*, vol. 143, pp. 455–466, 2015.
- [26] T. I. Gombosi, *Gaskinetic Theory*, Cambridge University Press, Cambridge, 1994.
- [27] M. J. V. Goldschmidt, R. Beetstra, and J. A. M. Kuipers, "Hydrodynamic modelling of dense gas-fluidised beds: Comparison of the kinetic theory of granular flow with 3D hard-sphere discrete particle simulations," *Chemical Engineering Science*, vol. 57, no. 11, pp. 2059–2075, 2002.
- [28] C. K. K. Lun, S. B. Savage, D. J. Jeffrey, and N. Chepurniy, "Kinetic theories for granular flow: inelastic particles in Couette flow and slightly inelastic particles in a general flowfield," *Journal of Fluid Mechanics*, vol. 140, pp. 223–256, 1984.
- [29] L. Huilin, L. Wenti, B. Rushan, Y. Lidan, and D. Gidaspow, "Kinetic theory of fluidized binary granular mixtures with unequal granular temperature," *Physica A: Statistical Mechanics and its Applications*, vol. 284, no. 1, pp. 265–276, 2000.
- [30] L. Huilin, D. Gidaspow, and E. Manger, "Kinetic theory of fluidized binary granular mixtures," *Physical Review E: Statistical, Nonlinear, and Soft Matter Physics*, vol. 64, no. 6, pp. 1–8, 2001.
- [31] L. Huilin and D. Gidaspow, "Hydrodynamics of binary fluidization in a riser: CFD simulation using two granular temperatures," *Chemical Engineering Science*, vol. 58, no. 16, pp. 3777–3792, 2003.

- [32] W. Shuai, C. Juhui, L. Guodong, L. Huilin, Z. Feixiang, and Z. Yanan, "Predictions of coal combustion and desulfurization in a CFB riser reactor by kinetic theory of granular mixture with unequal granular temperature," *Fuel Processing Technology*, vol. 126, pp. 163–172, 2014.
- [33] J. Shen, X.-S. Wang, M. Garcia-Perez, D. Mourant, M. J. Rhodes, and C.-Z. Li, "Effects of particle size on the fast pyrolysis of oil mallee woody biomass," *Fuel*, vol. 88, no. 10, pp. 1810–1817, 2009.
- [34] W. Fu, Y. Zhang, H. Han, and D. Wang, "A general model of pulverized coal devolatilization," *Fuel*, vol. 68, no. 4, pp. 505–510, 1989.
- [35] J. Reina, E. Velo, and L. Puigjaner, "Kinetic study of the pyrolysis of waste wood," *Industrial & Engineering Chemistry Research*, vol. 37, no. 11, pp. 4290–4295, 1998.
- [36] E. Desroches-Ducarne, E. Marty, G. Martin, and L. Delfosse, "Co-combustion of coal and municipal solid waste in a circulating fluidized bed," *Fuel*, vol. 77, no. 12, pp. 1311–1315, 1998.
- [37] J. B. Howard, G. C. Williams, and D. H. Fine, "Kinetics of carbon monoxide oxidation in postflame gases," *Symposium (International) on Combustion*, vol. 14, no. 1, pp. 975–986, 1973.
- [38] S. Chapman, T. G. Cowling, and D. Park, "The Mathematical Theory of Non-Uniform Gases," *American Journal of Physics*, vol. 30, no. 5, pp. 389–389, 1962.
- [39] J. M. Heikkinen, B. C. H. Venneker, G. di Nola, W. de Jong, and H. Spliethoff, "CFD simulation and experimental validation of co-combustion of chicken litter and MBM with pulverized coal in a flow reactor," *Fuel Processing Technology*, vol. 89, no. 9, pp. 874–889, 2008.
- [40] A. Gungor, "Two-dimensional biomass combustion modeling of CFB," *Fuel*, vol. 87, no. 8–9, pp. 1453–1468, 2008.
- [41] J. Adanez, P. Gayán, G. Grasa, L. F. De Diego, L. Armesto, and A. Cabanillas, "Circulating fluidized bed combustion in the turbulent regime: Modelling of carbon combustion efficiency and sulphur retention," *Fuel*, vol. 80, no. 10, pp. 1405–1414, 2001.
- [42] Q. Wang, Z. Luo, X. Li, M. Fang, M. Ni, and K. Cen, "A mathematical model for a circulating fluidized bed (CFB) boiler," *Energy*, vol. 24, no. 7, pp. 633–653, 1999.
- [43] I. Petersen and J. Werther, "Experimental investigation and modeling of gasification of sewage sludge in the circulating fluidized bed," *Chemical Engineering and Processing: Process Intensification*, vol. 44, no. 7, pp. 717–736, 2005.
- [44] I. Matsui, D. Kunii, and T. Furusawa, "Study of char gasification by carbon dioxide. I. Kinetic study by thermogravimetric analysis," *Industrial & Engineering Chemistry Research*, vol. 26, no. 1, pp. 91–95, 1987.
- [45] B. R. Stanmore and P. Gilot, "Review-calcination and carbonation of limestone during thermal cycling for CO₂ sequestration," *Fuel Processing Technology*, vol. 86, no. 16, pp. 1707–1743, 2005.
- [46] I. Matsui, D. Kunii, and T. Furusawa, "Study of fluidized bed steam gasification of char by thermogravimetrically obtained kinetics," *Journal of Chemical Engineering of Japan*, vol. 18, no. 2, pp. 105–113, 1985.
- [47] D. Gidaspow, R. Bezburuah, and J. Ding, "Hydrodynamics of circulating fluidized beds: Kinetic theory approach," in *Proceedings of the 7th international conference on fluidization*, Gold Coast, Australia, May 1992.
- [48] D. J. Gunn, "Transfer of heat or mass to particles in fixed and fluidised beds," *International Journal of Heat and Mass Transfer*, vol. 21, no. 4, pp. 467–476, 1978.
- [49] K. Myöhänen, T. Hyppänen, J. Miettinen, and R. Parkkonen, "Three-dimensional modeling and model validation of circulating fluidized bed combustion," in *Proceedings of the 17th International Conference on Fluidized Bed Combustion*, pp. 293–303, USA, May 2003.
- [50] A. Gungor and N. Eskin, "Two-dimensional coal combustion modeling of CFB," *International Journal of Thermal Sciences*, vol. 47, no. 2, pp. 157–174, 2008.
- [51] A. Goyal and A. Rehmat, "Modeling of a fluidized-bed coal carbonizer," *Industrial & Engineering Chemistry Research*, vol. 32, no. 7, pp. 1396–1410, 2002.
- [52] W. Zhou, C. Zhao, L. Duan, D. Liu, and X. Chen, "CFD modeling of oxy-coal combustion in circulating fluidized bed," *International Journal of Greenhouse Gas Control*, vol. 5, no. 6, pp. 1489–1497, 2011.
- [53] B. Chalermsoonsuwan, T. Chanchuey, W. Buakhao, D. Gidaspow, and P. Piumsomboon, "Computational fluid dynamics of circulating fluidized bed downer: Study of modeling parameters and system hydrodynamic characteristics," *Chemical Engineering Journal*, vol. 189–190, pp. 314–335, 2012.
- [54] L. Zhao, B. F. Q. Jia, and C. Zhao, "Numerical and experimental study on coal and biomass co-firing in the fluidized bed under O₂/CO₂ atmospheres," in *Proceedings of the 35th International Symposium on Combustion*, San Francisco, Calif, USA, 2014.

Research Article

Experimental Investigation of Combustion Kinetics of Wood Powder and Pellet

Peng Haobin,¹ Yuesheng Li,² Yunquan Li ,² Fangyang Yuan,³ and Guohua Chen ¹

¹School of Mechanical and Automotive Engineering, South China University of Technology, Guangzhou 510640, China

²Guangdong Institute of Special Equipment Inspection and Research Shunde Branch, Shunde 528300, China

³School of Mechanical Engineering, Jiangnan University, Wuxi 214122, China

Correspondence should be addressed to Guohua Chen; mmghchen@scut.edu.cn

Received 3 May 2018; Revised 15 July 2018; Accepted 30 July 2018; Published 2 September 2018

Academic Editor: Hiroaki Watanabe

Copyright © 2018 Peng Haobin et al. This is an open access article distributed under the Creative Commons Attribution License, which permits unrestricted use, distribution, and reproduction in any medium, provided the original work is properly cited.

The combustion kinetic characteristics of wood powder and pellet were investigated within thermogravimetric analyser (TGA) and tube furnace system. The kinetic parameters of these two different forms of woody fuel were measured and derived by double-step-and-double-equal and isothermal method, respectively. The results showed that the combustion mechanisms of wood powder kept consistent through the whole process, while the combustion mechanisms of wood pellet differed significantly between the volatile and char combustion stages. The most probable mechanism functions of the two different forms of woody fuel were not the same due to the differences in internal heat and mass transfer properties. In addition, activation energy values varied from $92.33 \text{ kJ}\cdot\text{mol}^{-1}$ for wood powder to $71.20 \text{ kJ}\cdot\text{mol}^{-1}$ for wood pellet, while the preexponential factor value of wood powder ($2.55 \times 10^8 \text{ s}^{-1}$) was far greater than the one of the wood pellet (78.55 s^{-1}) by seven orders of magnitude.

1. Introduction

Suffering the consequences of excessive use of fossil fuel, the countries all over the world contribute more and more to renewable energy development and utilization [1–3]. Biomass energy is the most potential renewable energy in near future, because it is easy to store and convenient to transport and its application technology is ordinary and mature. Furthermore, from production to utilization, the cycle chain of CO_2 emissions from biomass fuel closes to zero [4, 5]. The annual use of wood, widely in construction, furniture manufacturing, packaging, and handicraft, is more than 400 million m^3 , yet the processing rate is only about 65% [6]. The remaining compounds such as leftover sawdust should be utilized vigorously to promote energy conservation and emission reduction [7, 8]. The most effective way to use the remains is to extrude them into granules with uniform shape and density and then directly burn them for heating and power generation [9–11].

The previous researches of biomass granular fuel mainly focus on the macro combustion characteristics. Ge et al. [12] calculated the comprehensive combustion characteristics of

four kinds of the man-made board in air atmosphere by the thermogravimetric curve and compared the characteristics of synthetic combustion performances. Cuiping et al. [13] piecewise compared the combustion characteristics of three types of granular fuels, namely, corn straw, wood sawdust, and mixed sawdust, through the apparent activation energy values and the preexponential factor values under different combustion stages. Qing et al. [14] calculated the activation energy values and the preexponential factor values of four kinds of biomass materials by the Coats-Redfern method and the first order model, and they came to a conclusion that the wood sawdust is less active than the remaining three species of herbaceous biomass. The calculation compared well with the experimental results. In addition, some scholars explored the granular fuel pyrolysis and combustion rules by mathematical simulation, such as Haseli [15], establishing a mathematical model to describe the combustion process of a single biomass particle, based on a one-dimensional model of quality, momentum, and energy conservation during combustion, with the combination of combustion, pyrolysis kinetic equations.

TABLE 1: Proximate and ultimate analysis of biomass granular fuel.

Proximate analysis /wt %					Ultimate analysis /wt %			
M_{ad}	V_{ad}	A_{ad}	FC_{ad}	$[C]_{daf}$	$[H]_{daf}$	$[O]_{daf}$	$[N]_{daf}$	$[S]_{daf}$
5.55	83.08	1.32	10.05	52.02	5.07	42.46	0.41	0.04

Owing to the advantages of quick transmission of mass and heat and to acquire more accurate kinetic features of the experimental materials, the samples in kinetic experiments were mostly in fine particles (diameter <0.20 mm) and in small amount (<20 mg) [16–20]. However, the internal heat and mass transfer should not be ignored because of the objective existence while researching on the combustion kinetics of the whole granule [17, 21]. For the best of our knowledge, there was no combustion kinetic research of wood pellet based on the isothermal method in previous studies. To further explore the differences in the combustion kinetic characteristics between wood powder and pellet, some thermal kinetic analyses were conducted in the respective status of the same kind of wood. The results are expected to be the supplement to the existing research of wood pellet combustion kinetics.

2. Materials and Methods

2.1. Materials. The experimental materials were wood-based granular fuel produced by a contract-energy-management enterprise in Foshan, Guangdong. The sawdust and residues produced during furniture manufacturing were crushed and squeezed into densified cylindrical granules with approximately 8 mm in diameter, 40–60 mm in length, and about 950 kg/m³ in density, including eucalyptus, fir, beech, and walnut, collectively referred to as miscellaneous wood. The samples could be represented by sampling in dispersive points from the same product batch. According to the national standard DL/T 568 and GB/T 28731, the proximate analysis and ultimate analysis results are listed in Table 1. Before the experiment, some pellets were cut to both ends of the flush, with the mass of 1000 ± 5 mg, and the others were ground and sieved to powders with the diameter less than 0.18 mm. All samples were stored in a desiccator standby.

2.2. Apparatus and Instrument

2.2.1. Wood Powder Analysis. The experiments were conducted in an STA-449F3 thermogravimetric analyser (NET-ZSCH, Germany), with powder samples weighing approximately 10.0 mg, using air as the atmosphere gas at the flow rate of 60 mL/min. The reaction temperature rose to 1000°C from the environmental temperature in heating rates of 10, 20, 30, and 40°C/min, respectively.

2.2.2. Wood Pellet Analysis. The experiments of wood pellet were conducted in a self-made tube furnace system. The main part of the device was a tube reactor, typed SK-4-4-16Q, with an inner diameter of 60 mm and mid-effective heating length of 300 mm, produced by Wuhan Yahua Electric Furnace Ltd. When the experiment began, the influx of air was fed into

the tube furnace at the flow rate of 3 L/min. As the furnace atmosphere was stable and the temperature reached the set value, i.e., 800, 1000, 1200, and 1400°C, a corundum crucible carrying a pellet was put into the center of the reactor rapidly, and then the sample was ignited. Afterwards at the selected time moment, i.e., 12, 24, . . . , 60, 90, . . . , 210 s, the crucible was taken out and put into a vessel filled with argon immediately, and then the vessel was sealed tightly and put into a water sink to cool down quickly. After that, the sample which kept the morphology, composition, and properties was weighed, and finally a set of isothermal TG (Thermal Gravity Analysis) curves were drawn.

2.3. Method. The combustion process of wood obeys the Arrhenius law; the basic kinetic equation is generally described as follows:

$$\frac{d\alpha}{dt} = k(T) f(\alpha) = A \exp\left(-\frac{E}{RT}\right) f(\alpha) \quad (1)$$

where α is the conversion of the combustible part of the sample, which is described as follows:

$$\alpha = \frac{m_0 - m_t}{m_0 - m_\infty} \quad (2)$$

where m is the mass of the sample; m_0 , m_t , and m_∞ are, respectively, the mass of the sample at initial time, t moment, and finally time; $k(T)$ is the combustion rate constant; A is preexponential factor, s⁻¹; E is apparent activation energy, kJ/mol; R is the ideal gas law constant, 8.314 J/(mol·K); and $f(\alpha)$ is the reaction model.

2.3.1. Wood Powder Thermogravimetric Analysis. By the double-step-and-double-equal method for wood powder, concrete steps are as follows [22].

(a) *Determination of Most Probable Mechanism Function $G(\alpha)$.* Equation (3) is integrated and transformed into Flynn-Wall-Ozawa equation as

$$\lg \beta = \lg \left[\frac{AE}{RG(\alpha)} \right] - 2.315 - 0.4567 \frac{E}{RT} \quad (3)$$

where β is the heating rate, obtained from the formula as follows:

$$\beta = \frac{dT}{dt} \quad (4)$$

transforming (3) into

$$\lg G(\alpha) = \left(\lg \frac{AE}{R} - 2.315 - 0.4567 \frac{E}{RT} \right) - \lg \beta. \quad (5)$$

TABLE 2: Nine commonly used mechanism functions.

$G(\alpha)$	Expressions
$D_1(\alpha)$	$\alpha^2 = 0.2500 \left(\frac{t}{t_{0.5}} \right)$
$D_2(\alpha)$	$(1 - \alpha) \ln(1 - \alpha) + \alpha = 0.1534 \left(\frac{t}{t_{0.5}} \right)$
$D_3(\alpha)$	$[1 - (1 - \alpha)^{1/3}]^2 = 0.0426 \left(\frac{t}{t_{0.5}} \right)$
$D_4(\alpha)$	$\left(1 - \frac{2\alpha}{3}\right) - (1 - \alpha)^{2/3} = 0.0367 \left(\frac{t}{t_{0.5}} \right)$
$R_2(\alpha)$	$[1 - (1 - \alpha)^{1/2}] = 0.2929 \left(\frac{t}{t_{0.5}} \right)$
$R_3(\alpha)$	$[1 - (1 - \alpha)^{1/3}] = 0.2929 \left(\frac{t}{t_{0.5}} \right)$
$F_1(\alpha)$	$\ln(1 - \alpha) = 0.6931 \left(\frac{t}{t_{0.5}} \right)$
$A_2(\alpha)$	$[-\ln(1 - \alpha)]^{1/2} = 0.8326 \left(\frac{t}{t_{0.5}} \right)$
$A_3(\alpha)$	$[-\ln(1 - \alpha)]^{1/3} = 0.8850 \left(\frac{t}{t_{0.5}} \right)$

By substituting the α at the same temperature on the TG curves corresponding to different heating rates and different mechanism function $G(\alpha)$ in (5), a series of correlation coefficients R^2 can be achieved with $\lg G(\alpha)$ - $\lg \beta$ linear regression. The R^2 is closer to 1, the corresponding $G(\alpha)$ describes the wood powder combustion process better, and, hence, the closest one is the most probable mechanism function.

(b) *Derivation of E and A.* According to (3), a plot of $\lg \beta$ - $1/T$ corresponds to a straight line with the same α at different heating rates and the determinate form of $G(\alpha)$, from which the values of E and A can be derived from the slope and intercept, respectively.

2.3.2. Wood Pellet Thermogravimetric Analysis

(a) *Determination of Most Probable Mechanism Function $G(\alpha)$.* The most probable mechanism function of granular fuel combustion can be deduced from the coordination of the experimental data and the kinetic models, namely, reduced time method [22]. Nine commonly used mechanism functions (Table 2) were tested in this paper. If an experimental curve overlaps a theoretical curve, or the experimental data points almost fall in one theoretical curve by comparing the square of deviance [22], the $G(\alpha)$ corresponding to the theoretical curve is the most probable mechanism function, through

$$G(\alpha) = kt = \frac{G(\alpha)_{\alpha=0.5}}{G(\alpha)_{\alpha=1.0}} \left(\frac{t}{t_{0.5}} \right) \quad (6)$$

where $t_{0.5}$ is the time length while $\alpha=0.5$; $G(\alpha)_{\alpha=0.5}$ is the $G(\alpha)$ while $\alpha=0.5$; and $G(\alpha)_{\alpha=1.0}$ is the $G(\alpha)$ while $\alpha=1.0$.

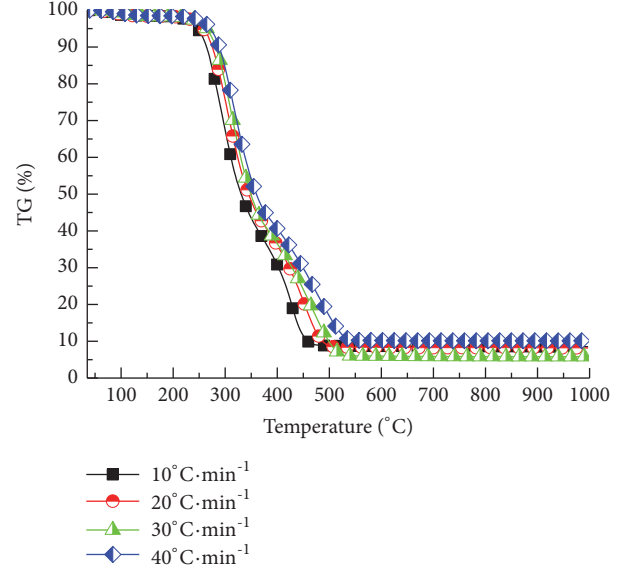


FIGURE 1: Combustion TG curves of wood powders.

(b) *Derivation of E and A.* By transforming the determinate most probable mechanism function to plot a straight line including α and t , n and k can be achieved according to the slope and intercept. And then substituting the k_i and T_i corresponding to various temperature sections into Arrhenius equation, one has

$$\ln k = \ln A - \frac{E}{RT}. \quad (7)$$

Plotting the straight line of $\ln k$ against $1/T$, E , and A can be derived from the slope and intercept, respectively.

3. Results and Discussion

3.1. *The Solution of Combustion Kinetic Parameters of Wood Powder.* The TG and DTG (Differential Thermal Gravity) curves of wood powder combustion are shown in Figures 1 and 2, respectively.

By substituting the α at the same temperature in four TG curves, heating rates, and different mechanism functions in (5), with $\lg G(\alpha)$ - $\lg \beta$ linear regression, the fitting results were achieved (shown in Table 3). It was clear that the R^2 closest to 1 corresponds to the function $G(\alpha)=(1-\alpha)^n$ ($n=-1$), namely, the most probable mechanism function to describe the combustion process of wood powder.

And then, by substituting the T and β corresponding to the same α at four TG curves of different heating rates and the determinate $G(\alpha)$ in (3), with linear regression of $\lg \beta$ - $1/T$, a series of E values were derived from the slopes and A values from the intercepts, and the results are shown in Table 4.

The fitting results of E values shown in Table 4 were reliable for the correlation coefficient R^2 values varying from 0.9030 to 0.9991. The results of A values shown in Table 4 were solved according to the E values and the determinate $G(\alpha)$.

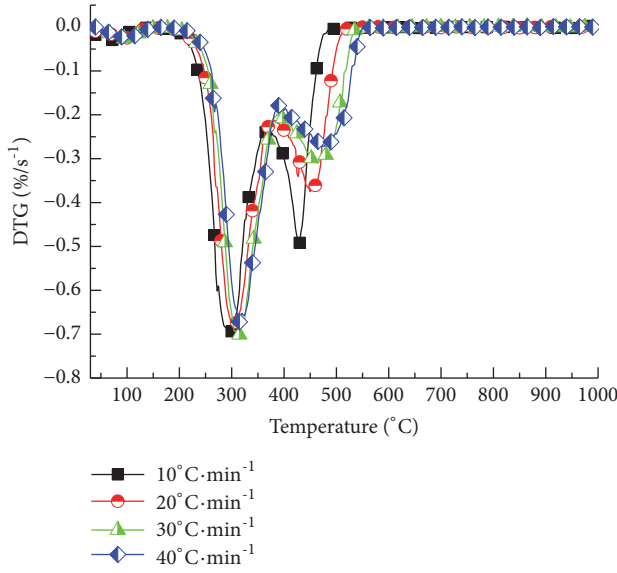


FIGURE 2: Combustion DTG curves of wood powders.

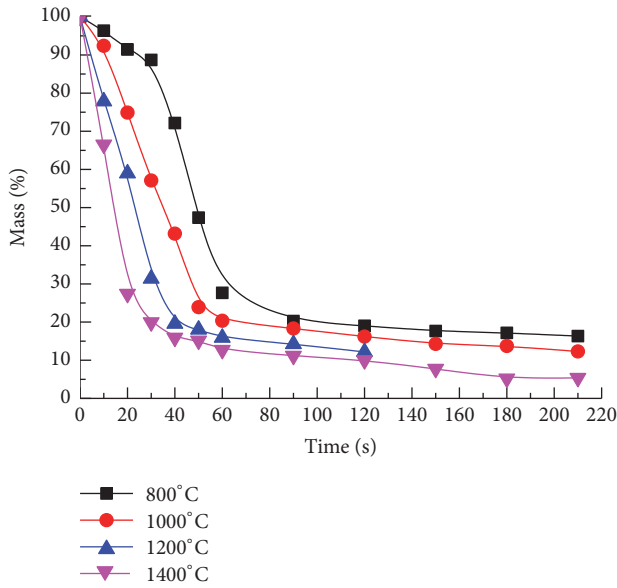


FIGURE 3: Mass loss curves of wood pellet combustion.

Global average E and A was $92.33 \text{ kJ mol}^{-1}$ and $2.55 \times 10^8 \text{ s}^{-1}$, respectively.

3.2. The Solution of Combustion Kinetic Parameters of Wood Pellet

3.2.1. The Determination of Most Probable Mechanism Function $G(\alpha)$. The weight loss curves of wood pellet during isothermal combustion are shown in Figure 3. The fitting results of $\alpha-t/t_{0.5}$ theory and experimental curves are shown in Figure 4. It was clear that the experimental data fell on the theoretical curve of function $G(\alpha)=A_2(\alpha)$ or nearby when the conversion rate of α varied in the range of $[0.10, 0.80)$.

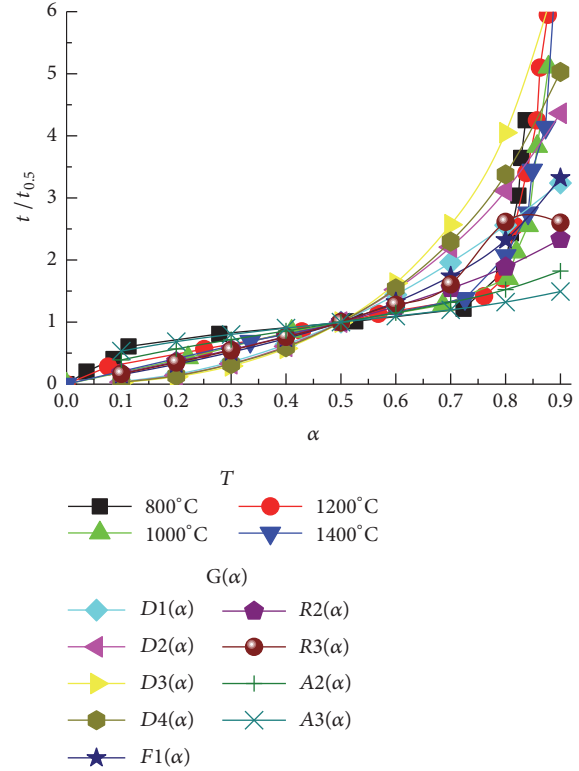


FIGURE 4: Most probable mechanism function fitting curves of wood pellet combustion reaction.

(a) *The Derivation of E and A .* The most probable mechanism function $A_2(\alpha)$ was transformed from

$$1 - \alpha = e^{-kt^n} \quad (8)$$

transforming (8) into

$$\ln [-\ln (1-\alpha)]=n \ln t+\ln k. \quad (9)$$

By plotting the straight line of $\ln [-\ln (1-\alpha)]-\ln t$ as shown in Figure 5, the n and k could be derived from the slope and intercept, respectively.

Substitute the k_i and T_i of the four temperature sections into Arrhenius equation as

$$\ln k=\ln A-\frac{E}{RT}. \quad (10)$$

Plotting the straight line of $\ln k$ against $1/T$ as shown in Figure 6, E and A were derived from the slope and the intercept to be $71.20 \text{ kJ} \cdot \text{mol}^{-1}$ and 78.55 s^{-1} , respectively, correlation coefficient R^2 to be 0.9844.

3.2.2. Comparison of Combustion Kinetic Characteristics between Wood Powder and Pellet. Wood pellet combustion is a complex reaction of multiple materials, multiple phases, and multiple steps [15, 24, 25]; thus the kinetics triplet, which might be the apparent result of multistep reactions, usually varies with the combustion condition and the reaction

TABLE 3: Commonly used mechanism functions [22, 23].

$G(\alpha)$	Mechanism	Expressions	R^2
$G_1(\alpha)$	Power law, $n=[1/4, 1/3, 1/2, 3/2, 2]$	α^n	0.9801
$G_2(\alpha)$	Two-dimensional diffusion	$\alpha + (1 - \alpha)\ln(1 - \alpha)$	0.9817
$G_3(\alpha)$	Three-dimensional diffusion, $n=[1/2, 2]$	$[1 - (1 - \alpha)^{1/3}]^n$	0.9833
$G_4(\alpha)$	Ginstling-Brounshtein equation	$1 - \left(\frac{2}{3}\right)\alpha - (1 - \alpha)^{2/3}$	0.9823
$G_5(\alpha)$	Avrami-Erofeev, $n=[1/4, 1/3, 2/5, 1/2, 2/3, 3/4, 1, 3/2, 2, 3, 4]$	$[-\ln(1 - \alpha)]^n$	0.9847
$G_6(\alpha)$	Chemical reaction, $n \neq 1$	$\frac{1 - (1 - \alpha)^{1-n}}{(1 - n)}$	0.9934
$G_7(\alpha)$	Phase boundary controlled reaction, $n=[1/4, 1/3, 1/2, 2, 3, 4]$	$1 - (1 - \alpha)^n$	0.9837
$G_8(\alpha)$	Chemical reaction, $n=[-2, -1, -1/2]$	$(1 - \alpha)^n$	0.9992
$G_9(\alpha)$	Index law, $n=[1, 2]$	$\ln \alpha^n$	0.9954
$G_{10}(\alpha)$	Jander equation, $n=[1/2, 2]$	$[1 - (1 - \alpha)^{1/2}]^n$	0.9825
$G_{11}(\alpha)$	Anti-Jander equation	$[(1 + \alpha)^{1/3} - 1]^2$	0.9781
$G_{12}(\alpha)$	Zhuravlev equation	$[(1 - \alpha)^{-1/3} - 1]^2$	0.9859
$G_{13}(\alpha)$	P-T equation	$\ln \left[\frac{\alpha}{(1 - \alpha)} \right]$	0.9984
$G_{14}(\alpha)$	Three-dimensional diffusion	$3 [1 - (1 - \alpha)^{1/3}]$	0.9833
$G_{15}(\alpha)$	Two-dimensional diffusion	$2 [1 - (1 - \alpha)^{1/2}]$	0.9825
$G_{16}(\alpha)$	Chemical reaction (second order)	$(1 - \alpha)^{-1} - 1$	0.9882
$G_{17}(\alpha)$	Nucleation and growth	$[-\ln(1 - \alpha)]^{1/n}$	0.9847
$G_{18}(\alpha)$	Power law	$\alpha^{1/n}$	0.9801

TABLE 4: Combustion kinetic parameters of wood powders under different conversion rates.

$\alpha/\%$	$E/\text{kJ}\cdot\text{mol}^{-1}$	A/s^{-1}	R^2	$\alpha/\%$	$E/\text{kJ}\cdot\text{mol}^{-1}$	A/s^{-1}	R^2
0.05	72.70	1.26×10^8	0.9991	0.50	101.96	3.87×10^8	0.9646
0.10	80.05	1.99×10^8	0.9977	0.55	104.17	3.07×10^8	0.9316
0.15	76.29	5.91×10^7	0.9795	0.60	94.52	3.85×10^7	0.9030
0.20	87.46	3.10×10^8	0.9979	0.65	97.86	3.12×10^7	0.9243
0.25	91.47	4.38×10^8	0.9973	0.70	99.62	2.41×10^7	0.9432
0.30	94.60	5.33×10^8	0.9960	0.75	96.90	1.31×10^7	0.9583
0.35	97.52	6.23×10^8	0.9951	0.80	90.22	5.32×10^6	0.9700
0.40	99.69	6.32×10^8	0.9912	0.85	82.78	2.30×10^6	0.9725
0.45	101.83	6.06×10^8	0.9845	-	-	-	-

progress. Designed towards precision and automation, the TGA (thermogravimetric analyser) currently is most suitable for thermal measurement on small amounts and small size of the sample. Hence, there is a certain distortion of wood pellet thermal measurement due to the intense internal heat and mass transfer. The comparison between wood powder and pellet combustion kinetic parameters is shown in Table 5.

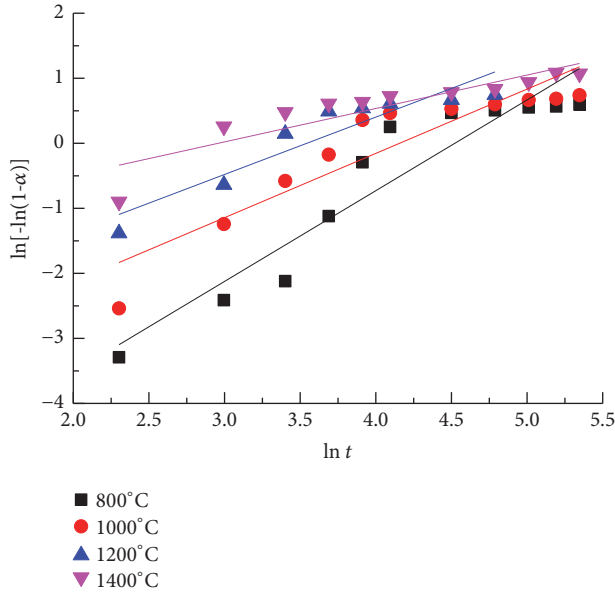
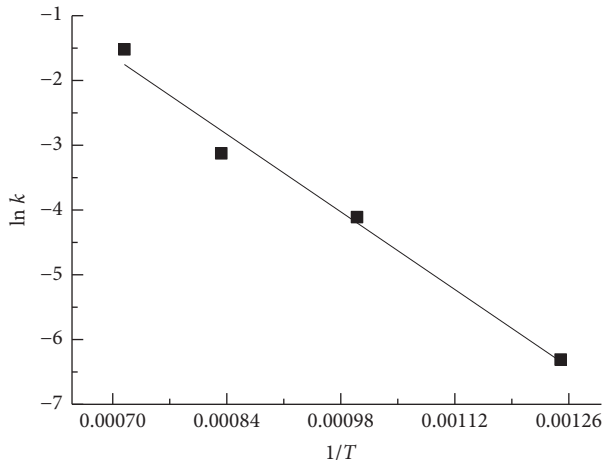
From Table 5, it is clear that the mechanism functions of wood powder and pellet are different. The discrepancies indicated that sample size, shape, amount, and heating rate could lead to the difference in combustion mechanism of the same kind of fuel [19]. For wood pellet, when $\alpha < 0.80$, the combustion process could be described by the mechanism function $G(\alpha) = [-\ln(1 - \alpha)]^{1/2}$, but when $\alpha \geq 0.80$, no function that had been selected could fit the corresponding combustion process, whereas for wood powder, there was no piecewise feature; the whole combustion process could

be described by the mechanism function $G(\alpha) = (1 - \alpha)^{-1}$. Referring to the proximate analysis result shown in Table 1, $\alpha = 0.80$ was the dividing point where volatile combustion transits to charcoal combustion, illustrating the fact that the complicated heat and mass transfer effects on combustion of the wood pellet were much greater than those on wood powder due to the complexity of internal structure. Therefore, origin pellet should be used as far as possible in the research targeting kinetic parameters determination.

The values of apparent activation energy E , characterizing the molecular activity of wood pellet and powder, were of the same order with the difference $21.13 \text{ kJ}\cdot\text{mol}^{-1}$, indicating the consistency of the two forms of materials. As for the characterization of combustible molecule and oxygen molecule collision frequency [26], the preexponential factor A values of the two materials differed greatly, with the latter being seven orders of magnitude higher than the former, showing

TABLE 5: Kinetic triplets of wood powder and pellet.

Material	A/s^{-1}	$E/kJ \cdot mol^{-1}$	Mechanism function $[G(\alpha)]$
Wood Powder	2.55×10^8	92.33	$(1 - \alpha)^{-1}$
Wood pellet	78.55	71.20	$[-\ln(1 - \alpha)]^{1/2} (\alpha < 0.80)$

FIGURE 5: The linear relationship of $\ln[-\ln(1-\alpha)]-\ln t$.FIGURE 6: The linear relationship of $\ln k-1/T$.

that the wood powder was much more probable to collide with O_2 than wood pellet in the combustion process. All the calculations were consistent with the apparent phenomenon. In engineering, the former was mainly applied to the layered combustion, and hence good ventilation should be ensured to make the fuel surface fully contacted with the fresh air [27, 28], while the latter was often used in suspension combustion; despite the relatively static state between the fuel and air [29], the fuel still showed good burnout performance for the high molecule collision frequency.

4. Conclusions

By the kinetic analysis and results comparison of the combustion process of wood powder and pellet of the same kind of wood, the following conclusions are drawn:

(1) For wood powder, the combustion mechanism of the whole combustion process was basically unchanged, and the most probable mechanism function had no obvious segmental characteristics; for wood pellet, there was a great discrepancy between volatile combustion stage and char combustion stage, respectively, described by different most probable mechanism functions.

(2) The activation energy E values were $92.33 \text{ kJ mol}^{-1}$ for wood powder and $71.20 \text{ kJ mol}^{-1}$ for wood pellet, respectively, with a difference less than 30%. The preexponential factor A value of the former ($2.55 \times 10^8 \text{ s}^{-1}$) was far greater than that of the latter (78.55 s^{-1}), by seven orders of magnitude.

(3) Currently, most of the TGA is only suitable for combustion kinetic analysis in wood powder with less sample quantity and small particle size; hence it is difficult to truly reveal the combustion kinetic characteristics of bulk granular biomass fuel. In academic researches and engineering applications for the granular fuel, the TGA that is suitable for bulk fuel should be adopted to reduce the experimental errors induced by the sample.

Data Availability

The datasets generated and analysed during this study are available in the FAIRsharing repository: <https://figshare.com/s/d51ecef2f1992ae0b7c3>.

Conflicts of Interest

The authors declare that there are no conflicts of interest regarding the publication of this paper.

Acknowledgments

The authors thank Shunchun Yao and Saihua Jiang for comments and insights leading to the development of this manuscript. The authors gratefully acknowledge support by South China University of Technology and Guangdong Institute of Special Equipment Inspection and Research, Shunde Branch. This work was supported by Administration of Quality and Technology Supervision of Guangdong Province Research Funds (Grant no. 2017PB08).

References

- [1] A. Omri and D. K. Nguyen, "On the determinants of renewable energy consumption: International evidence," *Energy*, vol. 72, pp. 554–560, 2014.

- [2] C. Cambero and T. Sowlati, "Assessment and optimization of forest biomass supply chains from economic, social and environmental perspectives – A review of literature," *Renewable & Sustainable Energy Reviews*, vol. 36, pp. 62–73, 2014.
- [3] J. Benedek, T. Sebestyén, and B. Bartók, "Evaluation of renewable energy sources in peripheral areas and renewable energy-based rural development," *Renewable & Sustainable Energy Reviews*, vol. 90, pp. 516–535, 2018.
- [4] M. Matúš, P. Križan, L. Šooš, and J. Beniák, "The effect of paper-making sludge as an additive to biomass pellets on the final quality of the fuel," *Fuel*, vol. 219, pp. 196–204, 2018.
- [5] Z. Liu, B. Fei, Z. Jiang, and X. Liu, "Combustion characteristics of bamboo-biochars," *Bioresource Technology*, vol. 167, pp. 94–99, 2014.
- [6] X. Deyan, "Analysis to situation and countermeasure industry of wood manufacture industry of our country," *Forestry Prospect and Design*, vol. no. 3, pp. 85–92, 2013.
- [7] F. Guo and Z. Zhong, "Co-combustion of anthracite coal and wood pellets: Thermodynamic analysis, combustion efficiency, pollutant emissions and ash slagging," *Environmental Pollution*, vol. 239, pp. 21–29, 2018.
- [8] L. J. R. Nunes, J. C. O. Matias, and J. P. S. Catalão, "Mixed biomass pellets for thermal energy production: A review of combustion models," *Applied Energy*, vol. 127, pp. 135–140, 2014.
- [9] S. Proskurina, E. Alakangas, J. Heinimö et al., "A survey analysis of the wood pellet industry in Finland: Future perspectives," *Energy*, vol. 118, pp. 692–704, 2017.
- [10] E. Trømborg, T. Ranta, J. Schweinle, B. Solberg, G. Skjevrak, and D. G. Tiffany, "Economic sustainability for wood pellets production - A comparative study between Finland, Germany, Norway, Sweden and the US," *Biomass and Bioenergy*, vol. 57, pp. 68–77, 2013.
- [11] R. Tauro, C. A. García, M. Skutsch, and O. Masera, "The potential for sustainable biomass pellets in Mexico: An analysis of energy potential, logistic costs and market demand," *Renewable & Sustainable Energy Reviews*, vol. 82, pp. 380–389, 2018.
- [12] P. Ge, L. Qiang, and X. Peng, "Thermogravimetric study on combustion and kinetic characteristics of artificial-plates," *Techniques and Equipment for Environmental Pollution Control*, vol. 6, pp. 2431–2436, 2012.
- [13] W. Cuiping, L. Ding kai, W. Fengyin et al., "Experimental study on the combustion characteristics of biomass pellets," *Transaction of the CSAE*, vol. 22, no. 10, pp. 174–177, 2006.
- [14] Q. Wang, W. Zhao, H. Liu, C. Jia, and H. Xu, "Reactivity and kinetic analysis of biomass during combustion," *Energy Procedia*, vol. 17, pp. 869–875, 2012.
- [15] Y. Haseli, J. A. van Oijen, and L. P. H. de Goeij, "A detailed one-dimensional model of combustion of a woody biomass particle," *Bioresource Technology*, vol. 102, no. 20, pp. 9772–9782, 2011.
- [16] X. Fang, L. Jia, and L. Yin, "A weighted average global process model based on two-stage kinetic scheme for biomass combustion," *Biomass & Bioenergy*, vol. 48, pp. 43–50, 2013.
- [17] W. Cao, J. Li, and L. Lue, "Study on the ignition behavior and kinetics of combustion of biomass," *Energy Procedia*, vol. 142, pp. 136–141, 2017.
- [18] A. I. Moreno, R. Font, and J. A. Conesa, "Combustion of furniture wood waste and solid wood: Kinetic study and evolution of pollutants," *Fuel*, vol. 192, pp. 169–177, 2017.
- [19] S. Y. Yorulmaz and A. T. Atimtay, "Investigation of combustion kinetics of treated and untreated waste wood samples with thermogravimetric analysis," *Fuel Processing Technology*, vol. 90, no. 7–8, pp. 939–946, 2009.
- [20] P. Jinxing, C. Guanyi, W. Deqin et al., "Kinetic and gaseous product analyses of wood pyrolysis," *Acta Energiæ Solaris Sinica*, vol. 32, no. 12, pp. 1719–1724, 2011.
- [21] B. Peters and J. Smuła-Ostaszewska, "Simultaneous prediction of potassium chloride and sulphur dioxide emissions during combustion of switchgrass," *Fuel*, vol. 96, pp. 29–42, 2012.
- [22] H. Rongzu, *Thermal Analysis Kinetic*, Science Press, Beijing, China, 2008.
- [23] R. López-Fonseca, I. Landa, U. Elizundia, M. A. Gutiérrez-Ortiz, and J. R. González-Velasco, "A kinetic study of the combustion of porous synthetic soot," *Chemical Engineering Journal*, vol. 129, no. 1–3, pp. 41–49, 2007.
- [24] H. Jiang, M. Bi, B. Li, B. Gan, and W. Gao, "Combustion behaviors and temperature characteristics in pulverized biomass dust explosions," *Journal of Renewable Energy*, vol. 122, pp. 45–54, 2018.
- [25] J. Li, M. C. Paul, P. L. Younger, I. Watson, M. Hossain, and S. Welch, "Prediction of high-temperature rapid combustion behaviour of woody biomass particles," *Fuel*, vol. 165, pp. 205–214, 2016.
- [26] Q. Wang, Y. Zhao, and Y. Zhang, "Shrinkage kinetics of large-sized briquettes during pyrolysis and its application in tamped coal cakes from large-scale chambers," *Fuel*, vol. 138, pp. 1–14, 2014.
- [27] M. Costa, N. Massarotti, V. Indrizzi, B. Rajh, C. Yin, and N. Samec, "Engineering bed models for solid fuel conversion process in grate-fired boilers," *Energy*, vol. 77, pp. 244–253, 2014.
- [28] N. Vorobiev, A. Becker, H. Kruggel-Emden, A. Panahi, Y. A. Levendis, and M. Schiemann, "Particle shape and Stefan flow effects on the burning rate of torrefied biomass," *Fuel*, vol. 210, pp. 107–120, 2017.
- [29] R. Hurt, J.-K. Sun, and M. Lunden, "A kinetic model of carbon burnout in pulverized coal combustion," *Combustion and Flame*, vol. 113, no. 1–2, pp. 181–197, 1998.

Research Article

Thermodynamic Analysis of Supercritical CO₂ Power Cycle with Fluidized Bed Coal Combustion

Chenchen Geng, Yingjuan Shao , Wenqi Zhong, and Xuejiao Liu

Key Laboratory of Energy Thermal Conversion and Control of Ministry of Education, School of Energy and Environment, Southeast University, Nanjing 210096, China

Correspondence should be addressed to Yingjuan Shao; yjshao@seu.edu.cn

Received 4 May 2018; Accepted 25 June 2018; Published 24 July 2018

Academic Editor: Xiaoke Ku

Copyright © 2018 Chenchen Geng et al. This is an open access article distributed under the Creative Commons Attribution License, which permits unrestricted use, distribution, and reproduction in any medium, provided the original work is properly cited.

Closed supercritical carbon dioxide (S-CO₂) Brayton cycle is a promising alternative to steam Rankine cycle due to higher cycle efficiency at equivalent turbine inlet conditions, which has been explored to apply to nuclear, solar power, waste heat recovery, and coal-fired power plant. This study establishes 300MW S-CO₂ power system based on modified recompression Brayton cycle integrated with coal-fired circulating fluidized bed (CFB) boiler. The influences of two stages split flow on system performance have been investigated in detail. In addition, thermodynamic analysis of critical operating parameters has been carried out, including terminal temperature difference, turbine inlet pressure/temperature, reheat stages, and parameters as well as compressor inlet pressure/temperature. The results show that rational distribution of split ratio to the recompressor (SR₁) achieves maximal cycle efficiency where heat capacities of both sides in the low temperature recuperator (LTR) realize an excellent matching. The optimal SR₁ decreases in the approximately linear proportion to high pressure turbine (HPT) inlet pressure due to gradually narrowing specific heat differences in the LTR. Secondary split ratio to the economizer of CFB boiler (SR₂) can recover moderate flue gas heat caused by narrow temperature range and improve boiler efficiency. Smaller terminal temperature difference corresponds to higher efficiency and brings about larger cost and pressure drops of the recuperators, which probably decrease efficiency conversely. Single reheat improves cycle efficiency by 1.5% under the condition of 600°C/600°C/25Mpa while efficiency improvement for double reheat is less obvious compared to steam Rankine cycle largely due to much lower pressure ratio. Reheat pressure and main compressor (MC) inlet pressure have corresponding optimal values. HPT and low pressure turbine (LPT) inlet temperature both have positive influences on system performance.

1. Introduction

High efficiency and clean coal-fired power generation technologies are priority research directions in the traditional energy industry. Utilizing double reheat and raising steam parameters are two effective means to improve power plant efficiency, however, which is generally restricted by nickel-based alloys development and expensive equipment cost. More efficient and compact cycles integrated with conventional coal-fired boiler become a breakthrough in improving fossil fuels utilization rate. Closed supercritical carbon dioxide (S-CO₂) Brayton cycle is considered as a promising substitute for steam Rankine cycle applied to thermal power generation. S-CO₂ is that both pressure and temperature of CO₂ are above its critical point (7.38Mpa 30.98°C) which is a suitable working fluid for power generation because of its near-critical

properties. CO₂ critical temperature is easily achieved and operating at high pressure allows more compact turbomachinery. Furthermore, S-CO₂ possesses high density in near-critical region similarity to its liquid phase resulting in less compressor work and higher efficiency. Besides, CO₂ is generally abundant, less corrosive, inexpensive, and nontoxic [1].

Previous researches show that S-CO₂ Brayton cycle is more efficient than supercritical steam Rankine cycle above moderate turbine inlet temperatures and can be coupled with various heat sources. The investigations of its potential applications have extended from nuclear, concentrated solar power (CSP), shipboard propulsion, waste heat recovery, and geothermal to fossil fuel [2, 3]. Detailed analysis began in the late 1960s. Feher [4] proposed CO₂ as the working fluid for the regenerative supercritical cycle that operated entirely above the critical pressure and was compressed in

the liquid phase. Hoffmann and Feher [5] further designed a 150 kWe power conversion module for a helium-cooled nuclear reactor in 1970. Angelino [6] analyzed different configurations of CO₂ condensing cycles including recompression cycle, partial cooling cycle, pre-expansion cycle, and pre-compression cycle. The study pointed out that the efficiency of recompression CO₂ cycle was better than reheat steam cycle at turbine inlet temperatures higher than 650°C. These studies have not been given sufficient attention in the following decades because of immature manufacturing technics as well as limitation of heat resource temperature. Dostal et al. [1] revived interest in S-CO₂ cycles in the early 20th century; they modified the recompression S-CO₂ cycle proposed by Angelino and carried out detailed component design, optimization, and economic analysis as well as control schemes for advanced nuclear reactors. After that, a growing number of studies were carried out involving system design [7], thermodynamic analysis and optimization [8, 9], and experimental loop tests [10, 11] as well as commercial-scale construction [12, 13] for different applications.

A considerable amount of heat recovered by recuperators from turbine exhaust brings about a narrow temperature range through the heat source. S-CO₂ cycle can well match with nuclear and CSP heat sources due to their nearly constant temperature [14]. However, modifications are indispensable for applications to the coal-fired power plant in order to effectively utilize flue gas heat and improve the gross plant efficiency. Several improvements have been put forward, such as utilizing residual heat to preheat air, improving cycle layouts, extracting a fraction of S-CO₂ from different points at high-pressure side to recover flue gas heat, heating recycled flue gas, and adopting cascaded or combined cycles. Muto et al. [15] proposed a double expansion turbine cycle to reduce the pressure difference between gas side and S-CO₂ side of heater and introduced an economizer to recover exit gas heat. Moullec [16] explored the potential performance of a coal-fired power plant based on double reheat recompression S-CO₂ cycle integrated with a post-combustion carbon capture and storage (CCS). A high temperature air preheating combined with a fraction of fluid split from the main compressor (MC) to the economizer can effectively utilize 100~500°C flue gas heat. The net lower heating value (LHV) plant efficiency without CO₂ capture for a maximal temperature and pressure of 620°C and 30Mpa could achieve 50.3% and 4.8% higher than supercritical steam power plant. Mecheri and Moullec [17] investigated the S-CO₂ system performance and still recommended the previous layout. Li et al. [18] set up an additional split flow economizer before the air preheater to heat the CO₂ from low temperature recuperator (LTR) and had accomplished 5MWe fossil-based S-CO₂ recompression and reheat integral test facility design. Bai et al. [19] provided a novel S-CO₂ intercooled recompression cycle with additional medium-temperature recuperator and an anabranch applied to a coal-fired power plant, which could achieve 49.5% net LHV efficiency with 29.6Mpa/650°C. Shelton et al. [20] constructed S-CO₂ recompression cycle with an oxy-coal circulating fluidized bed (CFB) and CCS, which could realize a nearly constant temperature heat source through heating the recycled flue gas and a fraction of CO₂ from the MC exit.

The efficiency increment of the S-CO₂ cycle plant configured with reheat and intercooling could achieve 2% compared to steam Rankine cycle power. Pratt and Whitney Rocketdyne [21] developed Zero Emission Power and Steam (ZEPS) plant which adopted a pressurized fluidized bed combustor (PFBC) with combined cycle that modified S-CO₂ cycle was used as the topping cycle and steam cycle was used as the bottoming cycle. The ZEPS plant efficiency could increase by 9.4% compared with oxy-combustion atmospheric boiler. Thimsen et al. [22] designed an inverted tower coal-fired S-CO₂ heater that applied to a 750MWe recompression S-CO₂ power cycle with 700°C turbine inlet temperature. A second cascading S-CO₂ cycle was employed as the bottoming cycle to cool the combustion products from 530°C to 370°C.

CFB boiler with relatively uniform, low heat flux and combustion temperature, and wide fuel flexibility as well as low pollutant emissions can be better coupled with S-CO₂ cycle compared to pulverized coal (PC) boiler [14, 23]. Combination of CFB boiler and S-CO₂ power cycle is one of the effective means for the coal-dominated energy structure in China to improve energy conversion efficiency and reduce pollutant emissions at their source. The gross system performance requires further analysis and optimization. This study establishes 300MW coal-fired power system based on recompression S-CO₂ cycle and single reheat integrated with CFB boiler. Secondary split flow extracted from high-pressure side of the cycle is adopted to accommodate narrow temperature variation through the boiler caused by the necessarily high extent of recuperated heat. A series of parameters sensitivity analysis have been carried out, including two stages split ratio, terminal temperature difference, turbine inlet pressure/temperature, and reheat pressure/temperature as well as compressor inlet pressure/temperature.

2. System Configuration and Model

2.1. System Configuration. The overall system layout based on modified recompression S-CO₂ cycle and single reheat integrated with CFB boiler and the corresponding T-s diagram are shown in Figures 1 and 2. Several different configurations have been put forward, including simple recuperated cycle, recompression cycle, partial cooling cycle, and pre-expansion cycle. However, recompression cycle is considered as a promising alternative with high performance and simple compositions [1]. The recompression cycle effectively alleviates pinch-point problem through adjusting flow rate to compensate specific heat difference and better match temperature variation between cold and hot side fluid in the LTR. Besides, single reheat, a common method used in steam Rankine cycle, can further increase plant efficiency. An additional high pressure CO₂ split flow extracted from LTR outlet to the economizer (ECO) can not only utilize flue gas heat but also increase high temperature recuperator (HTR) effectiveness, which is a valid method employed by aforementioned studies.

As Figure 1 shows, there exist two split flow locations in the system. Firstly, a portion of S-CO₂ exiting from LTR hot side is cooled in the precoolers (PC), compressed by the MC and preheated in the LTR sequentially. The remaining flow

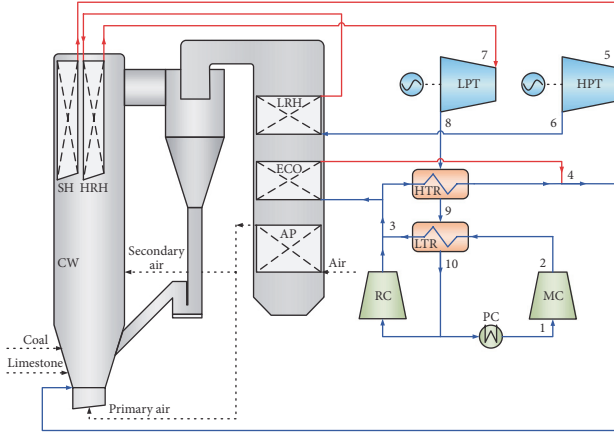


FIGURE 1: Schematic diagram of recompression S-CO₂ cycle with single reheat.

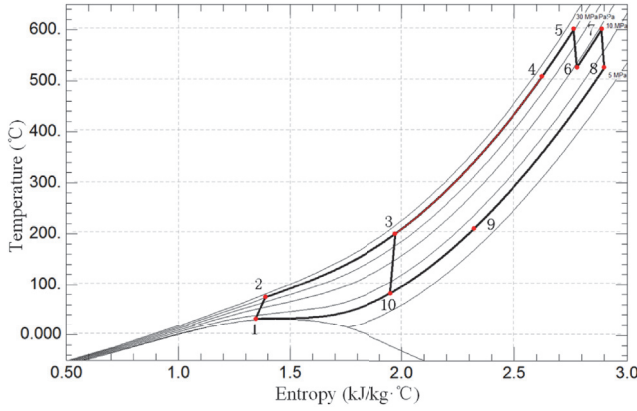


FIGURE 2: T-s diagram of recompression S-CO₂ Brayton cycle with single reheat.

is directly compressed by the recompressor (RC) and mixes with outlet fluid of LTR cold side. The mixture is divided into two branches again. One branch of S-CO₂ exiting from LTR cold side is diverted into the ECO to recover relatively high temperature flue gas heat and another branch is further preheated in the HTR. Two branches of fluid finally converge and are further heated to the desired temperature through the cooling wall (CW) and superheater (SH) of the CFB boiler sequentially. S-CO₂ with high pressure and temperature expands through the high pressure turbine (HPT) and is reheated in the low temperature reheater (LRH) and the high temperature reheater (HRH). S-CO₂ with moderate pressure expands through the low pressure turbine (LPT) and then passes through the HTR, LTR, and PC to the lowest temperature and pressure.

2.2. Mathematical Model. The thermodynamic model for the S-CO₂ power system has been established based on mass and energy balance. S-CO₂ properties are inquired from REFPROP database, which is developed by the National Institute of Standards and Technology (NIST) [24] based on Span and Wagner equation of state [25]. Thermal parameters

of different states in the system are calculated through iteration. In addition, CFB boiler heat balance and efficiency are obtained by preliminary thermal calculation [26].

Several assumptions need to be considered in this study:

- (1) The system operates under steady-state conditions.
- (2) Heat losses in pipelines and each component are neglected.
- (3) The temperature and pressure of mixing flows as well as respective branch flows are set to the identical value in order to reduce irreversible loss. The outlet states of LTR cold side and RC are equal. Similarly, the outlet states of HTR cold side and ECO are same.
- (4) Pressure drops in each component are assumed to be constant with the minimum and maximum pressure variations. The CFB boiler and PC pressure drops are set to 0.7Mpa and 0.05Mpa, respectively. The cold side and hot side pressure drops of LTR and HTR are set to 0.15Mpa and 0.1Mpa separately.

Two concepts of the split ratio are defined. The first split ratio (SR_1) is defined as the ratio of RC mass flow to the total mass flow and the second split ratio (SR_2) is defined as the ratio of ECO mass flow to the total mass flow, both of which are given by

$$SR_1 = 1 - \frac{(h_9 - h_{10})}{(h_3 - h_2)} \quad (1)$$

$$SR_2 = 1 - \frac{(h_8 - h_9)}{(h_4 - h_3)} \quad (2)$$

The compression and expansion in the MC, RC, HPT, and LPT are non-isentropic process. Work consumption of MC and RC and work output of HPT and LPT are expressed as

$$W_{MC} = m(1 - SR_1) \cdot \frac{(h_{2s} - h_1)}{\eta_{MC}} \quad (3)$$

$$= m(1 - SR_1) \cdot (h_2 - h_1)$$

$$W_{RC} = \frac{m \cdot SR_1 (h_{3s} - h_{10})}{\eta_{RC}} = m \cdot SR_1 (h_3 - h_{10}) \quad (4)$$

$$W_{HPT} = m \cdot (h_5 - h_{6s}) \cdot \eta_{HPT} = m \cdot (h_5 - h_6) \quad (5)$$

$$W_{LPT} = m \cdot (h_7 - h_{8s}) \cdot \eta_{LPT} = m \cdot (h_7 - h_8) \quad (6)$$

The temperature difference and effectiveness are frequently used for recuperator model. However, the terminal temperature difference, defined as the achievable minimum temperature at the end of recuperators, is a preference for calculation [27]. The terminal temperature differences of LTR and HTR are set to 8°C, which is a reasonably accomplishable value for current technical equipment. The smaller terminal temperature difference can improve heat transfer capacity, but cause the nonlinear increase of recuperator volumes and capital costs. The temperature relations in the LTR and HTR are defined as

$$t_2 + \Delta t \leq t_{10} \leq t_9 \quad (7)$$

$$t_3 + \Delta t \leq t_9 \leq t_8 \quad (8)$$

The energy balance equations for the LTR and HTR are expressed as

$$Q_{LTR} = m(1 - SR_1) \cdot (h_3 - h_2) = m \cdot (h_9 - h_{10}) \quad (9)$$

$$Q_{HTR} = m(1 - SR_2) \cdot (h_4 - h_3) = m \cdot (h_8 - h_9) \quad (10)$$

Heat absorption in the CFB is expressed as

$$Q_{CFB} = m[SR_2 \cdot (h_5 - h_3) + (1 - SR_2) \cdot (h_5 - h_4) + (h_7 - h_6)] \quad (11)$$

Heat rejection in the PC is expressed as

$$Q_{PC} = m(1 - SR_1) \cdot (h_{10} - h_1) \quad (12)$$

Thermal efficiency and net efficiency are defined as

$$\eta_{th} = \frac{(W_{LPT} + W_{HPT} - W_{MC} - W_{RC})}{Q_{CFB}} \cdot 100\% \quad (13)$$

$$\eta_{net} = \frac{(W_{LPT} + W_{HPT} - W_{MC} - W_{RC}) \cdot \eta_G \cdot 100\%}{(m_{coal} \cdot Q_{net,ar})} \quad (14)$$

$$= \eta_{th} \cdot \eta_G \cdot \eta_{CFB}$$

Initial parameters of recompression S-CO₂ cycle with CFB, specific compositions of coal, and desulfurizer are listed in Tables 1 and 2.

2.3. Validation of Thermodynamic Model. The thermodynamic model is validated by literature data [9]. MC inlet pressure of 7.38Mpa and compressor isentropic efficiency of 89% are selected. Other input parameters are identical to Table 1. As Figure 3 shows, the relative errors are below 3%, which are primarily caused by recuperator model. Terminal temperature difference of 8°C corresponds to nearly 95% effectiveness of LTR; however effectiveness of HTR is higher than 95%, leading to larger thermal efficiency.

3. Results and Discussion

The influences of critical operating parameters on system performance have been investigated comprehensively based on cycle thermodynamics model and CFB thermal balance.

3.1. Split Ratio to the RC (SR_1). Figure 4 presents effects of SR_1 on cycle efficiency at different terminal temperature differences. SR_1 is a key manipulated variable influencing the thermal efficiency of the S-CO₂ cycle, which has optimal values under given working conditions. Specific heat of S-CO₂ varies dramatically with the pressure and temperature, especially near the critical point, and therefore the terminal temperature difference will appear at the cold or hot end of the LTR as SR_1 changes. At first, with the increase of SR_1 , less amount of S-CO₂ passes through the PC and MC, resulting in work consumption decrease in the MC and increase in the RC; accordingly, the total work consumption increases. In addition, the outlet temperature of the cold side

TABLE 1: Initial parameters.

Parameter	Symbol	Unit	Value
Electric power output	W_e	WM	300
MC inlet pressure	P_1	Mpa	7.6
MC inlet temperature	t_1	°C	32
HPT inlet pressure	P_5	Mpa	25
HPT inlet temperature	t_5	°C	600
LPT inlet pressure	P_7	Mpa	14
LPT inlet temperature	t_7	°C	600
Terminal temperature difference	Δt	°C	8
MC and RC isentropic efficiency	η_{MC}, η_{RC}	%	90[16]
HPT and LPT isentropic efficiency	η_{HPT}, η_{LPT}	%	93[16]
Generator efficiency	η_G	%	98.5
Exhaust temperature	t_{py}	°C	110
Environment temperature	t_0	°C	20

TABLE 2: Compositions of coal and desulfurizer.

Coal and desulfurizer	Compositions	Unit	Value
Ultimate analysis of bituminous coal (As-received)	Carbon	%	62.96
	Hydrogen	%	4.13
	Oxygen	%	6.73
	Nitrogen	%	1.46
	Sulfur	%	1.22
	Moisture	%	10.00
	Ash	%	13.50
Heat value (LHV)	$Q_{net,ar}$	MJ/kg	24.72
Limestone	Calcium carbonate	%	95
	Moisture	%	0.2
	Impurities	%	4.8

fluid in HTR continues to rise, leading to a reduction in boiler heat absorption. The extent of decrease of boiler heat absorption is greater than the increase of compressor work consumption, which constantly improves the cycle efficiency until LTR reaches the temperature difference restriction at the hot end. In such a condition, the minimum temperature differences are achieved at both ends of LTR. LTR realizes an excellent temperature matching in which the negative impact of specific heat difference falls to zero and thermal efficiency reaches the maximum. Then, continuing to raise SR_1 leads to the sharp decline of LTR effectiveness and thermal efficiency as a result. The later analyses are based on optimal SR_1 values under different operating conditions.

Figure 4 also indicates impacts of different terminal temperature differences on thermal efficiency. The terminal temperature difference represents recuperators heat transfer capability, smaller temperature difference gets better heat transfer capacity and higher cycle efficiency, but it will need greater volumes and higher cost. In addition, larger heat transfer areas increase pressure drops in recuperators, which decrease efficiency conversely. The relevant study indicates that minimum temperature difference lower than 4°C is not economical [28].

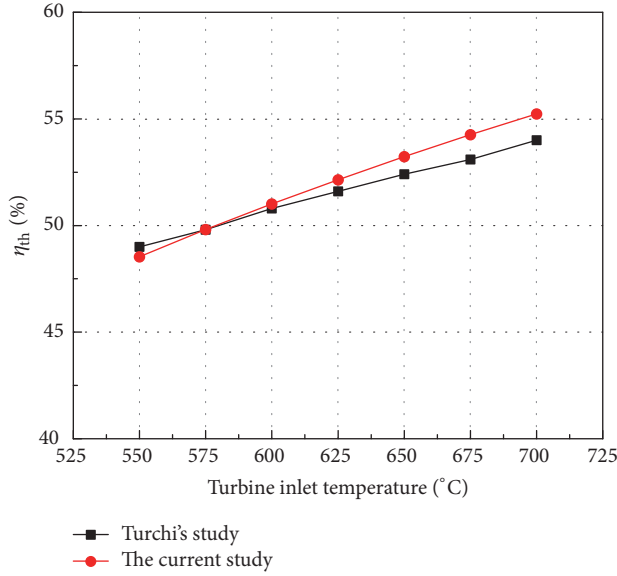


FIGURE 3: Validation of thermodynamic model by Turchi's study.

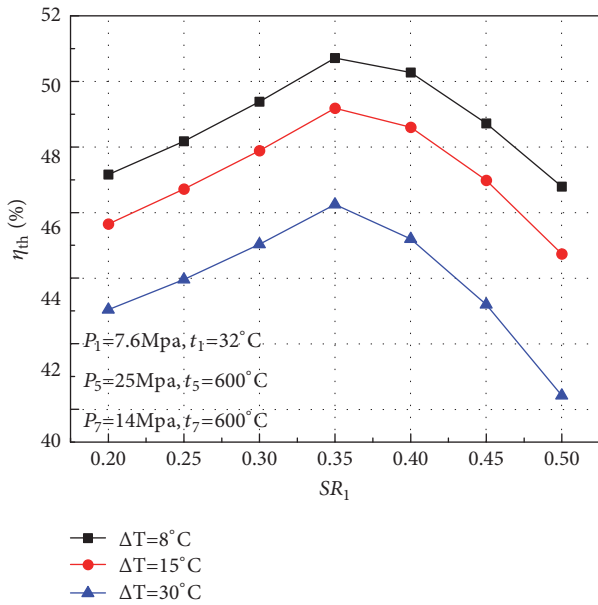
FIGURE 4: Effects of SR_1 on cycle efficiency at different terminal temperature differences.

Figure 5 illustrates effects of HPT inlet pressure on optimal SR_1 . The optimal SR_1 declines in the approximately linear proportion to HPT inlet pressure. The same mass flow in recuperator of simple recuperated cycle causes larger heat addition while bypassing the LTR of recompression cycle leads to higher average heat absorption temperature and thermal efficiency improvement. As Figure 5 presents, average specific heat differences between high-pressure and low-pressure side fluids are gradually narrowing with increasing HPT inlet pressure and a greater proportion of S-CO₂ is permitted to access to the PC and MC; thereby optimal values of SR_1 decrease.

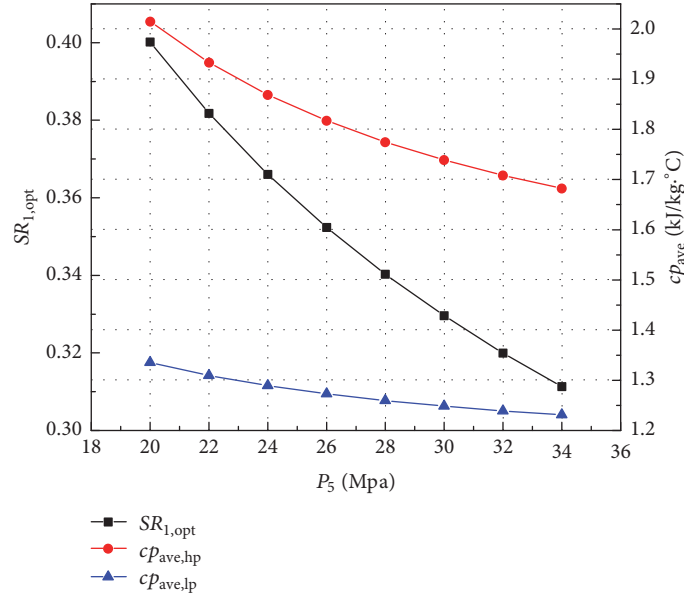
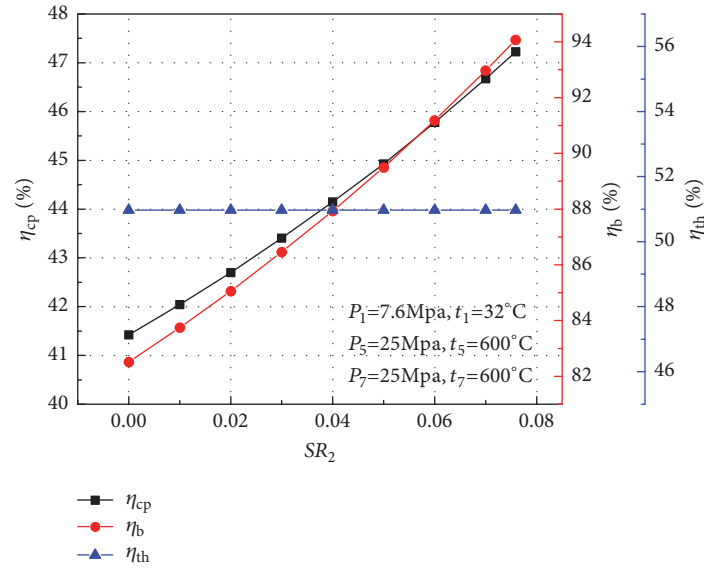
3.2. Split Ratio to the ECO (SR_2). Figure 6 shows effects of SR_2 on boiler efficiency, thermal efficiency, and net efficiency. It demonstrates that the split flow exiting from high-pressure side of the LTR can effectively recover moderate flue gas heat and improve boiler efficiency. Simultaneously, cycle thermal efficiency maintains constant and net efficiency increases accordingly. Boiler heat losses and corresponding efficiency are preliminarily calculated according to semiempirical formulas and historical operation data of steam CFB boiler. Suppose the minimum temperature approach of countercurrent LRH located above the ECO is 55°C and hot air is preheated to 300°C, exhaust gas temperature gradually decreases and boiler efficiency rises with the increase of SR_2 . Furthermore, thermal efficiency maintains constant because heat recovered by the HTR does not change with a low proportion of S-CO₂ entering into the ECO. When SR_2 is equal to 0.076, the exhaust temperature falls to 110°C, and thus boiler efficiency is improved to 94%; the net efficiency can reach about 47.2%.

3.3. HPT Inlet Parameters. Figure 7 shows effects of HPT inlet pressure on cycle efficiency at different HPT inlet temperature. The cycle efficiency is improved with the increase of HPT inlet pressure, but the rate of increase gradually slows down and eventually reaches a stable state. At first, the increment of specific work output of the HPT is greater than total specific work consumption of the MC and RC as HPT inlet pressure increases, 1Mpa increase in HPT inlet pressure leads to about 0.5% improvement in cycle efficiency. The increment rate of specific net work continues to fall with HPT inlet pressure rising. In these conditions, the benefit of efficiency improvement is less obvious and materials pressure-resistance requirement becomes stricter, leading to larger material cost.

It can also be observed from Figure 7 that HPT inlet temperature has a positive influence on system performance. The degree of efficiency improvement caused by HPT inlet temperature is more noticeable under higher HPT inlet pressure. The cycle efficiency is improved by nearly 0.35% with HPT inlet temperature increasing by 20°C under HPT inlet pressure of 20Mpa. The cycle efficiency is improved by nearly 0.6% with HPT inlet pressure of 35Mpa under the same HPT temperature interval.

3.4. Reheat Stages and Parameters. Reheat is an effective approach for steam Rankine cycle efficiency improvement by increasing average heat absorption temperature. However, S-CO₂ Brayton cycle with lower pressure ratio has different results. As Figure 8 presents, single reheat can improve cycle efficiency, especially under higher HPT inlet pressure. The thermal efficiency is improved by 1.5% with HPT inlet pressure of 25Mpa. However, the efficiency of double reheat is enhanced by only 0.2% under the same condition. Larger reheat stages are undesirable due to more complex configurations and additional capital cost, which may offset the benefit of efficiency increment.

Figures 9 and 10 show effects of LPT inlet pressure on cycle efficiency at different HPT inlet pressure and LPT inlet temperature. As these figures reveal, LPT inlet pressure has optimal values corresponding to different HPT inlet pressure

FIGURE 5: Effects of HPT inlet pressure on optimal SR_1 .FIGURE 6: Effects of SR_2 on boiler efficiency, thermal efficiency, and net efficiency.

and LPT inlet temperature. Firstly, the tendency of the change of HPT work output is opposite to the variation of LPT work output with increasing reheat pressure. HPT work output decreases and conversely LPT work output increases, which has an optimal reheating pressure. The corresponding optimal reheat pressures with different HPT inlet pressure of 20Mpa, 25Mpa, and 30Mpa are 13Mpa, 14.5Mpa, and 16Mpa respectively, which are slightly higher than the average of minimum and maximum pressures (12.6Mpa, 14.1Mpa, and 15.5Mpa). Figure 10 indicates that the efficiency is improved by nearly 0.5% with the reheat temperature increment of 20°C. Moreover, optimal reheat pressures are similarly affected by reheat temperature. Higher reheat temperature

corresponds to larger reheat pressure. Pressure ratios between HPT and LPT need to be redistributed due to various work output under different reheat temperature.

Figure 11 summarizes optimal reheat pressure values under different HPT inlet pressure and LPT inlet temperature, which can be used as a reference for the conceptual design of a power plant. These values are still affected by the pressure drop in reheater and detailed hydraulic calculation needs to be further carried out.

3.5. MC Inlet Parameters. Figure 12 shows effects of MC inlet pressure on cycle efficiency at different MC inlet temperature. MC inlet pressure similarity has optimal values,

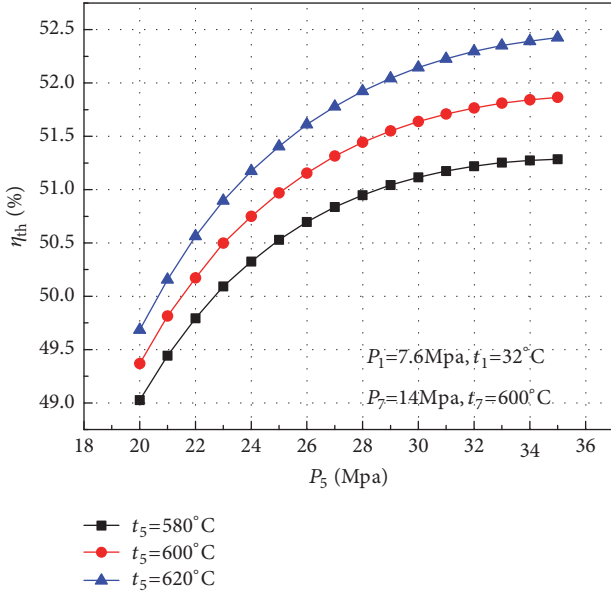


FIGURE 7: Effects of HPT inlet pressure on cycle efficiency at different HPT inlet temperature.

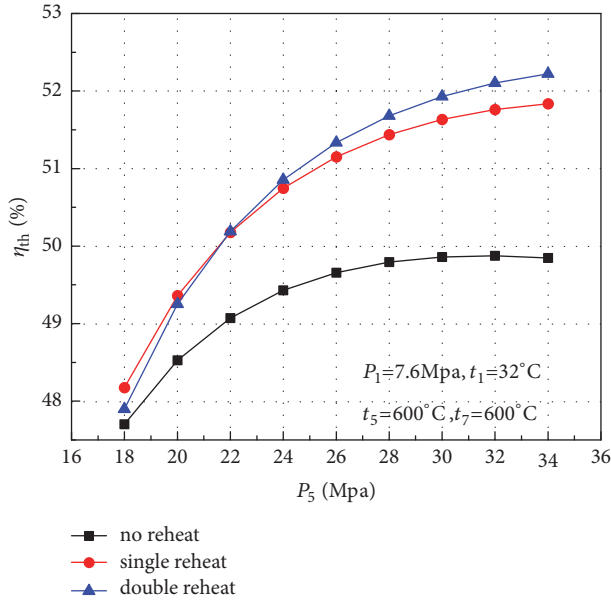


FIGURE 8: Effects of reheat stages on cycle efficiency at different HPT inlet pressure.

which correspond to the pseudocritical pressure of various MC inlet temperature. In addition, optimal MC inlet pressure increases and maximum cycle efficiency decreases with different MC inlet temperature. The specific reason is that turbine work output and compressor work consumption together decrease with increasing MC inlet pressure at first, but work consumption variation, especially in the MC, is greater due to the sharp decline of compressibility factor in the near-critical region, showing the incompressibility property of liquid phase, finally leading to continual rising of

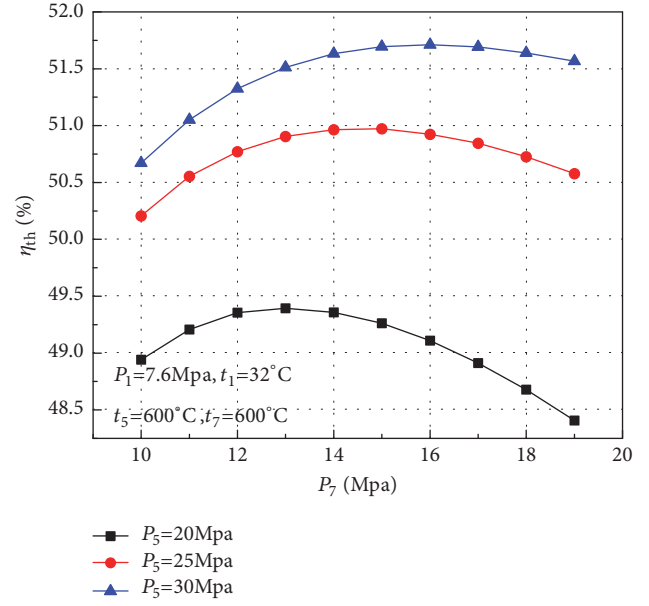


FIGURE 9: Effects of LPT inlet pressure on cycle efficiency at different HPT inlet pressure.

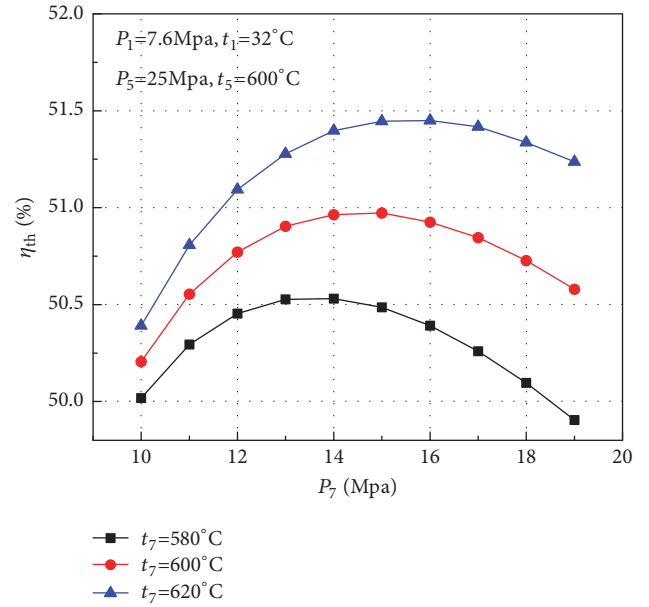


FIGURE 10: Effects of LPT inlet pressure on cycle efficiency at different LPT inlet temperature.

cycle efficiency. The benefit of lower compression work consumption near critical point gradually decreases with further increasing MC inlet pressure and temperature. Moreover, the total compressor work consumption increases with MC inlet temperature, resulting in a significant decrease of thermal efficiency especially under optimal MC inlet pressure.

4. Conclusions

S-CO₂ recompression Brayton cycle is a promising alternative to be applied in coal-fired power generation due to special

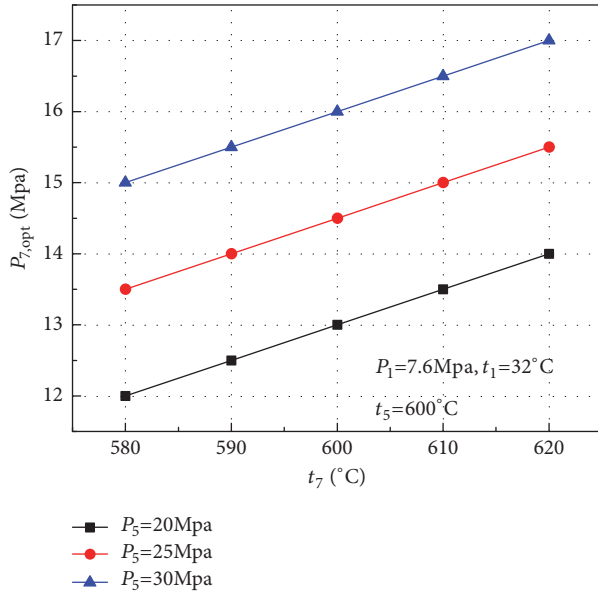


FIGURE 11: Optimal reheat pressure under different HPT inlet pressure and LPT inlet temperature.

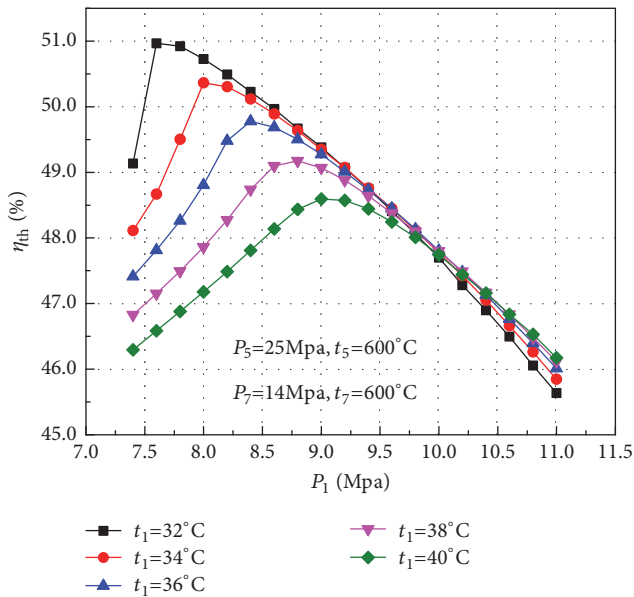


FIGURE 12: Effects of MC inlet pressure on cycle efficiency at different MC inlet temperature.

thermophysical properties in the near-critical region and high average heat absorption temperature as well as low pressure ratio, which contribute to higher efficiency and more compact turbomachinery compared to steam Rankine cycle.

CFB boiler with lower and uniform combustion temperature can be better integrated with S-CO₂ cycle. However, the overall system configuration needs to be further modified to match the narrow temperature range of heat source. This paper constructs recompression S-CO₂ Brayton cycle with single reheat based on the CFB boiler. Additional split flow extracted from LTR cold side is adopted in order to utilize flue

gas heat effectively. The net efficiency can reach 47.2% under the condition of 600°C/600°C/25Mpa.

Influences of critical parameters on system performance have been investigated systematically, including RC split ratio (SR₁), ECO split ratio (SR₂), HPT inlet pressure and temperature, and reheat layout as well as MC inlet pressure and temperature. The results show that SR₁, reheat pressure, and MC inlet pressure have optimal values, among which appropriate temperature matching is achieved between the hot and cold side of the LTR, the optimal reheat pressure is slightly higher than the average pressure and is still affected by reheat temperature, and the optimal MC inlet pressure corresponds to pseudocritical pressure of various MC inlet temperature. Smaller terminal temperature difference corresponds to higher efficiency, but the cost and pressure drops of heat exchangers need to be taken into account. Reasonable SR₂ can recover moderate flue gas heat caused by narrow temperature range. Single reheat improves cycle efficiency by 1.5% with HPT inlet pressure of 25Mpa; however, double reheat for efficiency improvement is less obvious compared to steam Rankine cycle largely due to much lower pressure ratio. In addition, HPT and LPT inlet temperature both have positive influences on system performance. The cycle efficiency is improved by nearly 0.5% with HPT or LPT inlet temperature increasing by 20°C under HPT inlet pressure of 25Mpa.

Abbreviations

S-CO ₂ :	Supercritical carbon dioxide
CSP:	Concentrated solar power
CFB:	Circulating fluidized bed
PFBC:	Pressurized fluidized bed combustor
PC:	Pulverized coal
CCS:	Carbon capture and storage
LHV:	Lower heating value
ZEPS:	Zero Emission Power and Steam
NIST:	National Institute of Standards and Technology
SR ₁ :	Split ratio to the recompressor
SR ₂ :	Split ratio to the economizer
LTR:	Low temperature recuperator
HTR:	High temperature recuperator
LPT:	Low pressure turbine
HPT:	High pressure turbine
MC:	Main compressor
RC:	Recompressor
PC:	Precooler
ECO:	Economizer
CW:	Cooling wall
SH:	Superheater
LRH:	Low temperature reheater
HRH:	High temperature reheater
AP:	Air preheater.

Data Availability

The data used to support the findings of this study are available from the corresponding author upon request.

Conflicts of Interest

The authors declare that there are no conflicts of interest regarding the publication of this paper.

Acknowledgments

Financial supports from the National Key Research and Development Program of China (no. 2017YFB0601802) and Key Research and Development Program of Jiangsu Province (no. BE2017159) are sincerely acknowledged.

References

- [1] V. Dostal, *A Supercritical Carbon Dioxide Cycle for Next Generation Nuclear Reactors*, Massachusetts Institute of Technology, Massachusetts, Mass, USA, 2004.
- [2] Y. Ahn, S. J. Bae, M. Kim et al., "Review of supercritical CO₂ power cycle technology and current status of research and development," *Nuclear Engineering and Technology*, vol. 47, no. 6, pp. 647–661, 2015.
- [3] M.-J. Li, H.-H. Zhu, J.-Q. Guo, K. Wang, and W.-Q. Tao, "The development technology and applications of supercritical CO₂ power cycle in nuclear energy, solar energy and other energy industries," *Applied Thermal Engineering*, vol. 126, pp. 255–275, 2017.
- [4] E. G. Feher, "The supercritical thermodynamic power cycle," *Energy Conversion*, vol. 8, no. 2, pp. 85–90, 1968.
- [5] J. R. Hoffmann and E. G. Feher, "150 kwe supercritical closed cycle system," *Journal of Engineering for Gas Turbines and Power*, vol. 93, no. 1, pp. 70–80, 1971.
- [6] G. Angelino, "Carbon dioxide condensation cycles for power production," *Journal of Engineering for Gas Turbines and Power*, vol. 90, no. 3, pp. 287–295, 1968.
- [7] F. Crespi, G. Gavagnin, D. Sánchez, and G. S. Martínez, "Supercritical carbon dioxide cycles for power generation: a review," *Applied Energy*, vol. 195, pp. 152–183, 2017.
- [8] J. Sarkar, "Second law analysis of supercritical CO₂ recompression Brayton cycle," *Energy*, vol. 34, no. 9, pp. 1172–1178, 2009.
- [9] C. S. Turchi, Z. Ma, T. W. Neises, and M. J. Wagner, "Thermodynamic study of advanced supercritical carbon dioxide power cycles for concentrating solar power systems," *Journal of Solar Energy Engineering*, vol. 135, no. 4, article 41007, 2013.
- [10] S. A. Wright, R. F. Radel, M. E. Vernon, P. S. Pickard, and G. E. Rochau, *Operation and Analysis of a Supercritical CO₂ Brayton Cycle*, Sandia, New Jersey, NJ, USA, 2010.
- [11] B. D. Iverson, T. M. Conboy, J. J. Pasch, and A. M. Kruienza, "Supercritical CO₂ Brayton cycles for solar-thermal energy," *Applied Energy*, vol. 111, pp. 957–970, 2013.
- [12] T. J. Held, "Initial test results of a megawatt-class supercritical CO₂ heat engine," in *Proceedings of the 4th International Symposium on Supercritical CO₂ Power Cycles*, 2014.
- [13] C. Turchi, *10 MW Supercritical CO₂ Turbine Test*, National Renewable Energy Laboratory, 2014.
- [14] K. Brun, P. Friedman, and R. Dennis, *Fundamentals and Applications of Supercritical Carbon Dioxide (SCO₂) Based Power Cycles*, Woodhead Publishing, Cambridge, UK, 2017.
- [15] Y. Muto, S. Ishiyama, Y. Kato, T. Ishizuka, and M. Aritomi, "Application of supercritical CO₂ gas turbine for the fossil fired thermal plant," *Journal of Energy and Power Engineering*, vol. 9, pp. 7–15, 2010.
- [16] Y. Le Moullec, "Conceptual study of a high efficiency coal-fired power plant with CO₂ capture using a supercritical CO₂ Brayton cycle," *Energy*, vol. 49, no. 1, pp. 32–46, 2013.
- [17] M. Mecheri and Y. Le Moullec, "Supercritical CO₂ Brayton cycles for coal-fired power plants," *Energy*, vol. 103, pp. 758–771, 2016.
- [18] H. Li, Y. Zhang, and M. Yao, "Preliminary design study on a multi-megawatts fossil-based supercritical CO₂ recompression and reheat integral test facility," in *Proceedings of the 5th International Symposium on Supercritical CO₂ Power Cycles*, 2016.
- [19] Z. Bai, G. Zhang, Y. Li, G. Xu, and Y. Yang, "A supercritical CO₂ Brayton cycle with a bleeding anabranch used in coal-fired power plants," *Energy*, 2017.
- [20] W. W. Shelton and N. Weiland, "Oxy-coal-fired circulating fluid bed combustion with a commercial utility-size supercritical CO₂ power cycle," in *Proceedings of the 5th International Symposium on Supercritical CO₂ Power Cycles*, 2016.
- [21] G. A. Johnson, M. W. McDowell, G. M. O'Connor, C. G. Sonwane, and G. Subbaraman, "Supercritical CO₂ Cycle development at Pratt and Whitney Rocketdyne," in *Proceedings of the ASME Turbo Expo 2012: Turbine Technical Conference and Exposition*, 2012.
- [22] D. Thimsen and P. Weitzel, "Challenges in designing fuel-fired sCO₂ heaters for closed sCO₂ Brayton cycle power plants," in *Proceedings of the 5th International Symposium on Supercritical CO₂ Power Cycles*, 2016.
- [23] P. Basu, *Circulating Fluidized Bed Boilers: Design, Operation and Maintenance*, Springer, Berlin, Germany, 2015.
- [24] E. W. Lemmon, M. L. Huber, and M. O. McLinden, NIST Standard Reference Database 23: Reference Fluid Thermodynamic and Transport Properties-REFPROP. 9.0, 2010.
- [25] R. Span and W. Wagner, "A new equation of state for carbon dioxide covering the fluid region from the triple-point temperature to 1100 K at pressures up to 800 MPa," *Journal of Physical and Chemical Reference Data*, vol. 25, no. 6, pp. 1509–1596, 1996.
- [26] X. Sun and Z. Huang, *Technology and Engineering Application of Large Circulating Fluidized Bed Boiler*, China Electric Power Press, Beijing, China, 2013.
- [27] J. C. Bryant, H. Saari, and K. Zanganeh, "An analysis and comparison of the simple and recompression supercritical CO₂ cycles," in *Proceedings of the Supercritical CO₂ Power Cycle Symposium*, 2011.
- [28] R. Dennis, "Overview of supercritical carbon dioxide based power cycles for stationary power generation," in *Proceedings of the 4th International Seminar on ORC Power Systems*, 2017.

Research Article

Investigation of the Thermal Improvement and the Kinetic Analysis of the Enriched Coal

Selma Duzyol ¹ and Cem Sensogut²

¹Department of Mining Engineering, Selcuk University, 42075 Konya, Turkey

²Department of Mining Engineering, Dumlupinar University, 43100 Kutahya, Turkey

Correspondence should be addressed to Selma Duzyol; selmad@selcuk.edu.tr

Received 12 January 2018; Revised 17 April 2018; Accepted 2 May 2018; Published 19 June 2018

Academic Editor: Kun Luo

Copyright © 2018 Selma Duzyol and Cem Sensogut. This is an open access article distributed under the Creative Commons Attribution License, which permits unrestricted use, distribution, and reproduction in any medium, provided the original work is properly cited.

The present research work is comprised of three main parts. The first part is about the enrichment of lignite coal by the utilization of dense medium separation called float and sink method. The second part deals with the investigation of the thermal behaviour for the coals enriched while the last part is concerned with the kinetic analysis of the coal combustion. The float and sink method is the mostly used technique for low-rank coal beneficiation in coal preparation plants of Turkey. In order to realize this process, the coal samples were, at first, fractioned to five different sizes which were -32+25 mm, -25+16 mm, -16+8 mm, -8+4.75 mm, and -4.75+2 mm. Each fraction was, then, processed in the dense mediums with the specific gravities of 1.20, 1.30, 1.40, 1.50, and 1.60 g/cm³, respectively. The thermal behaviour of the floated materials from the float and sink process was investigated in detail with the thermogravimetric analysis (TG) and the differential thermogravimetric analysis (DTG). The ignition and peak temperatures for the samples were also ascertained and correlated with the float and sink test results. In the final part of the study, the kinetic analysis of the coal samples was carried out by the Coats–Redfern method and the activation energies of the enriched coals were determined. The activation energies of the raw and the enriched coals were assessed and compared. The calculated activation energy values for the combustion reactions of the coal samples ranged were found to be between 15.17 kJ/mol and 97.45 kJ/mol. The strong correlation was obtained between the float and sink test results especially with the ash content of the coal samples and the combustible characteristic of the floated materials such as ignition temperatures, peak temperatures, and activation energies. The combustion characteristics of the coal samples were resultantly ascertained to be very dependent on the coal structure.

1. Introduction

Coal is a crucial source of the energy supply in many countries and for steel, cement, and concrete industries. The coal reserves including newly explored basins have reached to the sum of 15.4 billion tons at the end of the year 2014 in Turkey. The 14.1 billion tons of the coal reserves (about 92% of total) are lignite coals [1]. The lignite coals of Turkey were evaluated mostly in power generation because of their subdued calorific value and high ash content. Coal has a heterogeneous structure and complex mixture of organic and inorganic species in general. These specifications of coal limit its utilization from time to time and cause some serious problems in practice. It is important to increase the quality of coal by reducing its ash content, hence increasing its

calorific value. Therefore, cleaning of the coal is a process via comprising the removal of incombustible materials from coal. Many enrichment practices can be applied for the beneficiation of the coal such as jigging, dense media separation, froth flotation, oil agglomeration, shaking tables, washing cyclones, etc. Amongst these methods, the dense medium application mostly is used in the coal beneficiation plants in Turkey due to the larger upper limit of separation and the acceptable efficiency. Advanced cleaning possibilities of low-rank coals have been studied by many researchers [2, 3]. The further investigation of sink and float process was employed by many other researchers. Aktas et al. [4] used centrifugal float and sink separation technic in heavy medium and investigated the contribution of surface active agents for several Turkish coals. They had a conclusion of that the separation

TABLE 1: The specifications of coal sample *[31].

density (ton/m ³)	Ash (%)	Moisture (%)	Lower calorific value (kcal/kg)	C (%)	H (%)	N (%)	O (%)	S (%)
1.5*	35.84	12.85	2482*	30.2	3.01	1.0	15.3	1.8

efficiency much depended on the rank of coal. Tian et al. [5] applied low temperature oxygen-plasma ashing method before float and sink experiments for the determination of mineralogical characteristic and trace element affinities of coals collected from different regions of China. The light and heavy minerals isolated from the organic component of coal were separated according to their different densities by this method. Guanghui et al. [6] also developed a method which rapidly predicted the density compounds of run of mine coal. Their model processes the data obtained from floats and sinks along with standardized monthly production data as rapid as possible and more reliable prediction of gravity separation. Some other researchers additionally improved mathematical modelling for cleaning of coal [7–9]. Ozer [10] introduced a new cheap experimental setup for density fractionating of fine coal samples by putting the principles of separating funnel and funnel-flask methods together.

Dense medium separation not only utilizes sulphur and ash rejection but also increases the calorific value of coal. Therefore, the characterization of coal for combustion would be improved and thermal behaviour of coal would be changed.

The thermal behaviour of coal is determined mostly by using TG. Although, many works on biomass combustion with TG [11–15] and coal combustion [16–23] are available in the literature, investigations on ‘enriched coal’ are rather less [24–26]. The enrichment of coal provides an opportunity for the separation of coals and their maceral composition due to the difference of densities [27].

Indian researchers [12] investigated the possible usage of biomass products with pulverized coal due to the foresight of the increase in energy demand. They determined the TGA parameters such as activation energy and ignition index to assess the combustion features of coal blends with different biomass chars which would be helpful for identifying suitable biomass-type and blend proportion for a given coal in order to reveal some exclusive advantages in terms of particular combustion exercise. Podder and his coworkers [16] also investigated the thermal behaviours of Bangladeshi coals by TGA analysis. They observed the primary and secondary devolatilization sections when the coal was heated up to 600°C. In addition, the combustion specifications of biomass fuels and lignite coals were studied by Turkish researchers [17]. They concluded that low-rank coals with biomass could be efficiently burnt. In a different research, the low-rank Indian coals were agglomerated by using binders for the preparation of cooking [25] and the combustion characteristics were determined by TG and DTA analyses.

DTG was the first thermoanalytical implementation utilized in the investigation of the thermal behaviour of coal. DTG also provides to investigate of decomposition reactions in coal. A derivative weight loss curve can be put into practice

to point out the ignition and peak temperatures at which the weight loss is the most apparent [28, 29]. The reaction kinetics of coals is also determined from thermogravimetric analysis [30].

The primary purpose of the present work is to evaluate the washability characteristics of lignite coal via float and sink method and the influence of the enrichment on combustible behaviour of the coal. Therefore, the thermal and kinetic analyses were performed on the beneficiated coal samples. The strong relation was seen between the physical features of the products obtained from float and sink experiments and combustion results. The TG and DTG characteristics, ignition temperatures, peak temperatures, and activation energies were also analysed and the obtained results were explicated comparatively.

2. Experimental

2.1. Coal Sample Specifications. The run of mine (RoM) lignite coal from Orhaneli (Bursa) district of Turkey was used in the float and sink tests. The specifications of the coal sample were given in Table 1 [31]. It was determined that the raw coal sample has a high ash content value of 35.84%. The coal sample was screened as soon as received and sieved to five fractions as -32+25 mm, -25+16 mm, -16+8 mm, -8+4.75 mm, and -4.75+2 mm. The particle size distribution of raw coal was also determined and illustrated in Figure 1. Each fraction was washed and percolated before the float and sink experiments.

2.2. Experimental Procedures

2.2.1. Float and Sink Experiments. All fractions were processed separately in dense media with the densities of 1.20, 1.30, 1.40, 1.50, and 1.60 g/cm³. The dense mediums were prepared with -45 µm size of magnetite and tap water. Each fractioned coal sample was dipped into the dense medium starting with higher density to lower density step by step. The constituents with a density lower than the dipped medium's density floated and the floated particles were transferred in the lighter medium. The float products were washed and percolated before placed in the lower density liquid. This treatment was repeated until the lightest medium was reached. The sunken parts were separated from the liquid and washed away to remove the magnetite content from the coal. Thereafter, the products were dried, weighted, and then prepared for thermal analysis. In addition, the dense medium was stirred rather slowly to avoid magnetite sinking.

2.2.2. Thermogravimetric Analyses. Thermogravimetric analysis is often used in ascertaining the thermal attitude of solid fuels as shown in many previous works. Therefore, Polymer

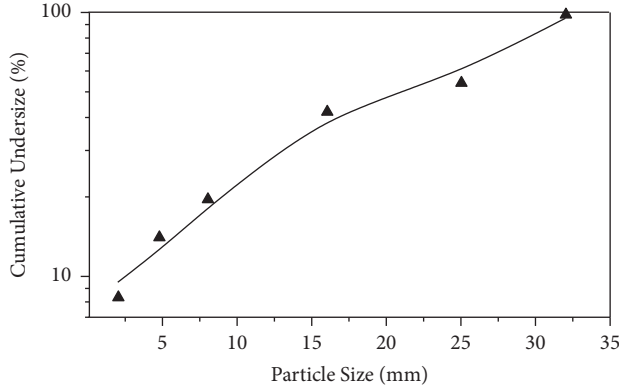


FIGURE 1: Particle size distribution of coal sample.

Laboratories PL-TGA 1500 thermal analyser was used for the thermogravimetric analysis of floated coal samples obtained from float and sink tests. Detailed schematic representation of the experimental procedure can be found in the literature [32].

After float and sink experiments, each obtained sample was reduced into the same particle size which was less than 100 μm by using laboratory type of ceramic ball mill. About ten milligrams of samples was heated up to 900°C at a constant rate of 10°C/min in a 5 mL/min flow of dry air. Then, the variation of sample mass in accordance with the heating rate was analysed in real time. Prior to thermogravimetric analysis of samples, the calibration of device has been carried out both for the mass and for the temperature. TG and DTG curves were derived from the analysis and the ignition and the peak temperatures of the samples were found using DTG curves according to the following:

$$\frac{T_{\text{final}} - T_{\text{initial}}}{t_{\text{final}} - t_{\text{initial}}} = \frac{dW}{dt} \quad (1)$$

where T is temperature (°C), t is time (min), and W (mg) is weight of sample. Analysis of each sample was repeated twice at least and repeatability was checked. The repeatability of the tests was found to be more than 99%. In addition, some of the experiments were performed twice at least to test the reproducibility of the results with standards errors of $\pm 1^\circ\text{C}$, to be reached. The peak and the ignition temperatures of the lignite coal sample can be obtained from burning profile and DTG curve. While the first peak indicates the ignition temperature, the second peak represents the peak temperature. Typical TG and DTG curves of lignite coal (RoM) were given in Figure 2. The weight loss of coal was raised with an increase in temperature. The ignition and peak temperatures were found to be 204°C and 398°C, respectively, from DTG curve. It is stated from the literature that the more reactive the coal is, the lower the maximum peak temperature is [29, 33–35].

2.2.3. Kinetic Analyses. The Coats and Redfern [36] approach based on the Arrhenius equation was used in the present work for the calculation of the kinetic parameters. This integral

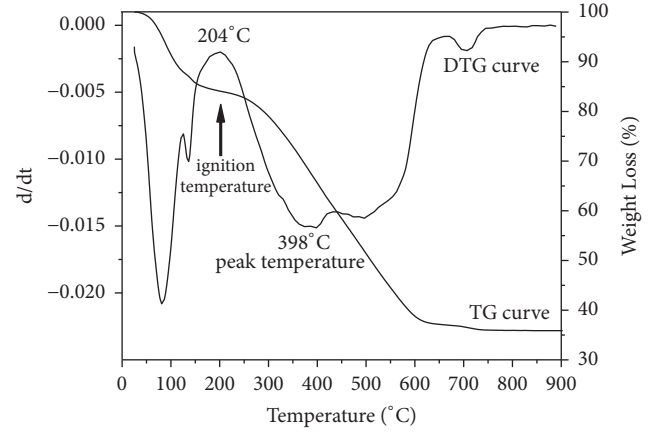


FIGURE 2: TG and DTG curves with ignition and peak temperatures of the coal sample.

method can be implemented to TG/DTG data, assuming the reactions order n as 1. The correct order is foreseen to lead to the best linear plot, from which the activation energy is appointed.

The final equation derived by this method is as follows:

$$\ln \left[-\frac{\ln(1-\alpha)}{T^2} \right] = \ln \left[\frac{A_r R}{\beta E} \left(1 - \frac{2RT}{E} \right) \right] - \frac{E}{RT} \quad (2)$$

In (2), T is temperature; A_r is Arrhenius constant; β is constant heating rate; E is activation energy; α is weight loss degrees which can be calculated by

$$\alpha = \frac{W_0 - W_t}{W_0 - W_f} \quad (3)$$

where W_0 is the initial weight of sample; W_f is the final weight of sample after burnt down.

According to the Coats and Redfern method, the expression $\ln[(A_r R / \beta E)(1 - 2RT/E)]$ in (2) is specifically constant under most circumstances. Plots of $\ln[-\ln(1-\alpha)/T^2]$ against $1/T$, a straight line should be obtained. The straight line with the maximum correlation coefficient will be taken as the function of the model that best expresses the kinetics of mass loss. Therefore, the activation energy, E , can be obtained from the slope of the line, $-E/R$.

3. Results and Discussion

3.1. The Results of the Float and Sink Experiments. The results of the float and sink experiments were given in Table 2 for all fractions.

In the Table 2, the highest yield of sinking part was achieved as 25.44% from the -32+25 mm fraction at specific gravity of 1.60 g/cm³ medium. The ash content of floating part in the -25+16 mm fraction at 1.20 g/cm³ specific density which had the minimum ash content as 4.51% was the 13.50% of the total sum of coal. This value was the lowest ash content obtained from the all float and sink tests. The ash content of floating parts at 1.20 and 1.30 g/cm³ of specific densities was

TABLE 2: The results of float and sink experiments.

Specific gravity range (g/cm ³)		-32+25 mm		-25+16 mm		-16+8 mm		-8+4.75 mm		-4.75+2 mm	
		Float	Ash	Float	Ash	Float	Ash	Float	Ash	Float	Ash
		Weight (%)	(%)	Weight (%)	(%)	Weight (%)	(%)	Weight (%)	(%)	Weight (%)	(%)
	-1.20	16.34	6.32	13.50	4.51	27.72	7.69	33.39	7.74	34.92	6.27
+1.20	-1.30	2.59	7.34	5.77	6.13	10.94	8.56	35.81	8.28	24.00	8.42
+1.30	-1.40	21.72	7.45	55.94	9.55	25.77	10.48	21.61	14.44	26.00	13.41
+1.40	-1.50	24.02	9.49	11.68	13.01	24.78	12.99	3.18	38.00	3.97	24.39
+1.50	-1.60	9.89	27.24	2.70	21.40	0.69	28.29	0.63	36.13	5.79	23.74
+1.60		25.44	83.03	10.41	78.43	10.10	76.31	5.38	79.53	5.32	76.35

very close for all fractions. In addition, the -4.75+2 mm size was the finest fraction in the experiments and the quantity of the floating part was quite a few at higher density mediums. The yield of floated material was 84.92% of total amount of sample under the specific gravity of 1.40 g/cm³ mediums at this fraction. Similar trend was followed for -8+4.75 mm size fraction. It was observed that when the density of the medium reached the coal density, the amount of the floated material was decreased significantly. The separation sensitivity was also lowered at 1.40 and 1.50 g/cm³ of specific densities of medium due to the approaching densities of both the coal samples and the medium. In addition, this decrease in the separation efficiency occurring because of the size may be due to the slower rate of settling of particles [37].

Whereas the ash content of sink materials of -32+25 mm fraction was 83.03%, it was decreased to 76.35% for -4.75+2 mm fraction at the specific density of 1.60 g/cm³. This discrepancy was arising from the size differences of fractions. The separation efficiency of the inorganic compounds from the coal was enhanced with a decrease in the size of fractions according to the liberalisation. However, the effectiveness of specific gravity of medium on the particles would also decrease with the decrement of the particle size. In addition, it was concluded that when the specific gravity of dense medium reached the coal density (1.50 g/cm³), the amount of floated material was decreased significantly.

The ash content of floated materials from all fractions at different dense mediums was illustrated in Figure 3. The average ash content of all fractions at the specific gravity of 1.60 g/cm³ was about 80%.

3.2. Thermal Behaviour of the Enriched Coal. Coal is also identified as consisting primarily of hydroaromatic and aromatic clusters linked by aliphatic bridges [38, 39]. When coal is heated, small amounts of pyrolysis water move away from the structures at around 300-350°C [40]. At 350°C, primary carbonization starts initially with the release of carbon dioxide and hydrogen. Methane and other lower aliphatic are evolved together with hydrogen, carbon monoxide, and alkyl aromatics with warming up at last [41]. The physical, chemical, and thermal changes of heating coal are directly related to the coal components. Therefore, burning profiles of enriched coals were investigated using TG analysis depending on the available circumstances in the laboratory. The derivatives of

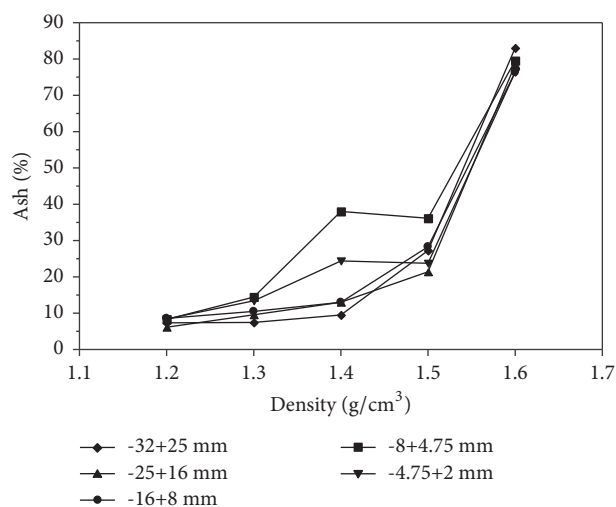


FIGURE 3: The ash contents of floated materials for all fractions at different specific gravities of medium.

TG curves were also estimated from the thermal profile of coal samples. The TG behaviour of floated materials from the float and sink experiments at different specific gravity of mediums for various size fractions was given in Figure 4. The sample code indicates the specific gravity of mediums. For example, the curve of 1.2 implies the floated materials obtained from the specific gravity of 1.2 g/cm³ medium. TG curves show the weight loss of the coal depending on the time relevant to heating. When evaluating all samples on their own merits, it might be seen that the whole burning profiles behaved in similar trend. This is related to similar chemical structures. The weight losses of the samples from 1.6 g/cm³ density for all fractions were lower than the others due to the higher quantity of inorganic materials. According to TG results, three regions were observed on thermographs. The first region was the weight loss due to the elimination of moisture, the second and the third were due to the devolatilization. The main weight loss occurring in second region was due to oxidation and removal of the volatile matters and combustion of carbonaceous parts of the coal samples. After the volatiles were removed from the samples, the third region was seen in connection with the oxidation of the char remaining [11]. In addition, the samples having

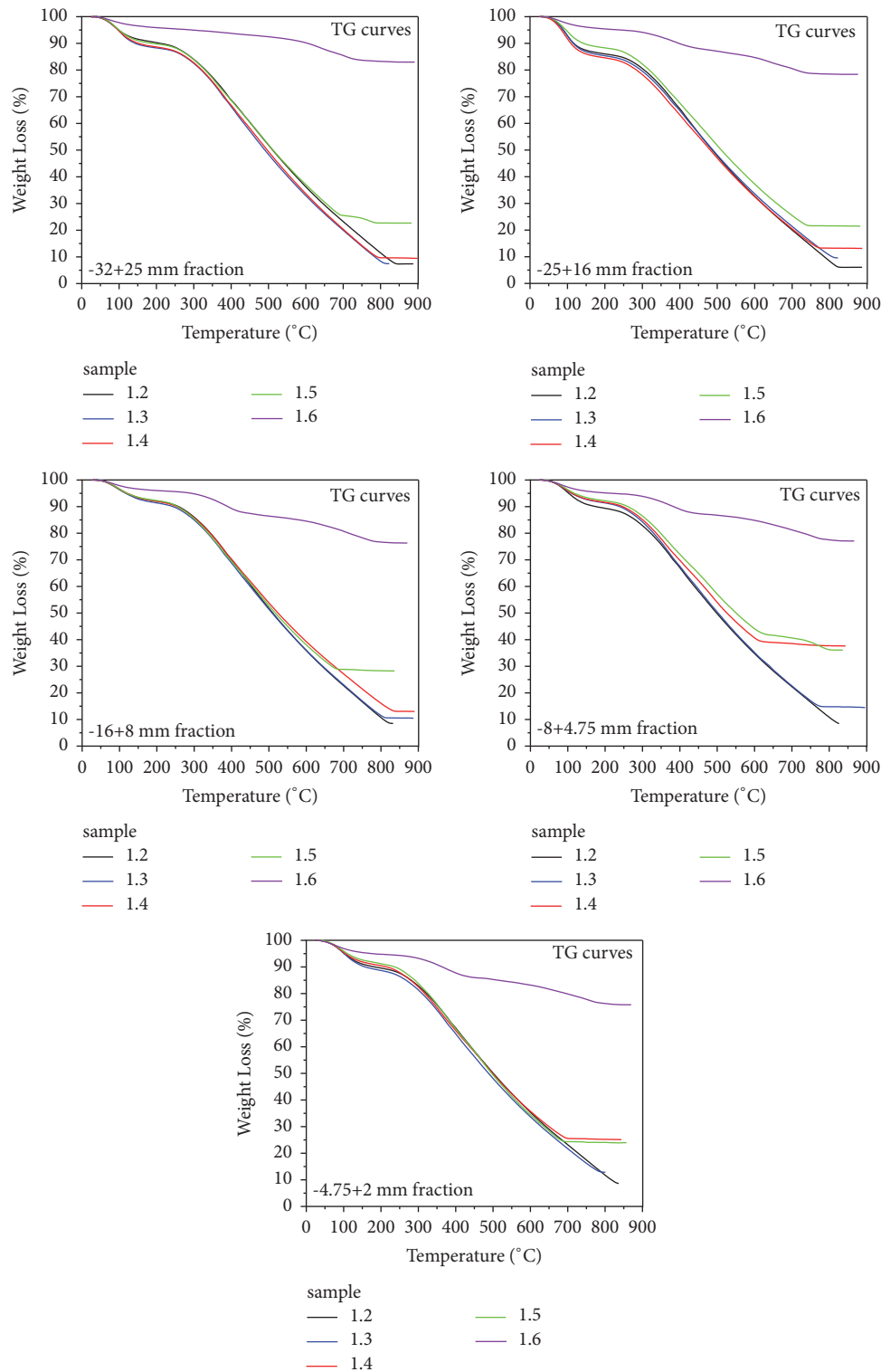


FIGURE 4: TG curves of floated materials for all fractions at different specific gravities of medium.

less inorganic materials in their structure started to ignition earlier as expected. The weight losses indicating these regions of TG curves could be easily seen from Figure 4.

The DTG profiles of floated materials at different specific gravity mediums were shown in Figure 5. DTG results

showed that the chemical reactivity of the coal samples was initially around 100°C, due to the loss of water (first region) as all the samples were dried after the float and sink tests. Two devolatilization reaction regions were observed in Figure 5 (region second and third). The second region

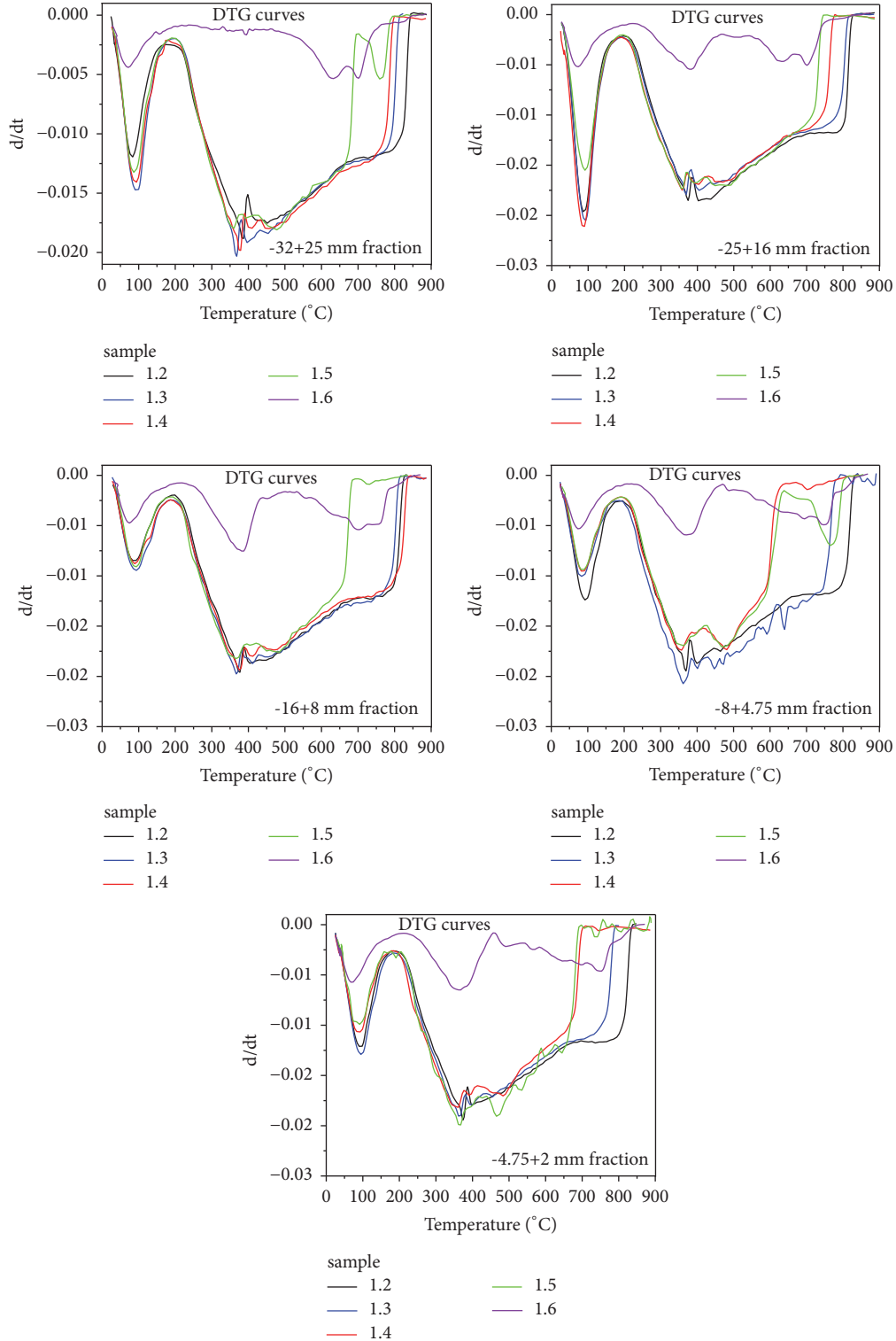


FIGURE 5: DTG curves of floated materials for all fractions at different specific gravities of medium.

approximately was started at 150°C and ended at 650°C. The third region was also started at about 650°C and ended at 850°C. The mass losses of coal samples were determined for enriched coals at different specific gravity of mediums and given in Table 3. The highest mass loss

was determined in the second reaction region for all coal samples due to the combustion of carbonaceous part of sample. When the carbonaceous content was increased due to the enrichment of coal, the observed mass loss was also raised.

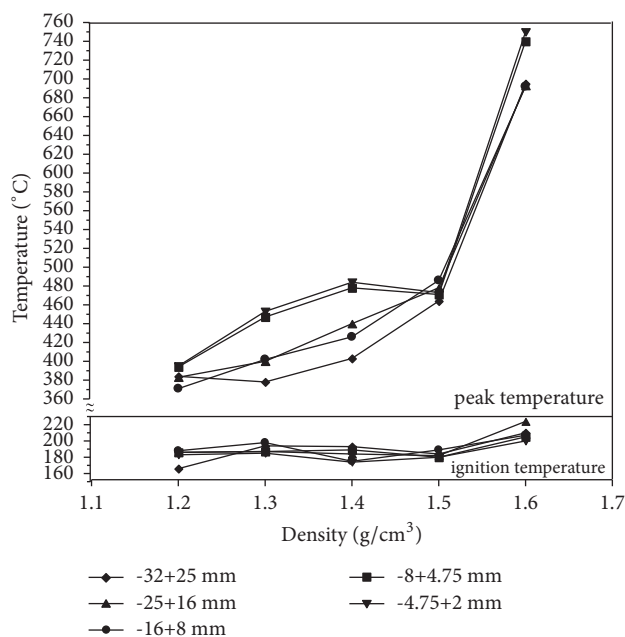


FIGURE 6: The ignition and peak temperatures of floated materials for all fractions at different specific gravities of medium.

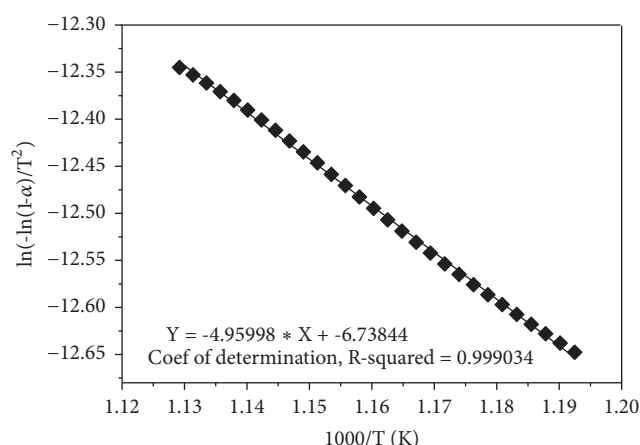


FIGURE 7: Plots of $\ln(-\ln(1-\alpha)/T^2)$ versus $1000/T$ of the coal sample.

The ignition and peak temperatures are important temperatures for burning behaviour of coal. The ignition temperature represents the place where the combustion is started. The peak temperature is also known as the temperature at which the rate of weight loss is at maximum degree through the maximum combustion rate. The ignition and the peak temperatures were also obtained from thermographs of DTG and given in Figure 6. The peak temperature is the indicative of the combustibility of coal. The coal with a difficult combustible behaviour has the higher peak temperature. As seen from Figure 6, when the specific gravity of the medium was increased, the acquired peak temperatures were also increased and the maximum peak temperature was obtained at 1.6 g/cm^3 density of medium for all fractions. The ignition temperatures of coal also showed similar trend. Generally,

TABLE 3: The range of mass losses of coal samples at three reaction regions.

Sample	Mass loss (%)		
	I	II	III
1.2	8-13	85-89	2-3
1.3	8-14	77-84	1-2
1.4	7-14	52-81	1-3
1.5	7-10	49-72	2-5
1.6	4-6	11-20	2-4

coking coals pass through a plastic or softening state in the temperature range $350\text{--}450^\circ\text{C}$ depending on their rank [42, 43] in the second region. In Figure 6, the obtained peak temperatures that ranged from 370°C to 480°C excepting the peak temperatures of coal which obtained 1.6 g/cm^3 density were in harmony with the literature. In the third region, the decomposition of the mineral matter occurred in the samples due to the decomposition temperatures of minerals in coal such as calcite, kaolinite in the range of $650\text{--}850^\circ\text{C}$ [44]. Further bond breaking occurs and evolution of organic matter as tar, gases, and condensation reaction also takes place at this region. In addition, it was shown as in Figure 6 that a reduction was observed in ignition temperatures as the particle size decreased [15].

If Figures 3 and 6 were compared with each other, the strong correlation could be seen between the curves. The peak temperatures were already related to the combustibility of coal and consequently ash content. As a result, the higher ash content caused the superior peak temperature while lower temperature indicated more easily burnt samples.

3.3. Kinetic Analysis Results of the Coal Combustion. The activation energy of raw lignite sample was calculated as 41.24 kJ/mol from the plots of $\ln(-\ln(1-\alpha)/T^2)$ versus $1000/T$ and given in Figure 7.

The activation energies of floated material from the float and sink tests at 1.20 , 1.30 , 1.40 , 1.50 , and 1.60 g/cm^3 of densities mediums for $-32+25 \text{ mm}$, $-25+16 \text{ mm}$, $-16+8 \text{ mm}$, $-8+4.75 \text{ mm}$, and $-4.75+2 \text{ mm}$ sizes were also determined and the obtained results were given in Figure 8. The correlation coefficients of all samples were above 0.995 . These top level correlation coefficients indicate that corresponding independent first-order reaction model fits with experimental data very well. It is clear from Figure 8 that the activation energies of all fractioned samples which floated at 1.60 g/cm^3 density were the maximum. The quantity of inorganic mineral matter causing the ash content of coal structure was also measured about 80% at this density medium. The activation energies of coal are much related to the ash content itself [41]. When considering the specified ash content of samples at Figure 3, the combustible behaviour of samples such as peak temperatures from Figure 6 and the activation energies from Figure 8 showed similar tendency. The activation energy and ash content of raw coal were determined as 41.24 kJ/mol and 35.84% , respectively. When the ash content of coal was decreased to 7.34% , the activation energy was 16.205 kJ/mol

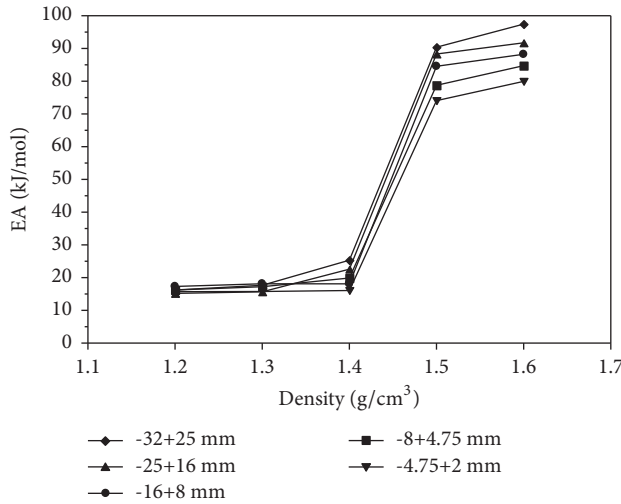


FIGURE 8: Activation energies of floated coal samples at different densities after the float and sink experiments.

which was the lowest value obtained (sample was 1.2 at +32-25 mm fraction). In a similar manner, when the ash content of coal sample was increased to the highest value of 83.03%, the determined activation energy was 97.45 kJ/mol (sample was 1.6 at -32+25 mm fraction). Ozbas et al. [26] reached parallel results in their work. They investigated the kinetic analysis of three different coals and effect of enrichment on the kinetic parameters of coals. The obtained activation energies of cleaned samples were lower than the raw coal. Hicyilmaz et al. [24] reached comparable combustion behaviour for Tuncbilek coal in Turkey. They concluded that the activation energies of utilized coal decreased and reactivity of coal increased. Reaction with high activation energy needed a high temperature or a long reaction time as indicated in the literature [45]. The higher activation energies also imply that the reactions were more temperature-dependent [15]. Kok [23] obtained the activation energies of two different coals by TG-DTG methods in the range of 27.6-42.2 kJ/mol.

4. Conclusions

The purpose of this study is to relate the combustion reactivity of lignite with its physical properties. For the enrichment of the coal samples, the float and sink tests were performed and then the combustion behaviour of these coal samples was investigated. The thermal analysis methods and the kinetic analysis of thermogravimetric (TG) data were carried out by using the Coats Redfern kinetic model at nonisothermal conditions. The following conclusions were derived:

- (1) The ash content of the coal obtained from the float and sink method had variations. The floated coal having minimum ash content (4.51%) was attained from -25+16 mm fraction at 1.20 g/cm³ specific density medium. When the specific gravity of dense medium was arranged around the coal density (1.50 g/cm³), the amount of floated material was decreased significantly.

- (2) The observed weight losses of the samples from 1.6 g/cm³ density for all fractions were lower than the others due to the higher quantity of inorganic materials as seen from the TG results. The main mass loss was due to the release of carbon dioxide and hydrogen in primary carbonization stage.
- (3) The three regions were watched on thermographs. The first region was where the moisture left the coal and the second and third regions illustrated the devolatilization regions.
- (4) Strong correlation was determined between the ash content and thermal behaviour of coal.
- (5) The higher ash content of the sample caused the superior peak temperature and the lower temperature demonstrates the more easily burnt samples.
- (6) The activation energies of coal are much related to the ash content itself according to the experimental results. The determined activation energies varied between 15.17 kJ/mol and 97.45 kJ/mol. The enrichment of coal decreased the activation energy and increased the coal reactivity.

Nomenclature

- E : Activation energy (kJ/mol)
 R : Gas constant (J/mol, K)
 T : Absolute temperature (K or °C)
 α : Weight loss degrees
 t : Time (min)
 W_t : Weight of coal at t time (g)
 W_0 : Initial weight of coal (g)
 W_f : Final weight of coal burnt down (g)
 β : Rate of heating (K/min)
 A_r : Arrhenius constant, (1/min).

Data Availability

The data used to support the findings of this study are available from the corresponding author upon request.

Conflicts of Interest

The authors declare that there are no conflicts of interest regarding the publication of this paper.

Acknowledgments

The authors greatly acknowledge the financial support provided by Scientific Research Project Fund of Selcuk and Dumlupinar Universities.

References

- [1] GDMRE, *General Directorate of Mineral Research and Exploration of Turkey. Annual Report*, 2015.

- [2] Q. Zhang, Y. Tian, Y. Qiu, J. Cao, and T. Xiao, "Study on the washability of the Kaitai coal," *Fuel Processing Technology*, vol. 92, 2011.
- [3] Y. Cebeci, U. Ulusoy, and I. Sonmez, "Determination of optimum washing conditions for a lignite coal based on ash and sulfur content," *Fuel*, vol. 123, 2014.
- [4] Z. Aktas, F. Karacan, and A. Olcay, "Centrifugal float-sink separation of fine Turkish coals in dense media," *Fuel Processing Technology*, vol. 55, article 235, 1998.
- [5] C. Tian, J. Zhang, Y. Zhao, and R. Gupta, "Understanding of mineralogy and residence of trace elements in coals via a novel method combining low temperature ashing and float-sink technique," *International Journal of Coal Geology*, vol. 131, article 162, 2014.
- [6] G. Wang, Y. Kuang, Z. Wang, L. Ji, and Y. Wang, "Rapid prediction of floating and sinking components of raw coal," *International Journal of Mining Science and Technology*, vol. 22, no. 5, pp. 735–738, 2012.
- [7] J. Abbott and N. J. Miles, "Smoothing and interpolation of float/sink data for coals," *Minerals Engineering*, vol. 4, no. 3/4, 1991.
- [8] B. Govindarajan and T. C. Rao, "Calendar of international conferences, symposia, courses and meetings of interest," *Minerals Engineering*, vol. 7, no. 11, article 1441, 1994.
- [9] Y. Cebeci and N. Aslan, "Using float-sink data in simple equations to predict sulfur contents," *Fuel Processing Technology*, vol. 76, no. 3, pp. 231–239, 2002.
- [10] C. E. Ozer, "A new simple method for density fractionation of finely sized coal," *Minerals Engineering*, vol. 86, article 114, 2016.
- [11] S. Y. Yorulmaz and A. T. Atimtay, "Investigation of combustion kinetics of treated and untreated waste wood samples with thermogravimetric analysis," *Fuel Processing Technology*, vol. 90, no. 7–8, pp. 939–946, 2009.
- [12] S. G. Sahu, P. Sarkar, N. Chakraborty, and A. K. Adak, "Thermogravimetric assessment of combustion characteristics of blends of a coal with different biomass chars," *Fuel Processing Technology*, vol. 91, article 369, 2010.
- [13] X. Liu, M. Chen, and Y. Wei, "Combustion behavior of corn-cob/bituminous coal and hardwood/bituminous coal," *Renewable Energy*, vol. 81, 2015.
- [14] S. Bada, R. Falcon, and L. Falcon, "Characterization and co-firing potential of a high ash coal with Bambusa balcooa," *Fuel*, vol. 151, pp. 130–138, 2015.
- [15] K. Jayaraman, M. V. Kok, and I. Gokalp, "Thermogravimetric and mass spectrometric (TG-MS) analysis and kinetics of coal-biomass blends," *Renewable Energy*, vol. 101, article 293, 2017.
- [16] J. Podder, T. Hossain, and K. M. Mannan, "An investigation into the thermal behaviour of Bangladeshi coals," *Thermochimica Acta*, vol. 255, no. C, pp. 221–226, 1995.
- [17] M. Varol, A. T. Atimtay, B. Bay, and H. Olgun, "Investigation of co-combustion characteristics of low quality lignite coals and biomass with thermogravimetric analysis," *Thermochimica Acta*, vol. 510, no. 1–2, pp. 195–201, 2010.
- [18] H. Haykiri-Açma, A. Ersoy-Meriçboyu, and S. Küçükbayrak, "Combustion reactivity of different rank coals," *Energy Conversion and Management*, vol. 43, no. 4, pp. 459–465, 2002.
- [19] M. V. Kok, "Recent developments in the application of thermal analysis techniques in fossil fuels," *Journal of Thermal Analysis and Calorimetry*, vol. 64, article 1319, 2001.
- [20] O. Oren and C. Sensogut, "Determination of Safe Storage Types for Coals with Regard to Their Susceptibility to Spontaneous Combustion – Tuncbilek Coal Case," *International Journal of Coal Preparation and Utilization*, 2016.
- [21] L. Ge, Y. Zhang, C. Xu, Z. Wang, J. Zhou, and K. Cen, "Influence of the hydrothermal dewatering on the combustion characteristics of Chinese low-rank coals," *Applied Thermal Engineering*, vol. 90, article 174, 2015.
- [22] X. Wang, E. Cotter, K. N. Iyer, J. Fang, B. J. Williams, and P. Biswas, "Relationship between pyrolysis products and organic aerosols formed during coal combustion," *Proceedings of the Combustion Institute*, vol. 35, article 2347, 2015.
- [23] M. V. Kok, "Simultaneous thermogravimetry-calorimetry study on the combustion of coal samples: effect of heating rate," *Energy Conversion and Management*, vol. 53, article 40, 2012.
- [24] C. Hiciyilmaz, K. E. Ozbaz, and M. V. Kok, "The benefit of coal washing from the view of combustion kinetics," in *Proceedings of the 13th Turkish Coal Congress, Zonguldak/Turkey*, 2002.
- [25] T. Das, B. K. Saikia, D. K. Dutta, D. Bordoloi, and B. P. Baruah, "Agglomeration of low rank Indian coal fines with an organic binder and the thermal behavior of the agglomerate produced: Part I," *Fuel*, vol. 147, article 269, 2015.
- [26] K. Ozbaz, M. V. Kok, and C. Hiciyilmaz, "Comparative kinetic analysis of raw and cleaned coals," *Journal of Thermal Analysis and Calorimetry*, vol. 69, article 541, 2002.
- [27] D. C. Cronauer, J. T. Joseph, A. Davis, J. C. Quick, and P. T. Luckie, "The beneficiation of Martin Lake Texas lignite," *Fuel*, vol. 71, no. 1, pp. 65–73, 1992.
- [28] J. W. Cumming and J. McLaughlin, "The Thermogravimetric Behaviour of Coal," *Thermochimica Acta*, vol. 57, article 253, 1982.
- [29] C. Sensogut, H. Ozsen, and A. Demirbas, "Combustion characteristics of 24 lignite samples," *Energy Sources, Part A: Recovery, Utilization, and Environmental Effects*, vol. 30, no. 5, pp. 420–428, 2008.
- [30] T. J. Kang, H. Namkung, D. H. Jang, and H. T. Kim, "Experimental study on different heating rate kinetics of Indonesian and Inner Mongolian low rank coal for catalytic gasification," *Journal of Industrial and Engineering Chemistry*, vol. 20, article 2095, 2014.
- [31] GDMRE, General Directorate of Mineral Research and Exploration of Turkey. The lignite inventory of Turkey, 2010.
- [32] S. Duzyol and C. Sensogut, "The relation between hydrophobic flocculation and combustion characteristics of coal," *Fuel Processing Technology*, vol. 137, pp. 333–338, 2015.
- [33] J. W. Cumming, "Reactivity assessment of coals via a weighted mean activation energy," *Fuel*, vol. 63, article 1436, 1984.
- [34] W. A. Kneller, "Physicochemical characterization of coal and coal reactivity: a review," *Thermochimica Acta*, vol. 108, article 357, 1986.
- [35] N. B. Sarkar, P. Sarkar, and A. Choudhury, "Effect of hydrothermal treatment of coal on the oxidation susceptibility and electrical resistivity of HTT coke," *Fuel Processing Technology*, vol. 86, no. 5, article 86, 2005.
- [36] A. W. Coats and J. P. Redfern, "Kinetic parameters from thermogravimetric data," *Nature*, vol. 201, no. 4914, pp. 68–69, 1964.
- [37] B. Wills, "An Introduction to the Practical Aspects of Ore Treatment and Mineral Recovery," in *Mineral Processing Technology*, Pergamon Press, Oxford, UK, 8th edition, 2015.
- [38] J. B. Howard, "Fundamentals of coal pyrolysis and hydrolysis," in *Chemistry of coal utilization*, M. A. Elliott, Ed., Wiley-Interscience, Toronto, Canada, 1981.

- [39] P. R. Solomon, M. A. Serio, and E. M. Suuberg, "Coal pyrolysis: Experiments, kinetic rates and mechanisms," *Progress in Energy and Combustion Science*, vol. 18, no. 2, pp. 133–220, 1992.
- [40] P. R. Solomon, M. A. Serio, R. M. Carangelo et al., "Analysis of the Argonne Premium Coal Samples by Thermogravimetric Fourier Transform Infrared Spectroscopy," *ENERGY & FUELS*, vol. 4, no. 3, pp. 319–333, 1990.
- [41] K. E. Ozbas, S. Bilgen, C. Hicyilmaz, and M. V. Kok, "Thermogravimetric behaviour of some Turkish lignites of different sizes," *Fizykochemiczne Problemy Mineralurgii*, vol. 32, article 149, 1998.
- [42] H. D. Glass, "Differential thermal analysis of coking coals," *Fuel*, vol. 34, article 253, 1955.
- [43] C. Moon, Y. Sung, S. Ahn, T. Kim, G. Choi, and D. Kim, "Thermochemical and combustion behaviors of coals of different ranks and their blends for pulverized-coal combustion," *Applied Thermal Engineering*, vol. 54, no. 1, pp. 111–119, 2013.
- [44] J. V. O'Gorman and P. L. Walker, "Thermal behaviour of mineral fractions separated from selected American coals," *Fuel*, vol. 52, article 71, 1973.
- [45] M. J. Lazaro, R. Moliner, and I. Suelves, "Non-isothermal versus isothermal technique to evaluate kinetic parameters of coal pyrolysis," *Journal of Analytical and Applied Pyrolysis*, vol. 47, pp. 111–125, 1998.